5-2023

Blood Flow Regulates Atherosclerosis Progression and Regression

Morgan A. Schake
University of Nebraska–Lincoln, mschake@huskers.unl.edu

BLOOD FLOW REGULATES ATHEROSCLEROSIS PROGRESSION AND REGRESSION

by

Morgan A. Schake

A DISSERTATION

Presented to the Faculty of

The Graduate College at the University of Nebraska

In Partial Fulfillment of Requirements

For the Degree of Doctor of Philosophy

Major: Biomedical Engineering

Under the Supervision of Professor Ryan M. Pedrigi

Lincoln, Nebraska

May, 2023

BLOOD FLOW REGULATES ATHEROSCLEROSIS PROGRESSION AND REGRESSION

Morgan A. Schake, Ph.D.

University of Nebraska – Lincoln, 2023

Advisor: Ryan M. Pedrigi

Atherosclerosis is the most prevalent pathology of cardiovascular disease with no known cure. Despite the many systemic risk factors for atherosclerosis, plaques do not form randomly in the vasculature. Instead, they form around bifurcations and the inner curvature of highly curving arterial segments that contain so-called disturbed blood flow that is low in magnitude and multidirectional over the cardiac cycle. Conversely, straight, non-bifurcated arterial segments that contain moderate-to-high and unidirectional (i.e., normal) blood flow are protected from plaque development. Thus, blood flow is a key regulator of atherosclerosis that may be able to be leveraged to develop new therapeutics. Towards this end, we performed two studies using a mouse model of atherosclerosis where a blood flow-modifying cuff was placed around the left carotid artery to induce disturbed blood flow and, in turn, plaque development. In the first study, we evaluated the hypothesis that injected nanoparticles had different accumulation kinetics in different types of disturbed flow (low versus multidirectional). We found that the blood flow profile did not affect accumulation, but the resultant plaque phenotype did. This suggests that nanoparticles could be used to target certain plaque types. In the second study, we evaluated the hypothesis that restored normal blood flow in atherosclerotic arteries promotes plaque stabilization. Our findings supported this hypothesis and also showed

that the combination of normal blood flow and atorvastatin produced additive beneficial effects that led to plaque regression. This result suggests that mechanical stimuli can be therapeutic. Since the endothelium directly senses blood flow and plays a key role in atherosclerosis development, we finally characterized how different flow profiles affect atheroprotective versus atherogenic endothelial signaling molecules. Ultimately, this work provides a foundation for the development of a new therapeutic for atherosclerosis based on the beneficial effects of normal blood flow.

ACKNOWLEDGMENTS

Chapter 2 and 3's work was supported by grants from the National Institute of Biomedical Imaging and Bioengineering of the National Institutes of Health (NIH) to RMP (R21EB028960), the American Heart Association to RMP (19CDA34660218), the National Science Foundation to RMP (CMMI-1944131), and the National Heart, Lung, and Blood Institute of the NIH to YC (R01HL144690). I also acknowledge support from the Nebraska Center for Integrated Biomolecular Communication to RMP (NIH, National Institute of General Medical Sciences (NIGMS) grant P20GM113126) and the UNMC Small Animal Ultrasound Core (RRID:SCR_022683), which is supported in part by funding from the Nebraska Center for Nanomedicine (NIGMS grant P30GM127200). The CFD simulations for Chapter 3 were completed using the Holland Computing Center of the University of Nebraska, which receives support from the Nebraska Research Initiative. Cryosectioning for Chapter 2 & 3 was performed with equipment provided by the Nebraska Center for Biotechnology Microscopy Core.

I'd also like to thank veterinarians Dr. Craig Kreikemeier-Bower and Dr. Anna Fitzwater for their assistance in caring for the mice and performing instrumentation of the left carotid arteries.

Additionally, I'd like to thank my advisor, Dr. Pedrigi, for his never-ending support and help throughout my Ph.D. I'd also like to thank my laboratory mates, Ian McCue and Jaideep Sahni. We learned a lot from each other.

PREFACE

Chapter 2 was published in *PLoS One*. Morgan A. Schake, Hunter A. Miller, Badrul Alam Bony, Evan T. Curtis, Connor C. Gee, Ian S. McCue, Thomas J. Ripperda Jr., Yiannis S. Chatzizisis, Forrest M. Kievit, Ryan M. Pedrigi. *Smooth muscle cells affect differential nanoparticle accumulation in disturbed blood flow-induced murine atherosclerosis.* PLoS One, 2021. **16**(12): p. e0260606.

Chapter 3 was published in *iScience.* Morgan A. Schake, Ian S. McCue, Evan T. Curtis, Thomas J. Ripperda, Samuel Harvey, Bryan T. Hackfort, Anna Fitzwater, Yiannis S. Chatzizisis, Forrest M. Kievit, Ryan M. Pedrigi., *Restoration of normal blood flow in atherosclerotic arteries promotes plaque stabilization.* ISCIENCE (2023), doi: https://doi.org/10.1016/j.isci.2023.106760.

TABLE OF CONTENTS

TABLE OF FIGURES

TABLE OF EQUATIONS

NOMENCLATURE

- LDL – low density lipoprotein. “bad cholesterol”
- HDL – high density lipoprotein. “good cholesterol”
- WSS – Wall shear stress
    - TAWSS – time average wall shear stress
    - MagMeanWSS – magnitude mean wall shear stress
    - OSI – oscillatory shear index
    - TransWSS – transverse wall shear stress
    - RRT – relative residence time
- Atherogenic – tending to promote the formation of fatty plaques in the arteries
- Atheroprotective – that protects against the formation of atherosclerosis
- Cells
    - ECs – Endothelial cells
    - HUVECS – Human umbilical vein endothelial cells
    - HAECS – Human aortic endothelial cells
- Transgenic Mice
    - $ApoE^{-/-}$ - Apolipoprotein E-deficient transgenic mice
    - $LDLr^{-/-}$ - LDL receptor-deficient transgenic mice
- Markers
    - NF-KB – Nuclear factor kappa B is a transcription factor that is activated by various cellular stimuli that induces multiple pro-inflammatory genes
    - KLF-2 – Kruppel-like factor 2 regulates endothelial inflammation by inhibiting adhesion molecules
    - eNOS – endothelial nitric oxide synthase helps to maintain endothelial cell homeostasis
    - THBD – thrombomodulin plays an important role as an anticoagulant
    - VE-Cadherin – vascular endothelial cadherin is an adhesion molecule located at the junctions between endothelial cells therefore a good marker for examining permeability

  - ET-1 – endothelin 1 is a potent vasoconstrictor peptide produces by vascular endothelial cells
  - CTFG – connective tissue growth factor is an important mediator and marker of tissue modeling and fibrosis
  - CAV-1 – caveolin 1 inhibits LDL transcytosis and vascular inflammation
  - CD31 – Platelet endothelial l adhesion molecules also known as cluster of differentiation 31 (CD31) is a protein that regulates leukocyte detachment, t-cell activation, platelet activation, and angiogenesis.
  - FSP-1 – fibroblast-specific protein 1 increases permeability in endothelial cells.
  - VEGF – vascular endothelial growth factor is a key regulator of angiogenesis, lipid metabolism and inflammation for developing atherosclerosis.
  - bFGF – basic fibroblast growth factor is major driver in plaque instability. It regulates angiogenesis, macrophage infiltration, and smooth muscle cell fate.
- In vivo – of a process performed or taking place in a living organism
- In vitro – of a process performed or taking place in a test tube, culture dish, or elsewhere outside of a living organism
- Ex vivo – experimentation or measurements done on tissue from an organism in an external environment or outside of the living body
- En face – the vertical layout or cross-section

CHAPTER 1

An Introduction to Atherosclerosis

Atherosclerosis refers to the process of plaque formation in the artery walls that results in acute complications such as myocardial infarction, unstable angina, and ischemic stroke [3]. Atherosclerotic lesions are characterized by the accumulation and transformation of lipids, inflammatory cells, smooth muscle cells, and necrotic cell debris in the intimal space underneath a monolayer of endothelial cells. In more complicated plaques, lesion growth can reduce blood flow by greater than 50%, thereby causing angina. It has been reported that 75% of acute myocardial infarctions occur from plaque rupture. This pathological process behind plaque rupture on fibroatheromas that causes heart attack or stroke, accounts for 850,000 global deaths annually [4]. From 2015 to 2018, the prevalence of cardiovascular disease in adults over the age of 20 years old was 49.2% with 126.9 million diagnoses in 2018 alone, costing $378 billion in medical expenses annually [4]. Typically, the atherosclerotic process begins in the first decade of life and progresses slowly, and based on the presence of several risk factors that are predominantly found in cardiovascular disease patients. In the United States alone, approximately 610,000 people die of heart disease every year. That is 1 in every 4 deaths. On average, about 735,000 Americans have a heart attack every year. Out of these patients, 525,000 suffer an initial attack, and 210,000 suffer from a recurrent attack [5].

1.1 Risk Factors

There are many risk factors such as hypercholesterolemia, hypertension, obesity, type I diabetes, and gender, that contribute to the progression of atherosclerosis. A healthy lifestyle is the cornerstone of cardiovascular health. In the most recent guidelines,

an estimated 28-37% of United States adults have moderate risk hypocholesterolemia and hypertension [6]. Hypocholesterolemia is responsible for 49% of the population's risk for a cardiac event. Incidences of atherosclerosis increase with higher levels of low-density lipoprotein (LDL). In western countries, specifically with high consumption of saturated fat and sugar that can lead to dyslipidemia, studies have shown that the mortality rate associated with cardiovascular-related diseases are higher than countries without consumption of these foods and associated lower cholesterol levels. Hypertension, or elevated blood pressure, is another major risk for cardiovascular disease and stroke. In a recent study to elucidate the mechanism by which hypertension accelerates cardiovascular disease, Al-Mashhadi *et al*. found that increased pressure facilitates coronary atherosclerosis by increasing smooth muscle cell activity and intimal accumulation of LDL [7].

Unhealthy diets and lifestyle also contribute to hypocholesterolemia and hypertension. About 50% of young adults and 31% of older adults have reported poor diets in surveys [5]. Exercise and physical activity also play a major role in atherosclerotic risks. Physical activity has been associated with reduced risk of cardiovascular disease due to improved glucose tolerance, reduced lipids, increased anti-inflammatory pathways, and reduced obesity [8]. Exercise appears to dampen hematopoiesis and reduces monocytes and neutrophils in both humans and mice. For example, in a transgenic mouse study examining exercise in leptin reduced animals (causing increased leukocyte expression), running induced lasting epigenetic changes, such as improved immune function, glucose tolerance, and mediating hematopoiesis, that persisted after the exercise was stopped [8]. Thus, the running mice demonstrated

improved anti-inflammatory effects with increased physical activity, despite the changes in leukocytes. Additionally, in a clinical study in 2018, physical activity of 3-4 forty-minute exercise sessions decreased blood pressure by an average of 4 mmHg and decreased cholesterol by an average of 4 mg/dL in humans [6]. Thus, high blood pressure and dyslipidemia are major risk factors, however, cardiovascular incidences due to these systemic risks can be decreased in physically active individuals by 21%, with a 36% decrease in chance of mortality [6].

Lastly, gender and estrogen levels also contribute to differences in LDL, HDL, triglycerides. There are major sex differences in lipid and lipoprotein metabolism that contribute to atherosclerotic disease progression. Starting at puberty, young men tend to have more atherogenic cholesterol profiles, while younger women are relatively protected from cardiovascular disease [9]. However, by age 55, women's incidence of myocardial infarction surpasses that of men. This is mainly due to sex hormone changes, especially estrogen [10]. In a hospital study evaluating lipoprotein lipid levels (total cholesterol, LDL, HDL, non-HDL, and triglycerides) in approximately 70,000 individuals (49,000 men and 20,000 women), it was demonstrated that levels of total LDL and non-HDL cholesterol levels, as well as triglycerides, peak earlier in men compared to women. Levels of cholesterol in men are highest at age 30-39, whereas this range is 50-59 in women. However, dyslipidemia trends are relatively similar between men and women [10]. The British Heart Foundation states that the number of women living with atherosclerosis is now roughly the same as the number of men. However, this phenomenon of men having earlier signs of atherosclerosis is difficult to study, especially since animal models don't show clear differences between sexes [11]. Therefore, much

remains to be learned about the hypercholesterolemia mechanisms for these sex-differences.

1.2 Vascular Anatomy

The artery is a tubular vessel for oxygen rich blood to flow through to reach perfusion sites. The vessel wall consists of three layers. The intima layer is composed of a monolayer of endothelial cells that are at the interface with the lumen and sense the mechanical environment, both shear stress due to blood flow and wall stress due to blood pressure. The endothelial cells sit on a basal lamina that consists of glycosaminoglycan and type IV collagen [12]. The endothelium controls vascular tone by interacting with the smooth muscle cells located in the next layer, the medial layer [13]. When the endothelium senses a change in the blood flow environment, it communicates with vascular smooth muscle cells to allow a change in vascular tone, constriction and dilation of the artery [13]. Another key structure component of this layer is collagen. Collagen fibers are oriented in the circumferential direction, creating structural integrity [14].

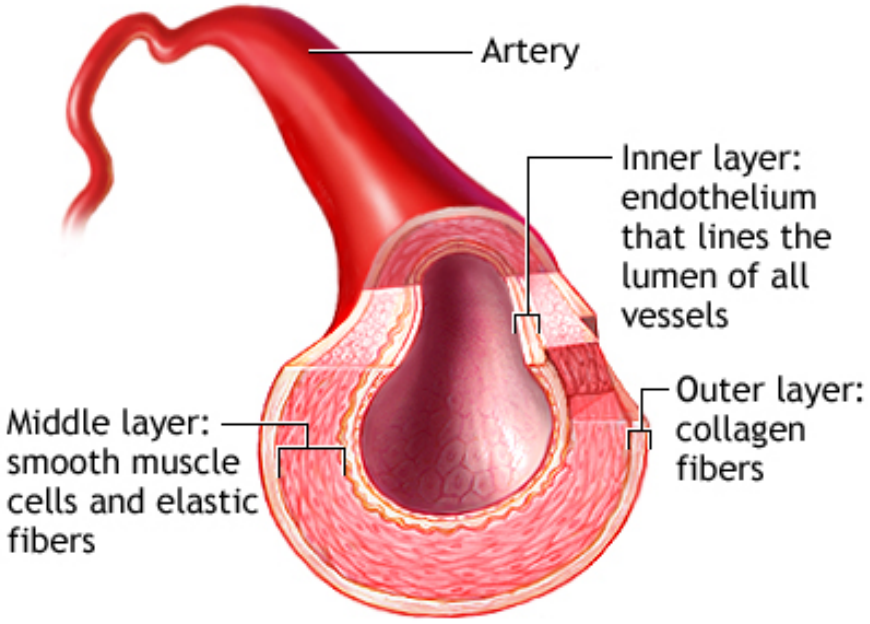

Figure 1.1 Display of the three artery layers: inner, middle, and outer layer.

However, in atherosclerotic arteries, smooth muscle cells migrate into the intima and deposit collagen, contributing to the progression of the plaque. The outer most layer with collagenous perivascular tissue is the adventitia consisting of type I collagen which is randomly oriented, unlike the medial layer (Figure 1.1). The adventitia is crucial for connecting arteries to other tissues in the body.

1.3 Atherosclerosis Initiation and Progression

Atherosclerosis is initiated by the accumulation of low-density lipoproteins (LDL) and triglyceride-rich lipoproteins in the intimal region. This accumulation results in the activation of proinflammatory atherogenic markers. There are many histological changes to the artery wall that occur during the development of atherosclerosis. The earliest sign of atherogenesis is known as the fatty streak or xanthoma. A fatty streak begins with the attachment of monocytes to the endothelial monolayer causing larger molecules to enter the intima. Once in the plaque, the monocytes differentiate into macrophages and take up the lipoproteins, giving rise to cholesterol ester-engorged foam cells. Over time, the macrophages can become dysfunctional and turn into foam cells [15]. At this nascent stage, the fatty streak does not impede blood flow or substantially protrude into the artery. The fatty streak alone does not cause any noticeable symptoms but can progress into a more dangerous phase [15].

The next phase of plaque progression is an intermediate lesion called pathological intimal thickening (PIT). In this phase, foam cells form, and smooth muscles migrate from the media into the intima of the vessel generating a collagen-enriched disorganized plaque progressing under the endothelial cell monolayer. Lipids and foam cells continue to accumulate and attract other immune cells such as leukocytes and t-cells [8]. This

attracts macrophages to the plaque area causing the plaque buildup to protrude into the vessel where blood is flowing [16].

After this phase, the plaque becomes more complicated and harder to treat. This is the final stage of plaque development before rupture. Once the intermediate lesion progresses into a fibrous cap atheroma with a fibrous cap of collagen and smooth muscle cells overlying a lipid rich necrotic core, the vessel starts to outward remodel to allow for blood flow to continue and maintain vessel diameter [16, 17]. This vulnerable plaque is now prone to rupture which can cause life threatening thrombosis. Once a region of the fibrous cap ruptures, the body registers this as an injury and the blood starts to clot. This can create an instant clot in the lumen that partially or completely blocks blood flow that causes a life-threatening event (Figure 1.2) [15].

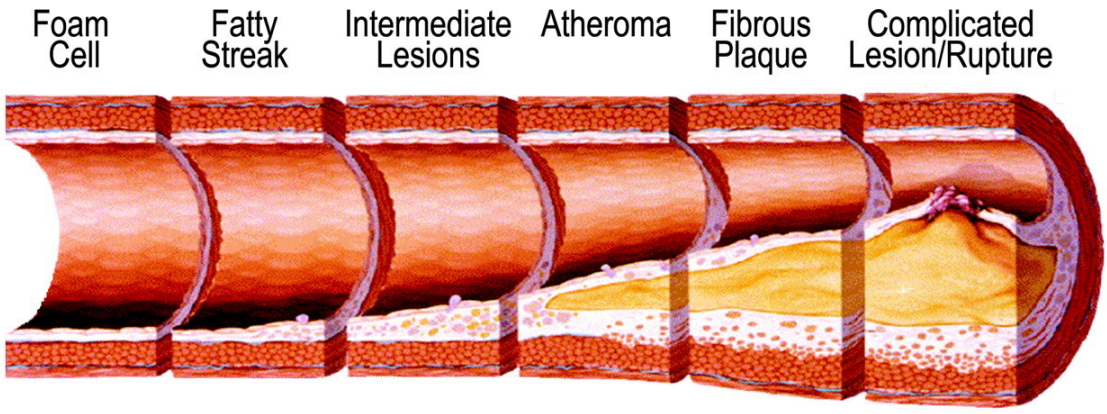

Figure 1.2. Display of plaque initiation and progression from normal to a more complicated plaque [18].

1.4 How the mechanical environment is associated with plaque development

Despite the many risk factors listed, blood flow is a key modulator of the atherosclerotic state of the artery. As blood flows over the endothelium, it imposes a mechanical stimulus, shear stress, which modulates the homeostatic environment [16, 17]. Wall shear stress (WSS) is a frictional force exerted parallel to the vessel wall that

can lead to alteration of the endothelium [19]. WSS is one of the most extensively studied parameters used to correlate hemodynamics to various aspects of cardiovascular disease. Importantly, WSS can vary considerably in space and time at any particular region of the vasculature [20]. This is especially true in diseased arteries with complex flow conditions and disturbed blood flow. Furthermore, WSS is a vector where magnitude and direction are important in biomechanical processes and mechanotransduction [17].

Countless studies have shown that blood flow can regulates beneficial cell signaling, such as anticoagulation, nitric oxide, inflammation, vascular tone, and vascular permeability [2, 21, 22]. Due to the different flow regimes across the vasculature, certain flow characteristics are more beneficial for promoting normal vascular health. Typically laminar flow is seen as atheroprotective at normal velocities and shear stresses (1.5 – 1.7 Pa), whereas disturbed blood flow that has low and/or multidirectional shear stresses (<1 Pa) promotes a dysfunctional and atherogenic response [17]. WSS is defined as the tangential stress on the endothelial surface of the arterial wall derived from the friction of flowing blood (Equation 1.1) [23]. It is directly proportional to the velocity of blood flow.

$$Eqn\ (1.1) \qquad \tau = \frac{4\mu Q}{R^3}$$

$$where\ \ \mu = viscocity, \qquad Q = flowrate, \qquad R = arterial\ radius$$

1.4.1 Localization of Atherosclerotic Plaques

Various WSS parameters have been linked with atherosclerosis complications. Therefore, it is well established that atherosclerotic plaques do not form randomly within the vasculature but can be found at predictable sites that exhibit disturbed blood flow (deviations in WSS magnitude and direction from normal) [1, 2, 7]. The regions with low and multidirectional wall shear stresses are typically seen in curvatures or bifurcations (Figure 1.3). In bifurcations, as flow splits, the velocity profile changes, causing high WSS at the inner walls of the split and low WSS at the outer walls where plaque is most likely to progress [2]. In curved vessels, as the flowing blood approaches the bend in vasculature, the inner wall of the curve experiences low WSS and the outer wall exhibits

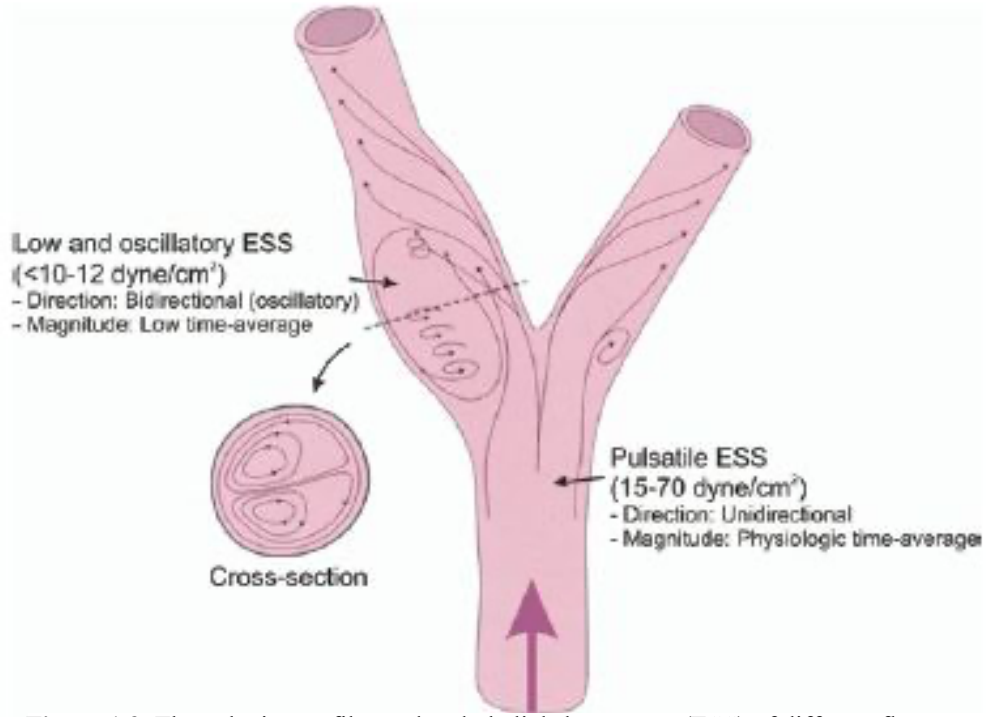

Figure 1.3. The velocity profiles and endothelial shear stress (ESS) of different flow environments found within the vasculature [1, 2].

high WSS causing plaque progression on the inner wall [2]. Therefore, examining the association between the WSS metrics of disturbed flow and plaque features in this mechanosensitive disease is important for understanding the initiation, progression, and

developing therapies. Many studies have confirmed that different WSS promotes different plaque phenotypes. The strong association between disturbed blood flow and the progression of atherosclerosis has been shown in many *in vivo* (mice, rabbits, pigs, and humans) and *in vitro* studies (HUVECs, HAECs, aortic ECs, etc.) [1, 2, 12, 21, 24-32]. Typically, low WSS has been shown to promote a vulnerable and unstable plaque whereas low and multidirectional WSS has resulted in a more stable plaque phenotype [25, 33].

1.4.2 Patient Studies

Researchers have extensively studied the correlation between WSS associated with disturbed flow and atherosclerosis. Differing low, medium, high, and multidirectional shear stress combinations can cause different mechanobiological responses. In patients with atherosclerosis, it is also important to understand how the hemodynamic environment will affect the plaque progression and destabilization.

The role of WSS was first examined in *ex vivo* studies of humans, where fatty streaks and atherosclerotic plaque were found to be distributed in regions of low WSS [19]. Later studies confirmed this phenomenon in human carotid artery bifurcations with laser Doppler velocimetry and MRI [19]. Additionally, cross sectional studies in humans using Doppler ultrasound demonstrated that patients with carotid artery plaques had a lower mean peak WSS compared to arteries devoid of plaque buildup, suggesting low WSS was associated with a more vulnerable plaque [19]. Low WSS causes a cascade of events promoting the vessel environment to become proinflammatory. This process begins when low WSS causes LDL cholesterol uptake, synthesis, and permeability [19, 23]. This is especially important for atherosclerosis in the context of hyperlipidemia

because LDL and cholesterol accumulate into the sub-endothelial layer, causing plaque to build. Low WSS plays a major role in regional localization of atherosclerosis and modulates gene expression through mechanotransduction processes inducing atherogenic behavior. Atherosclerotic plaques exposed to low WSS have consistently shown an increase in plaque burden, necrotic core area, lipid content, macrophages, smooth muscle cells, and a reduced fibrous cap thickness [27, 34, 35]. There have been many clinical studies examining how plaques will be affected based on low WSS. Samady *et al.* [27], evaluated twenty patients by taking a baseline measurement, and a 6 month follow up measurement with intravascular ultrasound (IVUS). The results demonstrated that in atherosclerotic arterial segments with low WSS, plaque area increased compared to intermediate and high WSS which showed plaque regression. Low WSS was also associated with an increase in necrotic core area and fibro-fatty area. Researchers suggested that patients with low WSS develop greater and more unstable plaques than patients that maintain a more intermediate WSS. In another prediction study of atherosclerosis by Stone *et al*., researchers examined low, intermediate, and high WSS in over 500 atherosclerotic patients where they measured a baseline, and then a final measurement a year later [35]. They also found that low WSS caused a more unstable plaque phenotype. They demonstrated that patients with coronary atherosclerotic plaque with increased plaque burden (>70%), decreased lumen area (<4mm^2), and the appearance of a TCFA had worsening clinical outcomes. The hazard for major adverse cardiovascular events at 3 years was high if all three of these lesion characteristics were present at baseline measurements [35]. These studies showed that not only is WSS important for the initiation of plaques, but it also plays an important role in disease

progression. Therefore, low WSS is a powerful local stimulus to examine the atherogenic processes and to understand how it effects the local environment.

Multidirectional WSS has also been studied in humans to examine the flow in bifurcations of arteries. In outer walls of bifurcations and downstream regions of stenotic arteries, cyclic WSS vectors appear from the oscillations in blood flow, thereby producing multidirectional WSS [1]. Due to the complex flow patterns caused by multidirectional WSS, time varying vortices and helical flows are formed. For example, shear stress at the walls of proximal internal carotid arteries changes the direction sharply during systole over a range of up to 70° [36]. Efforts to study the effects of off-axis flow patterns have become beneficial in understanding the complex changes that correlate with the initiation and progression of atherosclerosis. Furthermore, in human clinical studies using virtual histology intravascular ultrasound (VH-IVUS), Kok *et al*. investigated the clinical relevance of transverse WSS and other multidirectional WSS metrics on progression and destabilization of atherosclerosis in human coronary arteries in 20 patients. They took a baseline measurement of the coronary artery and a six month follow up measurement and found that multidirectional WSS was primarily involved in altering the plaque composition rather than the plaque size. Interestingly, low TAWSS with multidirectional flow had the largest and most predictive effect on plaque composition compared to higher TAWSS. Regions exposed to low and multidirectional flow showed more progression of necrotic core and dense calcium with the greatest impact on plaque progression. They concluded that multidirectional flow acts synergistically with time average WSS on plaque composition and plaque size [37].

1.4.3 Animal Studies

Many *in vivo* studies have shown the relationship between WSS and the progression of atherosclerosis. It is well established that disturbed blood flow promotes plaque initiation and progression. Currently the mouse model is the most frequently used species for atherosclerosis [38]. Apolipoprotein E-deficient (ApoE-/-) and LDL receptor-deficient (LDLr-/-) transgenic mice demonstrate a reasonable plaque development [28, 39]. LDLr-/- mice are known to spontaneously develop extensive and complex fibro-proliferative intimal lesions and ApoE-/- mice tend to have more heterogeneous and lipid rich lesions [40]. However, mice and humans differ based on lesion distribution. Hypercholesterolemic minipigs are also used to examine the initiation and progression of atherosclerosis. Using a pig model allows for more comparable hemodynamics and pathogenesis to humans [41]. Pigs also have a similar heart size and cardiovascular anatomy to humans [38, 41]. In a study by De Nisco *et al*. made a direct comparison between swine and human specific computational hemodynamics of coronary arteries. They found that there were no relevant differences in WSS based quantities, helical flow dynamics, and anatomical features between swine and human models [42]. Another study using a swine model of atherosclerosis, Chatzizisis *et al.* demonstrated that low WSS promoted plaque progression to high-risk atherosclerotic plaques characterized by large lipid cores, inflammation, a thin fibrous cap, and elastic lamina degradation [1]. Therefore, these results demonstrate that regions of low WSS have more extensive and vulnerable plaques than other regions of disturbed blood flow, and thus are the major contributor to morbidity compared to multidirectional WSS.

Researchers have induced certain WSS profiles using different techniques in animal models, such as inserting a shear stress modifying perivascular collar [40, 43], perivascular casts [44], or cuffs [28] all with the same goal of disrupting the flow environment. Animals are typically placed on a high fat diet, and a surgical method is used to disrupt the hemodynamic environment, causing the animals to develop lesions rapidly. By establishing a cuffed mouse model of atherosclerosis Cheng *et al*. used ApoE^{-} knockout mice on a high fat atherogenic diet [25, 33, 45]. Instrumentation of this cuff allows for three regions of disturbed blood flow with low WSS in the upstream regions towards the aortic arch, high shear stress in the cuff, and low and multidirectional WSS downstream of the cuff toward the carotid bifurcation. They demonstrated that the low WSS region developed larger atherosclerotic lesion with high lipid content, fewer smooth muscle cells, lower collagen content, and high outward remodeling. Furthermore, they found high expression of inflammatory markers such as VCAM-1, ICAM1, C-reactive protein, IL-6, and MMP [25]. These results demonstrated that low WSS produces a more vulnerable phenotype than multidirectional WSS and were much less stable than the other disturbed blood flow regions.

As stated, multiple studies have used hypercholesterolemic minipigs instrumented with a shear modifying stent. In a study completed by Hoogendoorn *et al*. researchers found four main correlations between multidirectional WSS and disease progression; (i) plaque initiation and progression are associated with low time average WSS and high multidirectional WSS in both mildly diseased and advanced disease pigs, (ii) the greatest plaque burden growth was observed in regions with low WSS turning into high WSS, while multidirectional WSS sustained plaque growth area, suggesting atherosclerotic

plaques reached a more stable phenotype under these complex flow conditions, (iii) plaques with a vulnerable composition were most often developed in the low WSS region, and (iv) multidirectional WSS metrics have a positive predictive values for the development of plaque [26]. Furthermore, pigs instrumented with a stenotic stent demonstrated that in the low flow region upstream of the stent, thin cap fibroatheroma persisted over the duration of the study compared to other disturbed flow regions [28]. These results support that lowered shear stress appears to be the principal flow disturbance needed for a fibrous cap. Therefore, animal models have proven invaluable in understanding the pathophysiology of atherosclerosis and by using these animal models, atherosclerosis initiation and progression in disturbed flow regions can be studied faster and more efficiently.

1.4.4 Shear Stress Metrics

As stated above, to characterize the WSS, many metrics have been used. Low and/or multidirectional disturbed blood flow have been quantified with different shear stress metrics to identify plaque localization regions. Typically, disturbed blood flow is characterized by variations in WSS from the time average vector. Time average WSS (TAWSS) is the average of the magnitude of the instantaneous WSS vectors over one cardiac cycle (Equation 1.2) [20]. This metric provides the magnitude of WSS but not the direction of flow.

$$Eqn.(1.2) \qquad TAWSS = \frac{1}{T}\int_0^T |\tau| dt, \ \ where\ |\tau| = \sqrt{\tau_x^2 + \tau_y^2 + \tau_z^2}$$

Additionally, the magnitude of the mean WSS (MagMeanWSS) is another metric that examines the magnitude of the average of the instantaneous WSS vectors over one cardiac cycle (Equation 1.3).

$$Eqn\ (1.3) \qquad |\tau_{mean}| = \left|\frac{1}{T}\int_0^T \tau dt\right| \tag{1.3}$$

Another metric that correlates disease progression with WSS is the oscillatory shear index (OSI). Since atherosclerosis tends to form on the outer walls of carotid arteries, OSI was introduced to examine flow reversal (Equation. 1.4). This metric is the ratio between MagMeanWSS and TAWSS to quantify the degree of flow multidirectionality. Thus, OSI indicates if the flow is forward. This inverse relationship with MagMeanWSS measures the deviation of WSS from its dominant direction, however, it does not determine how much of a deviation there is. Moreover, OSI helps to understand the magnitude and direction of flow [20].

$$Eqn\ (1.4) \qquad OSI = \frac{1}{2}\left(1 - \frac{\left|\frac{1}{T}\int_0^T \tau dt\right|}{\frac{1}{T}\int_0^T |\tau| dt}\right) = \frac{1}{2}\left(1 - \frac{MagMeanWSS}{TAWSS}\right) \tag{1.4}$$

The different disease patterns and flow environments then led to the introduction of an additional shear stress metric, transverse WSS (TransWSS). Researchers felt that the multidirectional flow environment was not fully captured by just utilizing OSI and demonstrated that there is a rotational flow also associated with plaque development over the cardiac cycle. TransWSS is the average over the cardiac cycle of WSS components perpendicular to the temporal mean WSS vector (Equation 1.5) [20]. This metric provides

the measurement for the biological hypothesis that vascular environment is also affected by crossflow.

$$Eqn\ (1.5) \qquad transWSS = \frac{1}{T}\int_0^T \left| \tau \cdot \left(n \times \frac{\int_0^T |\tau| dt}{\left| \int_0^T \tau dt \right|} \right) \right| dt = \frac{1}{T}\int_0^T \left| \tau \cdot \left(n \times \frac{\tau_{mean}}{|\tau_{mean}|} \right) \right| dt$$

1.5 Endothelial cell function is a critical pathophysiological factor in atherosclerosis

Differences in WSS triggers an inflammatory response. Interestingly, the endothelial cell monolayer is the barrier that senses this disturbance causing the cells to become dysfunctional. Thus, atherosclerosis tends to form in bifurcations or curvatures, where endothelial cells express a more dysfunctional phenotype. The endothelium is believed to play a crucial role in vascular homeostasis [46]. It is sensitive to the blood flow and a key regulator of the atherosclerotic environment, controlling the degree of inflammation the vessel experiences. Many of the atheroprotective signals are activated by steady normal flow, which downregulates a number of inflammatory markers in endothelial cells [47]. Vascular endothelial cells from the inner lining of blood vessels and act as a barrier that regulates exchanges between the blood and tissue. A normal healthy endothelium regulates vascular tone, structure and exerts anticoagulant and fibrinolytic properties (Figure 1.4A). Therefore damage, or changes in flow and shear stress to the endothelium, upsets the balance between vasoconstriction and vasodilation, angiogenesis, anticoagulation and thrombosis, and permeability, which initiates many processes that promote atherosclerosis (Figure 1.4B).

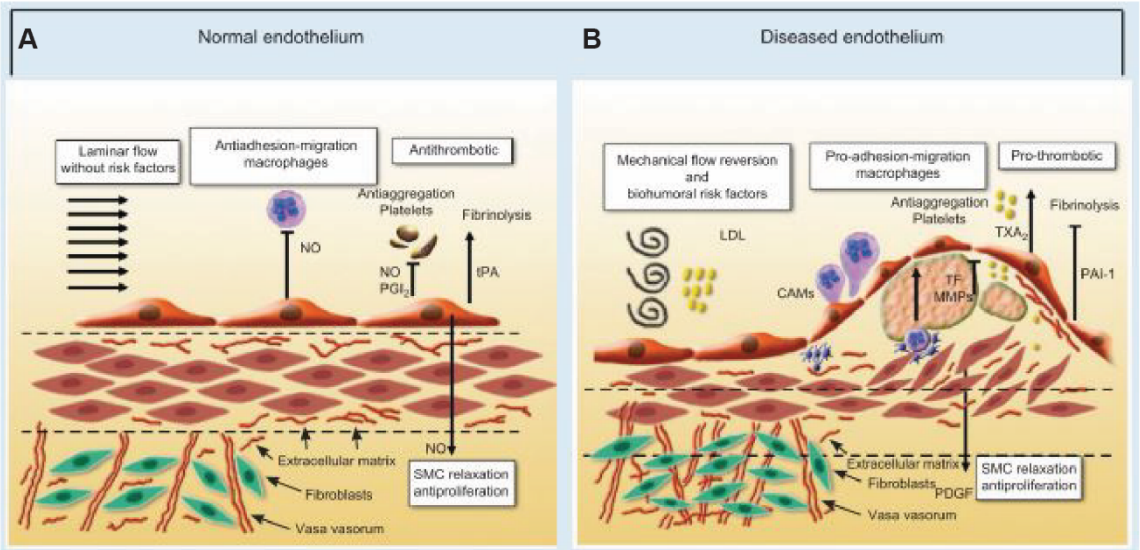

Figure 1.4. Normal endothelium compared to endothelial dysfunction and development of atherosclerosis. **(A)** Normal endothelium under laminar flow conditions. **(B)** Dysfunctional endothelium with disturbed flow [3].

1.5.1 Disturbed blood flow causes a dysfunctional endothelium

Research has shown that inflammatory cells localize to arterial segments with disturbed blood flow in early-stage atherosclerotic plaque and recent developments have shown that cytokines and inflammatory mediators promote the progression of local inflammation through plaque formation [48]. Current understanding of inflammation provides insight into the mechanisms involved in the process of cytokine and leukocyte recruitment which does not occur in the presence of a normal endothelium. Disturbed blood flow changes the cellular alignment of endothelial cells and increases their permeability to large molecules [49]. Lipids are the first molecules that penetrate the endothelium [3]. This causes an immune response, recruiting inflammatory cells such as monocytes, t-lymphocytes, dendritic cells, etc. into the intima to scavenge lipids. Once this happens, NF-kB is translocated to the nucleus and various atherogenic genes (VCAM-1, ICAM-1, E selectin, MCP-1, cytokines, etc.) adhere to the endothelial cell surface [2]. For example, a short time after starting an atherogenic diet in animal

experiments, areas of arteries that contain endothelial cells with adhesion molecules (VCAM-1) that bind leukocytes, within regions of disturbed blood flow, mediate endothelial dysfunction [48]. Libby *et al.* states that within one week of starting an atherogenic diet, rabbit's endothelial cells express VCAM-1 which initiates plaque progression towards an atheroma [48]. Once the endothelial barrier is dysfunctional, increased permeability causes a cascade of inflammatory events. Monocytes and other immune cells adhere to the endothelial cell surface and settle, they penetrate the sub-endothelial region and differentiate into macrophages to attack circulating lipid molecules [3, 22]. As lipids in the form of LDL are engulfed and transformed into foam cells, they become trapped which promotes the production of reactive oxygen species [13, 27, 32]. Low and multidirectional WSS attenuates nitric oxide by reducing the bioavailability and decreasing eNOS expression which exposes the endothelium to an atherogenic response. Deficits in nitric oxide is the hallmark of endothelial dysfunction and a contributor to atherosclerosis. Many of the endothelial cell functions are dependent on nitric oxide production. Nitric oxide opposes the effects of endothelium derived vasoconstrictors and inhibits oxidation of LDL [22]. It also inhibits platelet adherence and aggregation, leukocyte infiltration, proliferation of smooth muscle cells, and expression MCP-1 and VCAM-1 [19, 22].

The direct effects of WSS on endothelial cells have been elucidated primarily by *in vitro* experiments that examine how endothelial cells respond to the flow environment. Disturbed flow has been shown to induce polygonal cobblestone endothelial cell morphology and loss of alignment [19]. Additionally, low WSS accelerates cell turnover that leads to increases in lipid uptake and widening of gap junctions between non-

uniform endothelial cells [19, 29, 50]. This causes an increase production of reactive oxygen species and enhances gene expression of oxidative enzymes at the endothelial cell surface. For example, Wang *et al.* investigated how disturbed flow with complex changes in the direction of flow might affect the alignment of bovine aortic endothelial cells [36]. By using a parallel plate system that enabled changes in flow direction of 45°, 90°, 135°, 180°, and 360° researchers showed that different flow angles stimulate activation of distinct cellular pathways [36]. Multidirectional disturbed flow induced higher reactive oxygen species and lower nitric oxide compared with parallel flow. Additionally, flow that was perpendicular to the cells' direction stimulated reactive oxygen production and the translocation NF-KB to the nucleus, whereas parallel flow had little effect [36, 51]. This increase in inflammation can stimulate vascular smooth muscle cells migration from the media to the intima, potentially causing the formation of a vulnerable plaque with a fibrous cap. Furthermore, disturbed flow induces expression and upregulation of several inflammatory cytokines and receptors consistent with a proinflammatory response [2]. These features contribute to vulnerable plaque's rupture prone phenotype and likelihood of thrombotic complications or rapid progression. Thus, these results implicate the correlation of disturb flow and disease progression, demonstrating that disturbed flow does indeed have atherogenic effects when stimulating the aligned and elongated endothelial cells [36, 52].

1.5.2 Normal flow is atheroprotective and beneficial to endothelial cells

As stated, normal blood flow occurs in straight arterial segments up to a certain velocity and remain protected from atherosclerosis with a healthy endothelial phenotype [19]. One of the earliest observations of sustained normal steady flow with normal

physiological WSS demonstrated that endothelial cell morphology and alignment in the axial direction of flow promoted healthy functions and an atheroprotective phenotype [19]. In these straight portions of the vasculature, endothelial cells align and elongate parallel to the direction of flow to reduce resistance and activate signaling cascades that protect them from becoming dysfunctional. For *in vivo* work, using an *en face* technique, studies have been able to stain tissue and cells for VE-Cadherin to identify normal laminar flow regions. Laminar WSS produces anti-inflammatory effects through regulation of endothelial gene expression by transcription factors such as Kruppel-like factor 2 (KLF2), thereby controlling permeability, inflammation, thrombosis/hemostasis, vascular tone, and blood vessel development or angiogenesis to promote atheroprotection [19]. *In vitro* work has shown that endothelial cells can be stimulated with laminar steady flow using microfluidics, an orbital shaker, or parallel plates. In a microfluidics experiment by Mohammed *et al*. researchers used pulsatile flow to assess the mechanobiology of human aortic endothelial cells and found that pulsatile shear stress influenced the atheroprotective behavior and orientation of the cells as well as the size and shape of the nucleus [53]. In a study by Sahni *et al*., research from our lab demonstrated that human umbilical vein endothelial cells (HUVECs) seeded on a well plate and placed on an orbital shaker increased atheroprotective markers (eNOS, THBD, and KLF-2) and decreased atherogenic markers (ET-1, CTFG, and CAV-1) in a the laminar flow region at the periphery of the well compared to the multidirectional disturbed flow at the center of the well [32]. Interestingly, no study has considered the idea that differing beneficial flows, such as continuous or pulsatile, at normal WSS have the same biological trends but different degrees of activation. No study has quantified the

differences between flow profiles on the endothelium, instead, WSS and flow is an afterthought. Thus, it is important to quantify the biological response of endothelial cells to flow generated by different mechanisms (e.g., orbital shaker versus microfluidics) over a range of WSS magnitudes and directionality. This could provide a foundation for creation of new therapeutics based on activation of mechanosensitive signaling pathways.

1.6 Treatments for atherosclerosis

Atherosclerosis is the leading cause of death due to the major health consequences associated with it (ie. stroke, ischemic heart disease, myocardial infarction etc.). The number of patients increases every year and if treatment in not started early on, every other patient dies within 10 years [54]. However, if addressed early, patients are offered various therapeutic techniques with different efficiencies. Currently, there are numerous strategies in the treatment and prevention of atherosclerosis focusing on risk factors of the disease, such as lipid metabolism, inflammation, hypertension, and others, however, none of them are completely effective treatments in disease regression because treatment does not target the endothelial mechanical environment.

1.6.1 Current non-invasive treatments

As mentioned previously, atherosclerosis is a metabolic disorder characterized by hyperlipidemia and inflammation. The disorder of lipid metabolism in atherosclerosis is expressed as hyperlipidemia. This can appear in patients as increases in cholesterol, triglycerides, and phospholipids. Lipids are transported by the blood in the form of lipoproteins: very-low-density lipoprotein (vLDL), low-density lipoprotein (LDL), and high-density lipoproteins (HDL). Additionally, human blood plasma lipids are present with cholesterol, triglycerides, phospholipids, and fatty acids [54].

For more than a century, the link between cholesterol and atherosclerosis has been established [55]. In patients with cardiovascular disease, typically lipid disturbances occur where total cholesterol and LDL are elevated. These proteins can easily penetrate the endothelium and initiate the atherosclerotic process. Therefore, the leading therapy for treating atherosclerosis is a class of drugs called statins that alter lipid metabolism. Specifically, these drugs reduce the amount of cholesterol in the blood.

In clinical studies, the high efficacy of statins in reducing cholesterol and LDL has been well studied and examined. This gold standard drug decreases the frequency of recurrent complications of cardiovascular disease by 25-40% and reduces mortality [54]. Statins work as inhibitors of the enzyme known as Hydroxymethylglutaryl (HMG)-CoA reductase, which is a key enzyme in the synthesis of cholesterol [55]. Once administered, statins cause a decrease in intracellular cholesterol content in the blood, thereby increasing the number of membrane receptors to LDL in the liver to bind and remove LDL from the blood stream. This then reduces the concentration of total cholesterol and triglycerides [54].

In addition to decreasing cholesterol, statins also improved endothelial cell functions by preserving eNOS, thus leading to vasodilation. This may also help to reduce plaque vulnerability by inhibiting myocyte infiltration and reduce the secretion of metalloproteinases [56]. Furthermore, statins have shown to reduce inflammation by decreasing C-reactive protein concentrations and inhibiting platelet aggregation and the proliferative activity of smooth muscle cells [56].

There are many positive outcomes of this commonly used therapy to treat atherosclerosis, however there are also adverse effects after the treatment with statins due

to the untargeted and circulatory nature of how this drug is used. One concern of prescribing statins is the liver toxicity. Between 1987 and 2000, the FDA receive a notice of 30 cases of sever liver toxicity, therefore exerting caution in prescribing statins to patients with certain illnesses [54]. Additionally, in recent years, there has been evidence of a 20-30% increased risk with being diagnosed with diabetes following the use of statins [54]. Another more detrimental side effect includes muscle atrophy, stiffness, or breakdown with possible damage to the renal tubules [54]. Other side effects are neurological and degenerative diseases, as well as a 9-27% risk for developing cataracts. Importantly, they do not cause remission or cure the disease and they are not targeted to regions of plaque development. With that in mind, there is a need for a more targeted effective therapy, however, lipid metabolism is a necessary research field for understanding and developing atherosclerosis treatments and prevention.

1.6.2 Current targeted treatments

Despite advances in medical technology, atherosclerosis still has a high risk of recurrence and death, which has motivated researchers to find a more effective method of treatment, including preventative procedures. Although statins are the most used treatment, sometimes more aggressive therapy is needed to treat atherosclerosis. If patients have severe symptoms or a blockage, they may need a higher risk procedure or surgery. These can include angioplasty and stent placement, endarterectomy, and coronary bypass graft surgery.

Angioplasty is a procedure that helps to open a blocked artery. The first successful balloon angioplasty took place in 1977 and is still one of the most frequently used treatments in vascular emergencies of the heart and peripheral circulation [54]. This

process involves a catheter being inserted into a blood vessel and guided to the blockage. Then a balloon on the tip of the catheter can be inflated to open the diseased area of the artery [57]. Occasionally, a meshed stent is then placed to keep the artery from collapsing, however, recently, angioplasty has been suggested as a safer alternative to angioplasty plus stenting due to the disruption of the mechanical environment and likelihood of disease recurrence and death [58]. Furthermore, it has come to light that stenting in many clinical studies from 2011-2017 resulted in more strokes, adverse cardiac events, and death [54].

Endarterectomy is a surgery used to remove plaque from the artery walls, typically done on the carotid arteries. Removing plaque that is causing narrowing in the arteries can improve blood flow and reduce the risk of stroke [57]. According to the AHA, endarterectomy is three times as effective as medical therapy alone in reducing incidences of stroke with patients containing stenosis of 70%-90%. However, as effective as this treatment is, there are many inherent risks associated with it. 5.5% of patients had wound hematomas, 21% of patients have shown an increase in blood pressure after the procedure (does not including patients with high blood pressure prior to surgery), doubled cerebral blood flow causing extreme unilateral headaches, 50% of patients had intracerebral hemorrhaging, and seizures are reported in 3% of patients 5-7 days after the procedure [59]. Therefore, even though this therapy is one of the most common for targeting a diseased region, it still has high risks associated with it.

Finally, occasionally a coronary artery bypass graft is needed to completely replace a blocked artery. For this procedure, a surgeon takes a healthy blood vessel from another part of the body to create a new path for blood in the heart. The blood is then

redirected around the blocked or narrowed artery into the healthy artery [57]. This procedure requires open-heart surgery, which is extremely high risk, and is typically only done in patients with multiple narrowed arteries.

Currently, therapies for atherosclerosis are either untargeted with a noninvasive component, or targeted and extremely invasive. There is a need for a targeted non-invasive therapy that not only can be administered frequently, but also results in disease remission and plaque regression. Many studies have shown that atherosclerosis is a mechanical related disease, however there is no therapy that utilizes mechanosensitive pathways to treat atherosclerosis. Despite the atheroprotective nature of laminar flow, no therapy has leveraged the mechanosensitive nature of the endothelium. By introducing a beneficial mechanical stimulus to atherosclerotic arteries, targeting the endothelium, a therapy can be developed that promotes plaque regression.

1.6.3 Developing a mechanical therapy

Currently, therapies for atherosclerosis either use pharmaceuticals to address systemic conditions such as hypercholesterolemia or employ highly invasive surgical procedures to target the diseased artery. There is a need for a therapy that is both noninvasive and targeted. Many studies have shown that atherosclerosis is a mechanical-related disease, however there is no therapy that utilizes mechanosensitive pathways to treat atherosclerosis. Despite the atheroprotective nature of laminar flow, no therapy has leveraged the mechanosensitive nature of the endothelium. By introducing a beneficial mechanical stimulus to atherosclerotic arteries, targeting the endothelium, a therapy can be developed that promotes plaque regression.

CHAPTER 2

Smooth Muscle Cells Affect Differential Nanoparticle Accumulation in Disturbed Blood Flow-Induced Murine Atherosclerosis

Published in PLoS One 2021

2.1 Abstract

Atherosclerosis is a lipid-driven chronic inflammatory disease that leads to the formation of plaques in the inner lining of arteries. Plaques form over a range of phenotypes, the most severe of which is vulnerable to rupture and causes most of the clinically significant events. In this study, we evaluated the efficacy of nanoparticles (NPs) to differentiate between two plaque phenotypes based on accumulation kinetics in a mouse model of atherosclerosis. This model uses a perivascular cuff to induce two regions of disturbed wall shear stress (WSS) on the inner lining of the instrumented artery, low (upstream) and multidirectional (downstream), which, in turn, cause the development of an unstable and stable plaque phenotype, respectively. To evaluate the influence of each WSS condition, in addition to the final plaque phenotype, in determining NP uptake, mice were injected with NPs at intermediate and fully developed stages of plaque growth. The kinetics of artery wall uptake was assessed *in vivo* using dynamic contrast-enhanced magnetic resonance imaging (DCE-MRI). At the intermediate stage, there was no difference in uptake between the two WSS conditions, although both were different from the control arteries. At the fully-developed stage, however, nanoparticle uptake was reduced in plaques induced by low WSS, but not multidirectional WSS. Histological evaluation of plaques induced by low WSS revealed a significant inverse correlation between the presence of smooth muscle cells and nanoparticle accumulation, particularly at the plaque-lumen interface, which did not exist

with other constituents (lipid and collagen) and was not present in plaques induced by multidirectional WSS. These findings demonstrate that NP accumulation can be used to differentiate between unstable and stable murine atherosclerosis, but accumulation kinetics are not directly influenced by the WSS condition. This tool could be used as a diagnostic to evaluate the efficacy of experimental therapeutics for atherosclerosis.

2.2 Introduction

Atherosclerosis is a chronic inflammatory disease characterized by the development of plaques composed of lipids and immune cells within the artery wall. It is the leading cause of death worldwide [28]. The clinical significance of the plaque is typically based on the degree of lumen stenosis determined from angiography. However, the plaque phenotype that causes most deaths due to vulnerability to rupture does not always cause a severe stenosis [60]. While other imaging modalities can be used to better quantify additional features of plaque phenotype (e.g., intravascular ultrasound), all of them require invasive catheterization that carries risk of major complications to the patient [61]. Another problem with diagnosis of high-risk plaques is that plaque progression to rupture is a highly nonlinear process, where plaque features can change rapidly in the weeks to months before rupture [62, 63]. Thus, there is a need for a noninvasive diagnostic tool that would allow more frequent imaging of patients considered intermediate-to-high risk for myocardial infarction or ischemic stroke [63]. Given the dynamic nature of plaque evolution, such a tool could also be impactful in research that employs animal models to characterize plaque progression and regression. To address this need, contrast-enhancing nanoparticles (NPs) can be tracked in atherosclerotic arteries to relate accumulation in plaques to plaque phenotype and

changes with progression. While studies have examined NP accumulation in atherosclerosis [64], in general, few have looked at changes with plaque progression and the large range of NP properties alone, including size, targeting ligands, and surface coating, warrant additional studies.

Another factor that might influence NP accumulation is the blood flow environment, but no study to our knowledge has examined this relationship. In addition, blood flow is an important determinant of the susceptibility of an arterial segment to atherosclerosis [2, 25, 27, 35]. This connection stems from the tangential load that blood flow imparts onto the endothelium called wall shear stress (WSS). In straight arterial segments, blood flow is laminar and the associated WSS promotes normal endothelial cell functions that are atheroprotective. In contrast, arterial segments around bifurcations or the inner curvature of highly curving arteries cause blood flow to be disturbed and the associated WSS is low in magnitude and/or varying in direction over the cardiac cycle (i.e., multidirectional), which causes an atherogenic endothelial phenotype [39, 65, 66]. WSS is not only important in atherosclerosis initiation, but also progression, where different WSS conditions have been shown to influence the development of different plaque phenotypes [1, 12, 27, 35].

We have previously reported that implantation of blood flow-modifying stents within the coronary arteries of transgenic hypercholesterolemic pigs caused the development of advanced plaques, wherein low WSS promoted thin cap fibroatheroma and multidirectional WSS was associated with the development of thin and thick cap fibroatheroma and pathological intimal thickening [28]. This study was motivated by a well-established ApoE$^{-/-}$ mouse model that places a blood flow-modifying constrictive

cuff around one of the carotid arteries to induce disturbed flow and cause the development of advanced plaques [25, 67]. Recently, we quantified the WSS characteristics in the arteries of ApoE$^{-/-}$ mice instrumented with a cuff *in vivo* using micro-CT imaging and Doppler ultrasound to obtain each cuffed artery geometry and blood velocity, respectively, and then performed computational fluid dynamics to compute the associated WSS [39]. We found that the cuff reproducibly induced low WSS in the upstream region, high WSS within the cuff, and multidirectional (including oscillatory) WSS in the downstream region of each instrumented artery. These results aligned with those previously reported by the seminal study introducing this mouse model, which used an idealized CFD model to estimate WSS in the instrumented artery [25]. This study also showed that 9 weeks after cuff placement, upstream plaques exhibited increased lipids and inflammatory mediators, together with decreased smooth muscle cells and collagen that localized to the cap region, similar to an unstable advanced plaque phenotype in humans, whereas downstream plaques showed the opposite trends and were more similar to a stable advanced plaque phenotype [25]. These results have been corroborated by several other studies [67-70].

Herein, we employed this well-established ApoE$^{-/-}$ mouse model to characterize differential accumulation of folic acid-coated gadolinium (FA-Gd) NPs between the two atherogenic WSS conditions induced by the cuff, low and multidirectional. Folic acid was chosen for the surface coating to improve colloidal stability, improve magnetic resonance imaging (MRI) enhancing properties, and take advantage of the folate receptor on activated macrophages that accumulate at the plaque site [71]. The kinetics of NP uptake into the plaques were determined *in vivo* using dynamic contrast-enhanced (DCE)-MRI.

To better separate the influence of WSS versus plaque phenotype on NP accumulation, mice were injected with NPs and imaged at both intermediate (5 weeks) and fully-developed (9 weeks) stages of plaque growth. At the endpoint of the study, histology was performed to characterize plaque features, which were individually correlated to NP accumulation.

2.3 Materials and methods

2.3.1 Synthesis of FA-Gd NPs

FA-Gd NPs were formulated using a modified polyol synthesis method [72]. The NPs were formed by adding 2 mmol gadolinium chloride hydrate ($GdCl_3xH_2O$) into 30 mL of triethylene glycol and heated to 80°C until the dissolution of precursors was achieved. The mixture was combined with 6 mmol sodium hydroxide and continuously stirred for 4 h at 180°C. The NPs were coated with 4 mmol folic acid ($C_{19}H_{19}N_7O_6$) and continuously stirred for 12 h at 150°C. Once cooled, the synthesized NPs were washed three times in deionized water from a Millipore water purification system. All chemicals were purchased from Sigma-Aldrich.

2.3.2 NP relaxivity characterization

R_1 relaxivity of NPs was measured using a 9.4T (400 MHz) 89 mm vertical bore magnet (Varian, Walnut Creek, CA) with a 4 cm Millipede RF imaging probe and triple axis gradients (100 G/cm max). A fast spin echo sequence was used with the following parameters: 7 repetition time, TR, values from 200-2000 ms in 300 ms increments, TE = 32.42 ms, ETL = 16, 25x25x3 mm^3 field of view (FOV), and a 128x128 data matrix. The saturation recovery method was utilized to measure relaxation time, T_1, of each NP concentration based on MR signal and the equations 2.1 and 2.2:

$$S = S_0\left(1 - e^{-\frac{TR}{T_1}}\right) \quad \text{(Eqn. 2.1)}$$

In which S is MR signal at a given voxel and S_0 is the signal of the given voxel at saturation. Relaxivity, r in $mM^{-1}s^{-1}$, was then calculated as:

$$R_1 = r * C + b \quad \text{(Eqn. 2.2)}$$

Where $R_1 = T_1^{-1}$, C is the concentration of NP and b is the y-intercept of the line.

2.3.3 Mouse Model

This study was carried out in strict accordance with the recommendations in the Guide for the Care and Use of Laboratory Animals of the National Institutes of Health. The protocol was approved by the Institutional Animal Care and Use Committee (IACUC) of the University of Nebraska-Lincoln (Project ID: 1581 and 2007). All surgeries were performed under isoflurane gas anesthesia (2-3% induction and 0.25-2% for maintenance) and buprenorphine (1 mg/kg via subcutaneous injection) was given at the time of surgery to provide sustained release of analgesia for 72 hrs. A total of 18 female $ApoE^{-/-}$ mice at 11 weeks of age were placed on an atherogenic diet (Envigo) for two weeks and then instrumented with a blood flow-modifying cuff (Promolding) around the left carotid artery that tapers from 500 μm at the inlet to 250 μm at the outlet. This cuff induces three regions of disturbed flow and associated WSS: low WSS upstream, high WSS within, and multidirectional WSS downstream of the cuff [39]. Previous studies have demonstrated that atherogenic flow conditions cause development of advanced plaques consistent with an unstable phenotype in the upstream region and a stable phenotype in the downstream region (no plaque forms in the cuff as high flow is atheroprotective) within 9 weeks of cuff placement [25, 67]. To evaluate nanoparticle accumulation at an intermediate and the fully-developed stage of plaque growth, five of

these mice were injected with FA-Gd NPs and imaged with DCE-MRI at 5 and 9 weeks after cuff placement. Healthy 6-week-old C57BL/6 mice (four total arteries obtained from two mice) on a normal chow diet were also injected with nanoparticles and imaged at a single time point as an additional control. The remaining $ApoE^{-/-}$ mice, in addition to those injected with NPs, were used for histological evaluation of plaque size and constituents at 5 versus 9 weeks and upstream versus downstream plaques.

2.3.4 DCE-MRI and mouse imaging protocol

DCE-MRI was performed on mice herein as previously described [72, 73]. Briefly, mice were induced with 2% isoflurane gas and breathing rates were monitored by a pressure-based sensor (SA Instruments), maintaining 50 to 80 breaths per minute over the course of the imaging sequence. Mice were affixed in a cylindrical animal holder to maintain head and body position during MR imaging. A 30-G needle was connected to a syringe via catheter and inserted into a lateral tail vein and secured with surgical tape. Mice were injected with 100 μL FA-Gd NP solution followed by a 100 μL bolus of PBS to flush excess NPs from the catheter. DCE-MRI was performed using a 2-D gradient echo multi-slice sequence with two flip angles for calculation of R_1 [73] and generation of K^{trans} maps, which indicates the NP permeation from the plasma into the arterial wall, based on the Patlak model, a two-compartment pharmacokinetic model assuming unidirectional contrast transfer. Two baseline scans were performed to calculate T_1 values prior to injection with the following parameters: TR = 138 ms, TE = 3.48 ms, flip angles of 10° and 30° respectively, 2 averages, 256x256 data matrix, 20 slices each with a 23x23x0.5 mm^3 FOV for a total scan time of 53 seconds. Post-contrast scans all used a flip angle of 30° with the same parameters as above. After completion of baseline scans, NPs were injected through the tail vein catheter, followed by 45 minutes of post-contrast

image collection. The K^{trans} maps were then generated using a custom program in MATLAB (R2020b). Pharmacokinetic properties of the NPs were determined based on a modification of our previously described methods, using the Patlak model instead of the reference region [73]. Briefly, arterial input functions were collected from ROIs typically drawn around the carotid arteries and fit to a bi-exponential model using a nonlinear least squares algorithm in MATLAB.

2.3.5 Histological analysis

To assess the development of atherosclerotic plaques at 5 (n=8 mice) and 9 (n=10 mice) weeks after cuff placement, the carotid arteries of all mice were prepared for histological evaluation. Mice were intracardially perfused with 35 ml of saline solution and then perfusion-fixed with 35 ml of 4% paraformaldehyde at mean arterial pressure. Both carotid arteries were excised still attached to the aortic arch and embedded in OCT. The tissue was then snap frozen in a mixture of isopentane (ThermoFisher) and dry ice. Cryosections with a thickness of 8 μm were serially collected from the innominate bifurcation in the right (control) common carotid artery, which aligned with a similar position in the far upstream region of the adjacent left (instrumented) common carotid artery (2-3 mm from the aortic arch), to the carotid bifurcation. Sections were collected in a way to allow assessment of multiple stains over the length of the arteries. Co-registration of the histology sections to the DCE-MRI images and associated K^{trans} maps was done using the cuff as a landmark, which was easily identifiable in both MRI and histology, the latter because the cuff region remains non-diseased due to the presence of high WSS—plaques develop immediately upstream and downstream of the cuff in the atherogenic flow regions of the instrumented artery (Figure 2.1). Four plaque constituents were evaluated. Oil red O (Sigma) was performed for analysis of lipid and picrosirius red

(Sigma) for analysis of collagen. These basic stains were imaged at 10x magnification with a Zeiss Axio Observer 5 microscope. Two immunostains were also performed to evaluate the presence of smooth muscle cells and mitotic cells, respectively. Smooth muscle cells were detected using a primary antibody directed against alpha-smooth muscle actin (α-SMA) (rabbit polyclonal anti-αSMA at 1:250, Abcam #ab5694) and an Alexa Fluor 594 preadsorbed secondary antibody (goat polyclonal anti-rabbit at 1:1000, Abcam #ab150084). Mitotic cells were detected using a primary antibody directed against Ki67 (rabbit polyclonal anti-Ki67 at 1:100, Abcam #ab15580) and an Alexa Fluor 647 secondary antibody (goat polyclonal to rabbit at 1:750, Abcam #ab150079). Both immunostains were counterstained with DAPI (0.0025%, Abcam #ab228549). Immunostained-sections were imaged at 20x magnification with a confocal microscope. Confocal parameters were held constant over all sections of all mice.

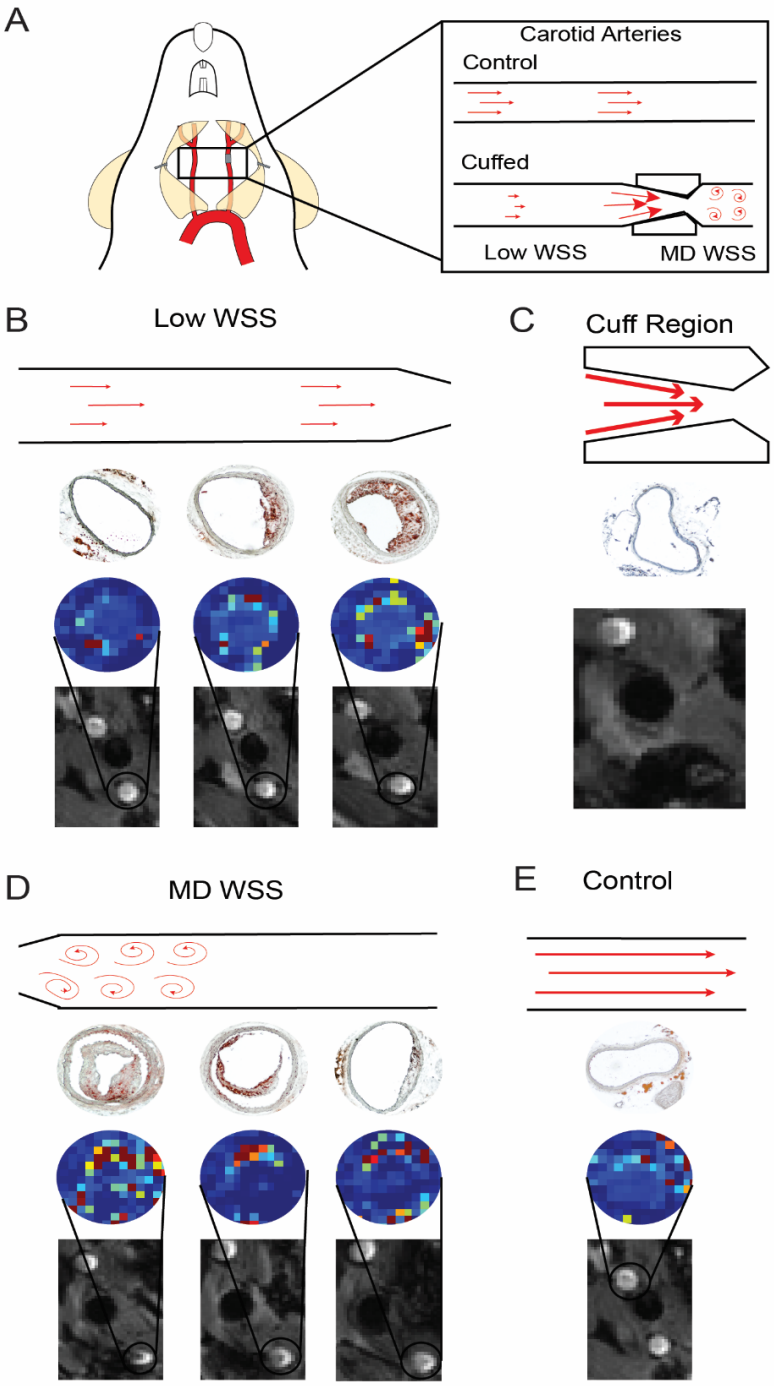

Figure 2.1. Representative sequence of co-registered MR images and histological data along the length of the instrumented carotid artery. (A) Diagram of the flow environment in the instrumented versus contralateral control carotid arteries. The cuff creates three distinct hemodynamic conditions, low WSS upstream of the cuff, high WSS within the cuff, and multidirectional (MD) WSS downstream of the cuff [39]. (B-D) Longitudinal sequence of DCE-MR images and K^{trans} maps co-registered to histology sections stained with oil red O to identify lipid from the (B) low WSS, (C) cuff, and (D) multidirectional WSS regions in the instrumented artery of a representative mouse at 9 weeks after cuff placement. (E) Data from the contralateral control artery. Note, the cuff prevents reliable acquisition of K^{trans} maps, so they are not shown in this region.

Sections stained for oil red O, picrosirius red, and Ki67 were binarized with a threshold in ImageJ to quantify the presence of positive staining within the plaque. The fluorescent images of α-SMA were converted to greyscale to quantify stain intensity. Quantification of all stains was done using a custom MATLAB program that summed the binarized (0 or 1) or greyscale (0 to 255) pixel values and normalized by the total number of pixels in the region of interest within the histological section (grey scale pixel values were additionally normalized by the maximum pixel value of 255). This program was also used to manually segment the arterial layers (lumen, internal elastic lamina (IEL), and external elastic lamina (EEL)) of each histological section (for fluorescence images, a phase image was taken with each that was used for segmentation). Once manually segmented, the program automatically identified the plaque based on deviations between the lumen and internal elastic lamina contours (these contours overlap in a non-diseased vessel section). The "cap region" was also automatically identified as the first 13.3 μm of thickness from the plaque-lumen interface, which scales to ~150 μm in a human carotid artery—a typical thickness for the cap of a fibrous cap atheroma [74]. The program quantified stain area in the plaque, plaque cap, and plaque body minus the cap region (the phase images associated with the α-SMA stain of each section were used for quantification of plaque area and burden). Finally, the program also quantified the mean distribution of collagen and α-SMA within the plaque of each section from the IEL to the lumen.

2.3.6 Statistics

To evaluate differences in NP accumulation between the different WSS regions, K^{trans} was averaged over the three DCE-MRI slices nearest the cuff in each of the two

regions of the instrumented artery where atherosclerosis develops, upstream (low WSS) and downstream (multidirectional WSS), from each mouse at 5 and 9 weeks after cuff placement. The contralateral control arteries from these mice were similarly evaluated, except K^{trans} was averaged over the entire central portion of the artery. To evaluate differences in plaque constituents and size between the different WSS regions and time points, each histological readout was averaged over all viable sections within the plaque of each instrumented vessel segment of each mouse. Group comparisons were performed using a one-way ANOVA. Pairwise comparisons, including those performed post hoc of the ANOVA, were done using a two-sample, two-tailed *t*-test. Comparisons were chosen a priori. A step-down Bonferonni-Holm correction method was used to control for type-I errors associated with multiple comparisons. Assumptions on normality were met based on a Shapiro-Wilk test and evaluation of histograms.

To evaluate the relationship between K^{trans} and plaque area, lipid, collagen, and smooth muscle, respectively, one to three co-registered histology-MRI pairs were obtained in each of the two WSS regions, low and multidirectional (all mice are represented in this analysis for each vessel segment, but, in vessel segments of some mice, missing or damaged histology sections allowed only one pairing to be included in the analysis). Each histological stain was averaged over all sections associated with the co-registered MRI slice (typically, four histology sections per slice) and plotted as a function of K^{trans}. A Spearman's rank correlation coefficient (ρ) was calculated for each data set and a linear regression was performed to visualize the trend. A Bonferonni correction method was used with these data to account for multiple comparisons.

All statistical tests were performed in MATLAB. Quantities are reported as mean ± standard deviation (SD). Corrections for multiple comparisons were implemented as an adjustment of the calculated *p*-value by the ratio of 0.05 to the adjusted alpha value. An adjusted *p*-value of less than 0.05 was considered statistically significant, which is indicated as $*p<0.05$, $**p<0.01$, and $***p<0.001$.

2.4 Results

2.4.1 Validation of NP structure and properties

Gd-based small molecule contrast agents (CAs) are commonly used in clinical settings to evaluate vascular permeability with DCE-MRI [64]. Concerns over toxicity and mediocre contrast enhancement have inspired the development of paramagnetic NP-based CAs often utilizing iron oxide or lanthanide series ions, like Gd [75, 76]. However, for these NPs to be useful in DCE-MRI, they must provide sufficient T_1 contrast enhancing properties. The FA coating, which was verified by FT-IR, functions as a surface coating [77] and serves to ensure strong T_1-enhancement, target engagement, and stability in blood. Surface FA preferentially targets folate receptors present on mononuclear phagocytes [28], increasing NP concentration at sites of inflammation by translocation [28, 78]. Surface FA also increases colloidal stability of FA-Gd, drawing H_2O nearer to the core by increasing hydrophilicity and further increasing T_1 effects [79, 80].

FA-Gd NP dimensions were assessed using high-resolution transmission electron microscopy (HRTEM), which demonstrated a mean core diameter of 4.5 nm (Figure 2.2A). Hydrodynamic size was determined as 12.9±0.4 nm by dynamic light scattering (DLS). FT-IR was performed to confirm the presence of FA on the surface of FA-Gd

NPs (Figure 2.2B). Shifting of the COOH peak from the free FA spectrum indicated coating of FA on the Gd NP surface. Prior to DCE-MRI, the contrast-enhancing properties of FA-Gd were also quantified. Relaxivity characterization of FA-Gd used a saturation recovery method of T_1 measurement at 9.4 T and determined an R_1 relaxivity of 3.15 $s^{-1}mM^{-1}$ (Figure 2.2C). Zeta potential assessment of FA-Gd showed a mean value of -40.5 mV (Figure 2.2D), which increased colloidal stability and helped to prevent aggregation and adsorption of negatively-charged serum proteins [81].

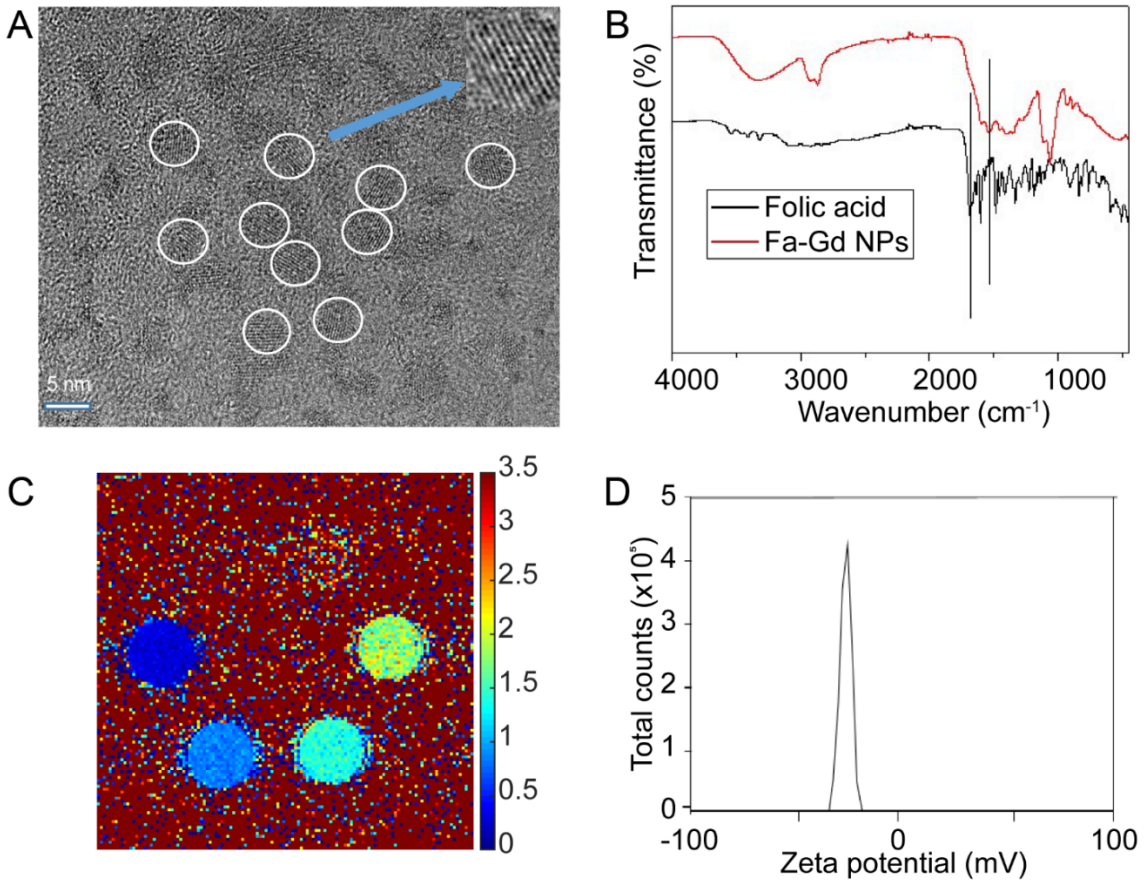

Figure 2.2. NP structure and properties. (A) HRTEM images of FA-Gd NPs, white circles indicate average diameter (4.5 nm) of the NPs. Blue arrow indicates lattice fringe of NPs. **(B)** FT-IR spectra of folic acid and FA-Gd NPs. The black spectrum corresponds to free FA, while the red spectrum corresponds to FA-Gd NPs. The COOH peak was shifted from 1680 to 1527 cm^{-1}, which confirmed the FA coating on to the Gd NPs. **(C)** R_1 map of FA-Gd NP phantoms for determination of R_1 relaxivity (3.14 $mM^{-1}s^{-1}$). **(D)** Zeta potential distribution of FA-Gd NPs, mean value of -40.5 mV.

2.4.2 NP accumulation in arterial segments exposed to low versus multidirectional WSS

DCE-MRI provides the ability to noninvasively monitor accumulation and retention kinetics of a contrast agent into a tissue of interest and is typically used to measure blood vessel permeability. We have recently extended the use of DCE-MRI to assess and compare vascular permeability kinetics of different NPs in a mouse model of traumatic brain injury [72, 73]. Here, we used this same imaging technique to determine accumulation kinetics of FA-coated, Gd-core NPs with a mean core diameter of 4.5 nm in atherosclerotic plaques. A small core size served to increase T_1 effects via increased surface area-to-volume ratio and the resultant increase in Gd-H_2O interactions [82], as well as minimize T_2 effects by decreasing the disruption of H_2O proton spin phase coherence [83]. Though the core size of FA-Gd is below 5 nm, the hydrodynamic size of 12.9 nm is sufficiently large to limit renal clearance [84]. This minimization of renal clearance, and thus increased duration of higher NP concentrations in the blood, may increase uptake into plaques, though previous investigations have shown plaque-associated macrophage internalization of NPs begins within 15 minutes of administration [85]. The relatively rapid NP clearance, compared with long-circulating formulations whose half-lives can be in the realm of hours and days [86], reduces exposure to off-target tissues. The size of FA-Gd is sufficiently small to limit sequestration to the liver by the reticuloendothelial system and increase the time spent in circulation [87].

Behavior of NPs in the blood (Table 1) was assessed by quantifying half-lives. The distribution half-life ($t_{1/2,dist}$) was 17.4±10.3 minutes while the elimination half-life ($t_{1/2,elim}$) was 46.8±14.5 minutes. As a comparison, the small molecule contrast agent Gd-DTPA has a $t_{1/2,dist}$ of approximately 4.0 minutes and a $t_{1/2,elim}$ of approximately 15.7

minutes [73]. We used DCE-MRI to generate K^{trans} maps to determine the accumulation kinetics of NPs in different regions of the instrumented artery, which contain different WSS conditions, at intermediate and fully-developed stages of plaque growth. T1-weighted images and Gd-time curves were also generated (Figures 2.3 and 2.4), though K^{trans} was the metric of comparison for NP accumulation kinetics throughout the work. In both regions, plaques developed immediately adjacent to the cuff, had a length of approximately 0.5–1.5 mm, and exhibited the highest K^{trans} in the portion of each region with maximum plaque burden (Figures 2.5).

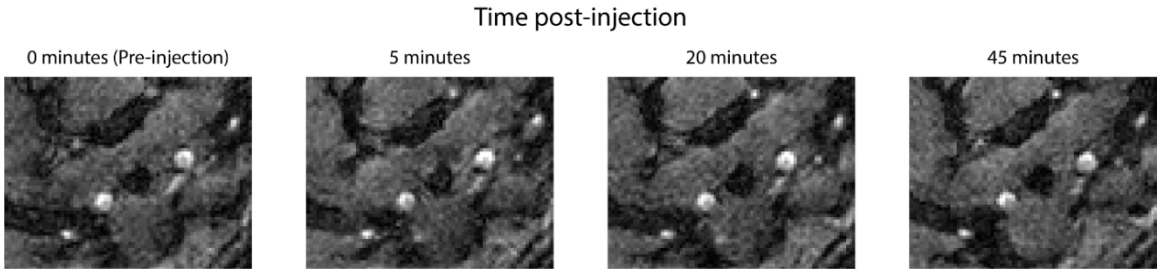

Figure 2.3. T1-weighted images of carotid arteries over time before and after injection of nanoparticles.

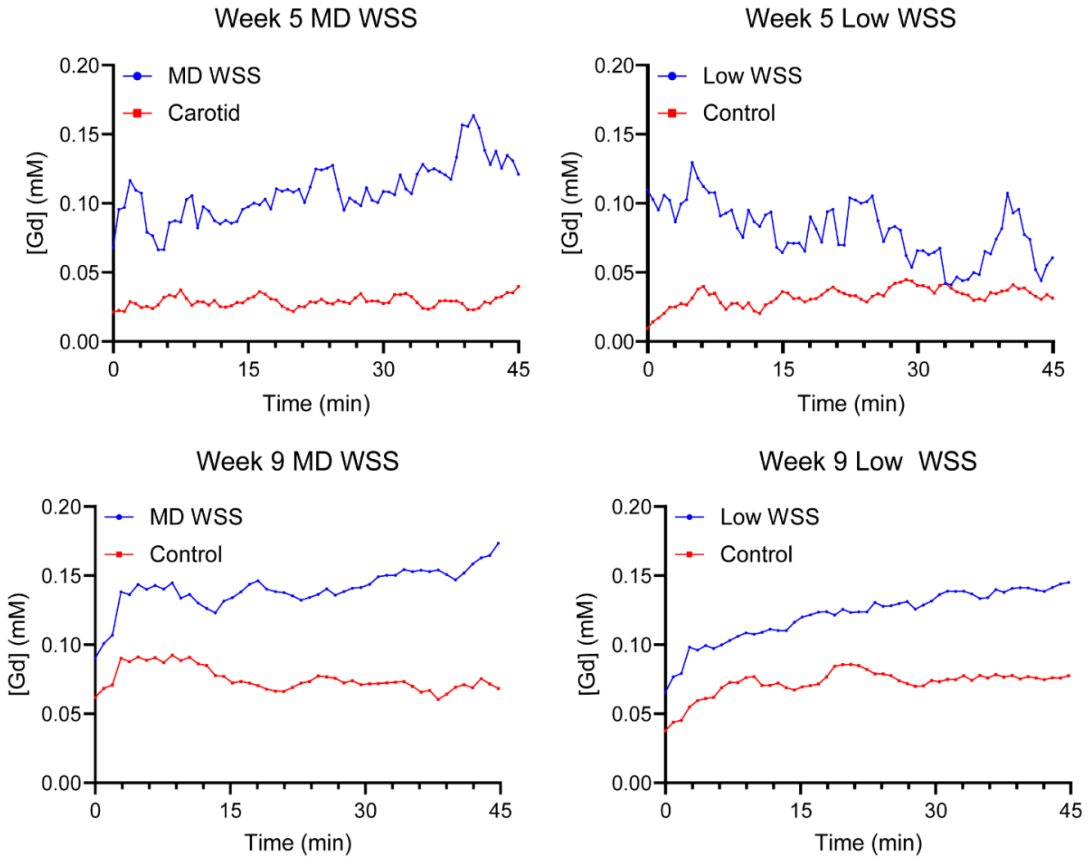

Figure 2.4. Gd-time curves in the cuffed and control arteries. Curves represent a running average of 5 time points taken from a single slice in the relevant vessel region from a single animal**.**

In the low WSS region, K^{trans} substantially increased from the least diseased portion of the instrumented artery (three MRI slices from the cuff) to the portion containing the maximum plaque burden immediately adjacent to the cuff by 1.5-fold at 5 weeks and 2.2-fold at 9 weeks after cuff placement. In the multidirectional WSS region, no differences in K^{trans} were seen, likely because this region abuts the carotid bifurcation, which contains naturally-occurring disturbed flow, so plaques were present throughout (Figure 2.5).

Table 2.1. Pharmacokinetics of FA-Gd in $ApoE^{-/-}$ mice determined by MRI.

Distribution Half-life ($t_{1/2,dist}$)	$K_{el,dist}$ [min^{-1}]	Elimination Half-life ($t_{1/2,elim}$)	$K_{el,elim}$ [min^{-1}]
17.36±10.26	0.067±0.068	46.82±14.50	0.016±0.0052

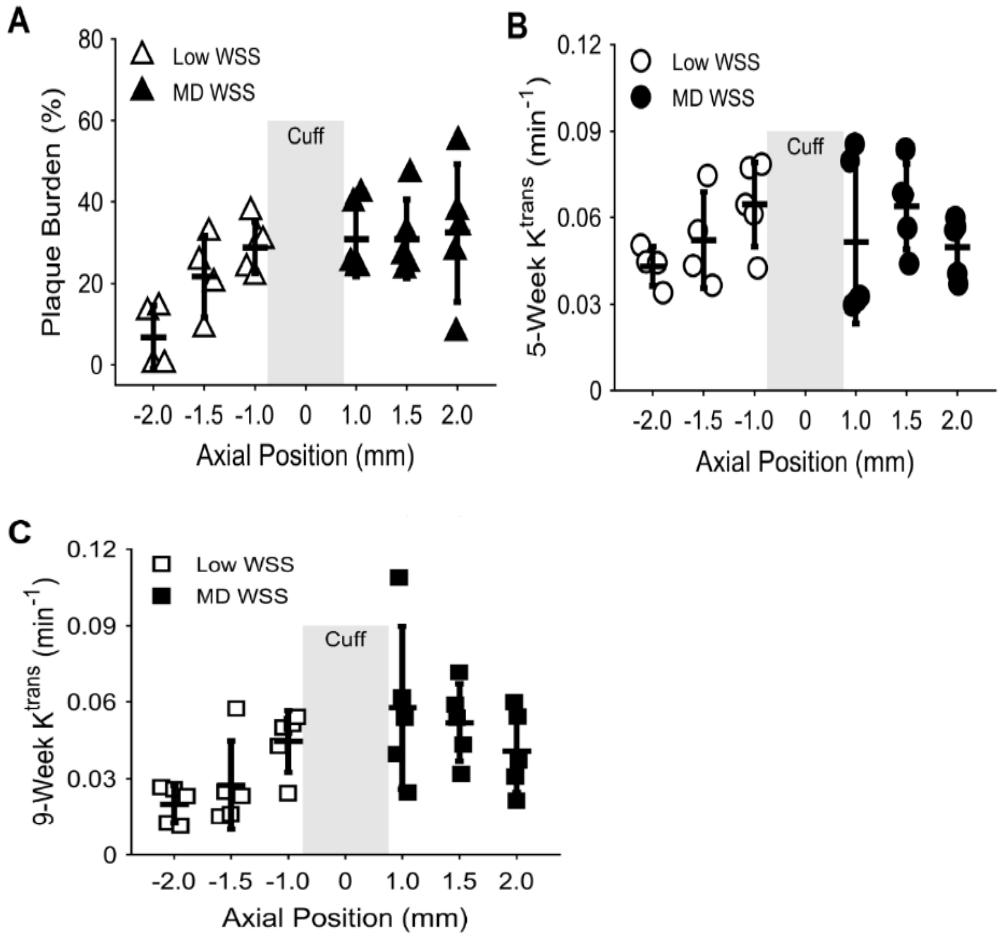

Figure 2.5. Plaque burden and NP accumulation over the length of the instrumented artery. **(A)** Plaque burden in mice injected with NPs at 9 weeks after cuff placement, **(B)** NP accumulation assessed via K^{trans} at 5 weeks after cuff placement, and **(C)** K^{trans} at 9 weeks after cuff placement as a function of position (in mm) from the center of the cuff (no plaque developed in the cuff region and there are no K^{trans} values due to the cuff creating an unreliable signal; thus, no data are presented in this region). Data points represent the mean plaque burden and K^{trans} values for each mouse injected with NPs (n=5) at each MRI slice location. Bars are mean±SD. These data were not evaluated for statistical differences between vessel regions.

We next evaluated differences in maximal K^{trans} between low and multidirectional WSS in the instrumented arteries, and normal WSS in the control arteries at 5 and 9 weeks after cuff placement. A one-way ANOVA demonstrated a highly significant difference between two or more of these groups (***p<0.001) and a two-sample, two-tailed *t*-test was used to evaluate pairwise differences (Figure 2.6A). At the intermediate stage of plaque development (5 weeks), DCE-MRI showed a significant difference in NP

accumulation between the low WSS region of the instrumented vessels compared to the contralateral control vessels, but not the multidirectional WSS region. The low WSS region had a mean K^{trans} value across all mice of 0.055±0.0047 min^{-1} versus 0.038±0.0053 min^{-1} in the control (a 1.45-fold increase; $^{**}p$=0.005) and the multidirectional WSS region had a mean K^{trans} value of 0.055±0.016 min^{-1} versus 0.038±0.0053 min^{-1} in the control (a 1.45-fold increase; p=0.22). At the fully developed stage of plaque growth (9 weeks), the K^{trans} difference between instrumented and control arteries was significant in the multidirectional WSS region, but not in the low WSS region. The low WSS region had a mean K^{trans} value of 0.031±0.0067 min^{-1} versus 0.025±0.0047 min^{-1} in the control (p=0.38), while the multidirectional WSS region had a mean K^{trans} value of 0.050±0.011 min^{-1} versus 0.025±0.0047 min^{-1} in the control (a 2.00-fold increase; $^{**}p$=0.007). The low WSS region was also found to be statistically lower at 9 compared to 5 weeks ($^{**}p$=0.0012), whereas there was no difference between time points in the multidirectional WSS region (p=1). Direct comparisons of mean K^{trans} values in the low versus multidirectional WSS regions also demonstrated a significant difference at 9 weeks (1.64-fold; $^{*}p$=0.043), but not 5 weeks (p=1).

We also assessed whether the control carotid arteries in $ApoE^{-/-}$ mice exhibited a higher K^{trans} compared to the carotid arteries of C57BL/6 control mice (e.g., due to the presence of hypercholesterolemia) and found no differences at either time point (Figure 2.6 B&C). C57BL/6 carotid arteries showed a mean K^{trans} value of 0.030±0.0074 min^{-1} compared with 0.038±0.0053 min^{-1} and 0.025±0.0047 min^{-1} in the $ApoE^{-/-}$ control carotid arteries at 5 (p=0.18) and 9 (p=0.25) weeks, respectively.

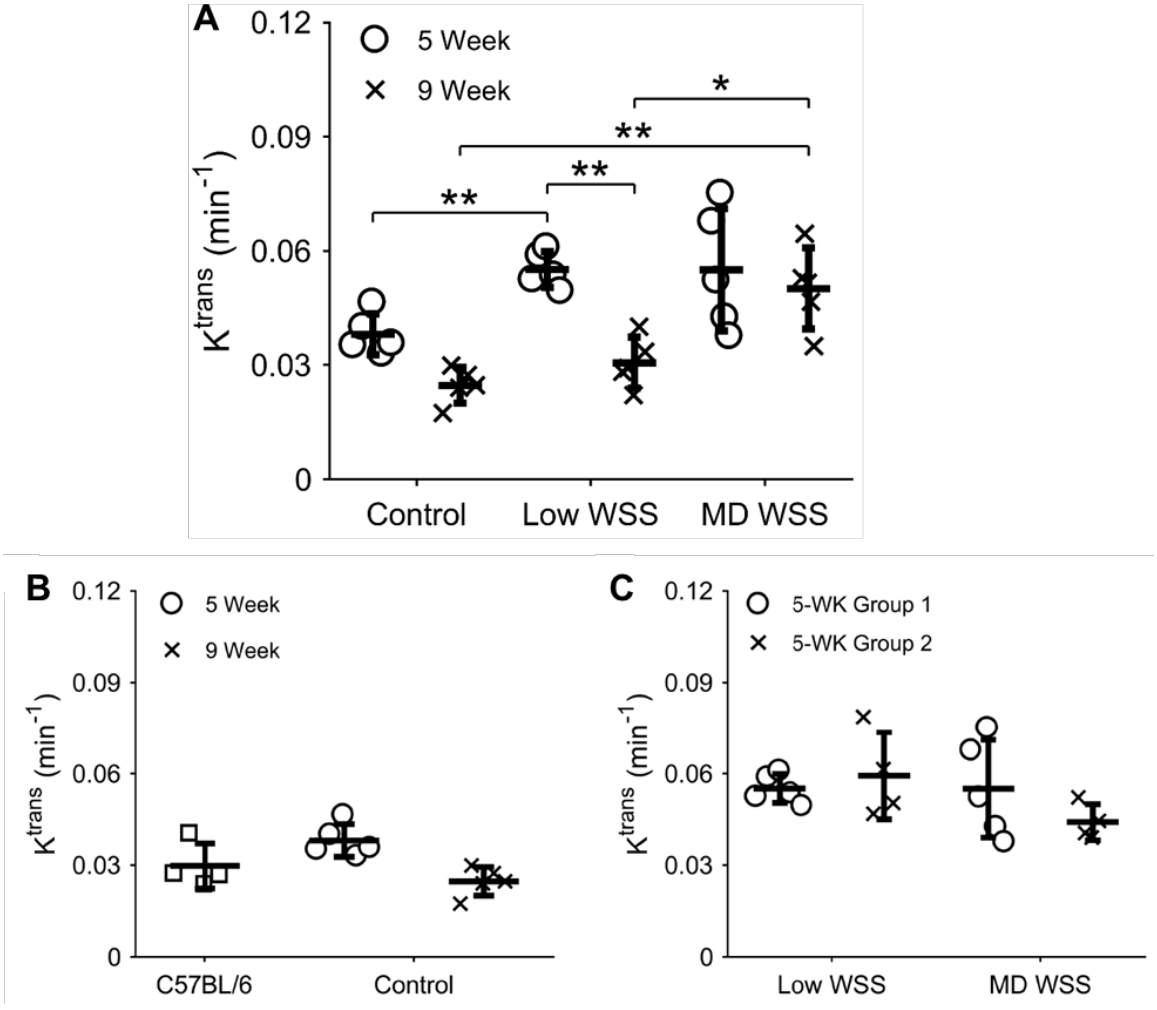

Figure 2.6. NP accumulation assessed via K^{trans} in disturbed and normal WSS conditions. (A) K^{trans} in the low and multidirectional (MD) WSS regions of the instrumented carotid arteries and contralateral control carotid arteries at 5 and 9 weeks after cuff placement. **(B)** No statistical differences were seen in Ktrans from C57BL/6 mice (four vessels from n=2 mice) versus control arteries from ApoE mice (n=5 mice) at 5 and 9 weeks. **(C)** Four addition mice used for histological evaluation of plaque features at 5 weeks after cuff placement were also injected with NPs immediately prior to culling. No statistical differences in K^{trans} were seen in this group of mice (Group 2) versus the five mice injected with NPs at 5 and 9 weeks after cuff placement (Group 1). Each data point represents the mean K^{trans} from the three DCE-MRI slices closest to the cuff within each WSS region of the instrumented artery and the mean K^{trans} from the central portion of the control artery for each mouse that was injected with NPs (n=5). Bars are mean±SD. *P<0.05 is considered statistically significant.

2.4.3 Differential NP accumulation in plaques is influenced by plaque phenotype

To better understand our finding of changes in K^{trans} from 5 to 9 weeks in the low WSS region, we evaluated changes in the constituents and size of plaques in both regions

of the instrumented arteries. In plaques induced by low WSS, α-SMA significantly decreased 0.46-fold (*p=0.023) and plaque burden significantly increased 1.60-fold (*p=0.048) from 5 to 9 weeks after cuff placement (Figure 2.7), while lipid exhibited a non-significant increase of 1.59-fold (p=0.13) (Figure 2.8). Collagen was unchanged in the low WSS between 5- and 9-week groups (Figure 2.9). The distribution of α-SMA also changed from nearly uniform at 5 weeks to more localized to the plaque-lumen interface at 9 weeks (Figure 2.7D). Although plaques induced by multidirectional WSS exhibited mostly similar trends, none of the differences in plaque constituents or size reached statistical significance (Figure 2.10).

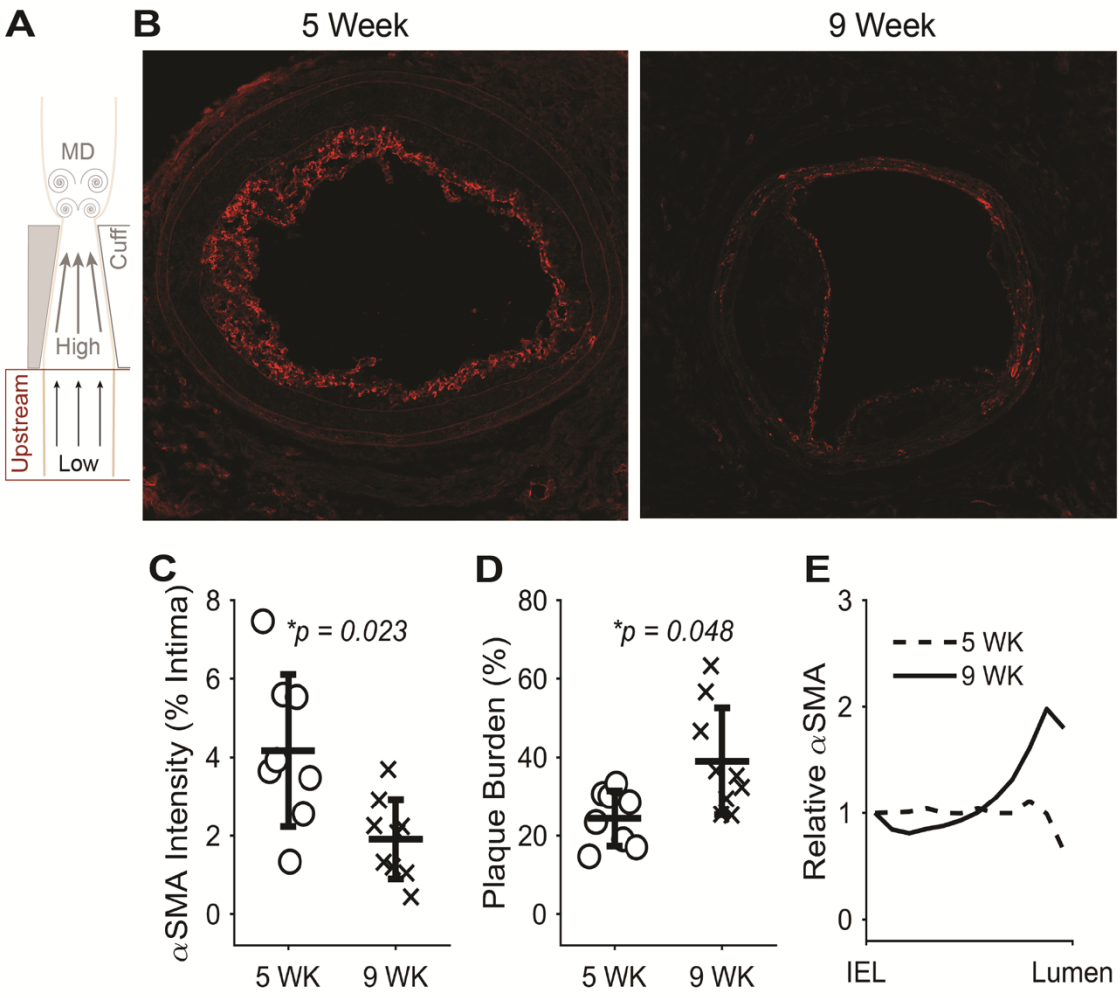

Figure 2.7. (A) Diagram of the instrumented carotid artery highlighting the focus of this figure on the low WSS (upstream) region. **(B)** Representative histology sections stained for alpha-smooth muscle actin (α-SMA), **(C)** plot of mean α-SMA intensity normalized by intima area at 5 (n=8) and 9 (n=10) weeks, and **(D)** plot of mean α-SMA intensity distribution from the internal elastic lamina (IEL) to the lumen normalized by the value at the IEL at 5 and 9 weeks. **(E)** Plot of mean plaque burden at 5 and 9 weeks. In the scatter plots, each data point represents the average of all viable histological sections for the given stain in the plaque region of the upstream vessel segment of one mouse. Bars are mean±SD. *P<0.05 is considered statistically significant.

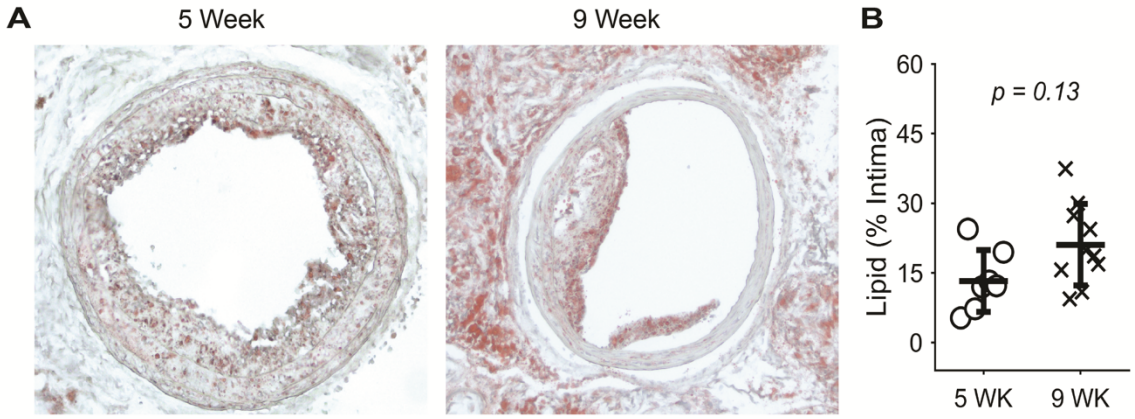

Figure 2.8. (A) Representative histology sections stained with oil red O to detect lipid and **(B)** plot of mean lipid area normalized by intima area across all mice at 5 (n=7 mice) and 9 (n=10) weeks after cuff placement.

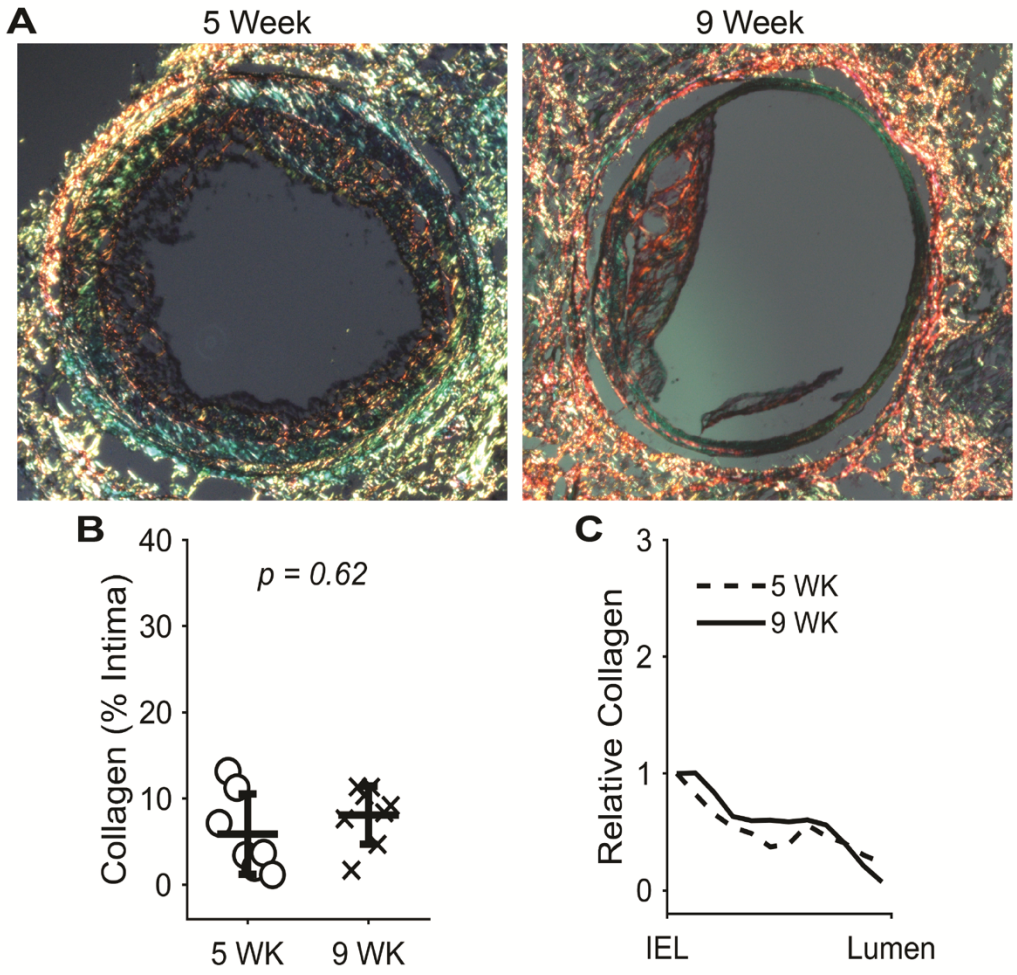

Figure 2.9. (A) Representative histology sections stained with picrosirius red to detect collagen, **(B)** plot of mean collagen area normalized by intima area at 5 (n=7) and 9 (n=8) weeks, and **(C)** plot of mean collagen distribution from the internal elastic lamina (IEL) to the lumen normalized by the value at the IEL at 5 and 9 weeks.

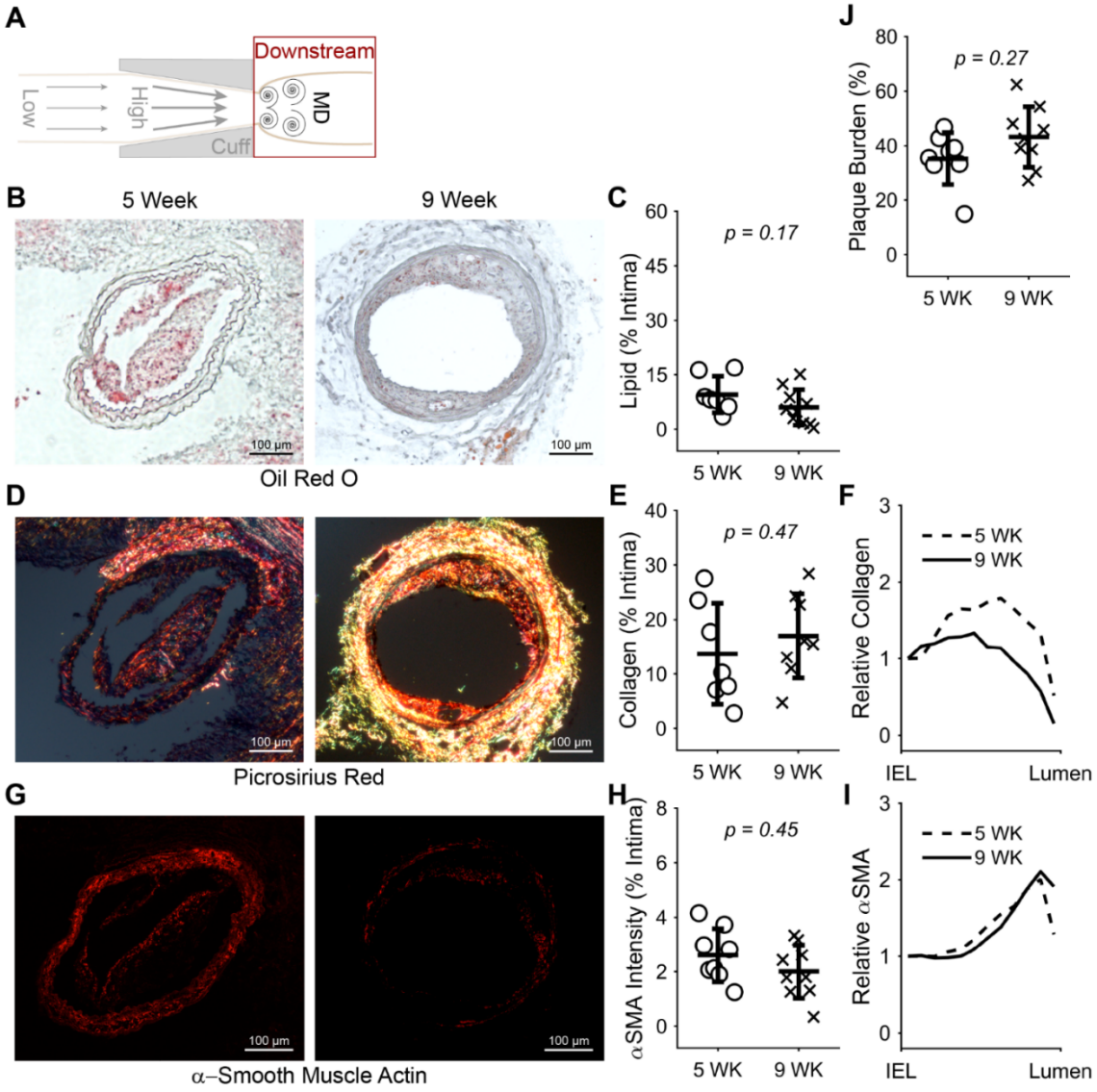

Figure 2.10. Constituents and size of plaques induced by multidirectional WSS at 5 versus 9 weeks. **(A)** Diagram of the instrumented carotid artery highlighting the focus of this figure on the multidirectional WSS (downstream) region. **(B)** Representative histology sections stained with oil red O to detect lipid and **(C)** plot of mean lipid area normalized by intima area across all mice at 5 (n=7 mice) and 9 (n=10) weeks after cuff placement. **(D)** Representative histology sections stained with picrosirius red to detect collagen, **(E)** plot of mean collagen area normalized by intima area at 5 (n=7) and 9 (n=8) weeks, and **(F)** plot of mean collagen distribution from the internal elastic lamina (IEL) to the lumen normalized by the value at the IEL at 5 and 9 weeks. **(G)** Representative histology sections stained for alpha-smooth muscle actin (α-SMA), **(H)** plot of mean α-SMA intensity normalized by intima area at 5 (n=8) and 9 (n=10) weeks, and **(I)** plot of mean α-SMA intensity distribution from the internal elastic lamina (IEL) to the lumen normalized by the value at the IEL at 5 and 9 weeks. **(J)** Plot of mean plaque burden at 5 and 9 weeks. In the scatter plots, each data point represents the average of all viable histological sections for the given stain in the plaque region of the downstream vessel segment of one mouse. Bars are mean±SD. *P<0.05 is considered statistically significant.

To evaluate how nanoparticle accumulation may be influenced by plaque phenotype, each of the aforementioned constituents and plaque area were correlated to K^{trans} from co-registered DCE-MRI slices at 9 weeks after cuff placement. In plaques induced by low WSS (Figure 2.11A-B), the fluorescence intensity of α-SMA exhibited a significant inverse correlation with K^{trans} of -0.87 (*p=0.014) (Figure 2.11C). This inverse correlation was found to stem from the plaque cap (considered to cover the first 13.3 μm of plaque thickness from the lumen), where separate evaluation revealed an even stronger correlation of -0.92 (**p=0.0039) (Figure 2.11D). On the other hand, the plaque body (whole plaque minus the cap) in this region showed a non-significant correlation of -0.72 (p=0.11) (Figure 2.11E). In contrast to low WSS, α-SMA in plaques induced by multidirectional WSS exhibited no correlation with K^{trans} (Figure 2.12A-E).

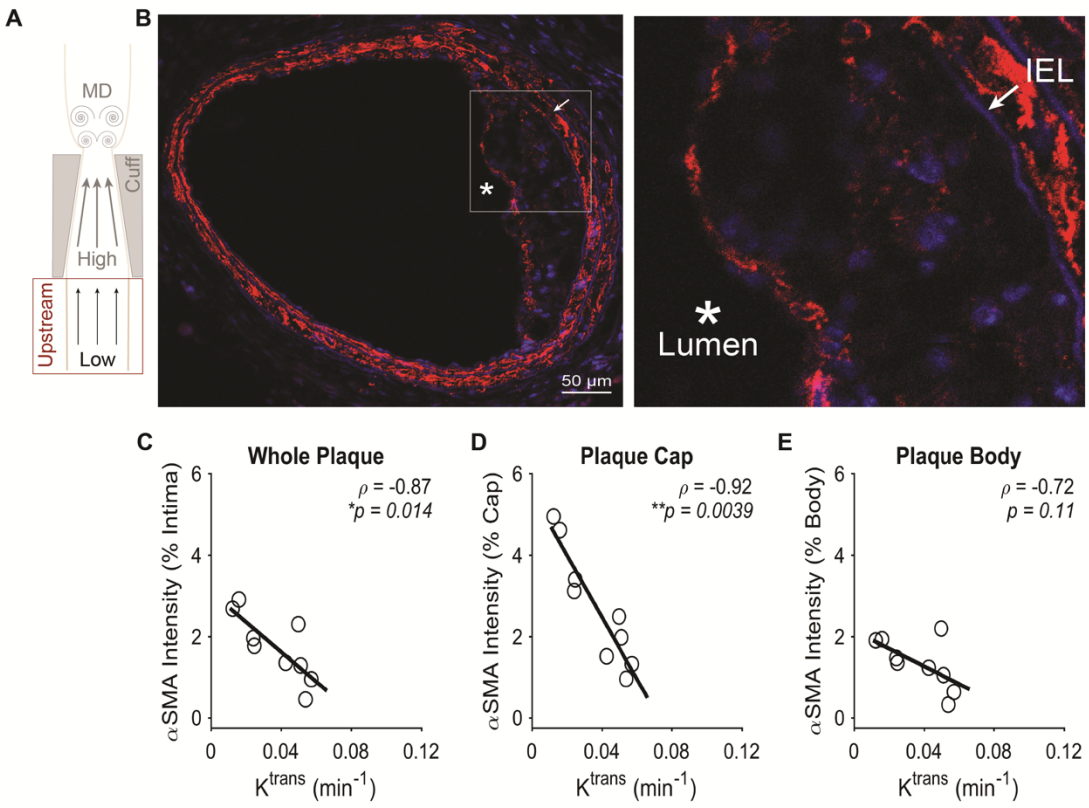

Figure 2.11. Correlation between α-SMA and NP accumulation assessed via K^{trans} at 9 weeks after cuff placement. **(A)** Diagram of the instrumented carotid artery highlighting the focus of this part of the figure on the low WSS (upstream) region. **(B)** A representative histology section and higher magnification insert of the plaque region, where the lumen and internal elastic lamina (IEL) are identified. **(C-E)** The correlation between α-SMA and K^{trans} in different regions of the plaques induced by low WSS, including the **(C)** entire plaque, **(D)** plaque cap (13.3 μm), and **(E)** plaque body minus the cap. Each data point of each plot represents the mean α-SMA fluorescence intensity normalized by intimal area across all histological sections associated with a DCE-MRI slice, from which K^{trans} was obtained (in mice with viable histological sections associated with more than one DCE-MRI slice, more than one pairing was used; all mice injected with NPs (n=5) are represented in all plots). The black line in each plot represents a linear regression of the data to visualize the trend. Spearman's correlation coefficient, ρ and associated p-value are also given. *P<0.05 is considered statistically significant.

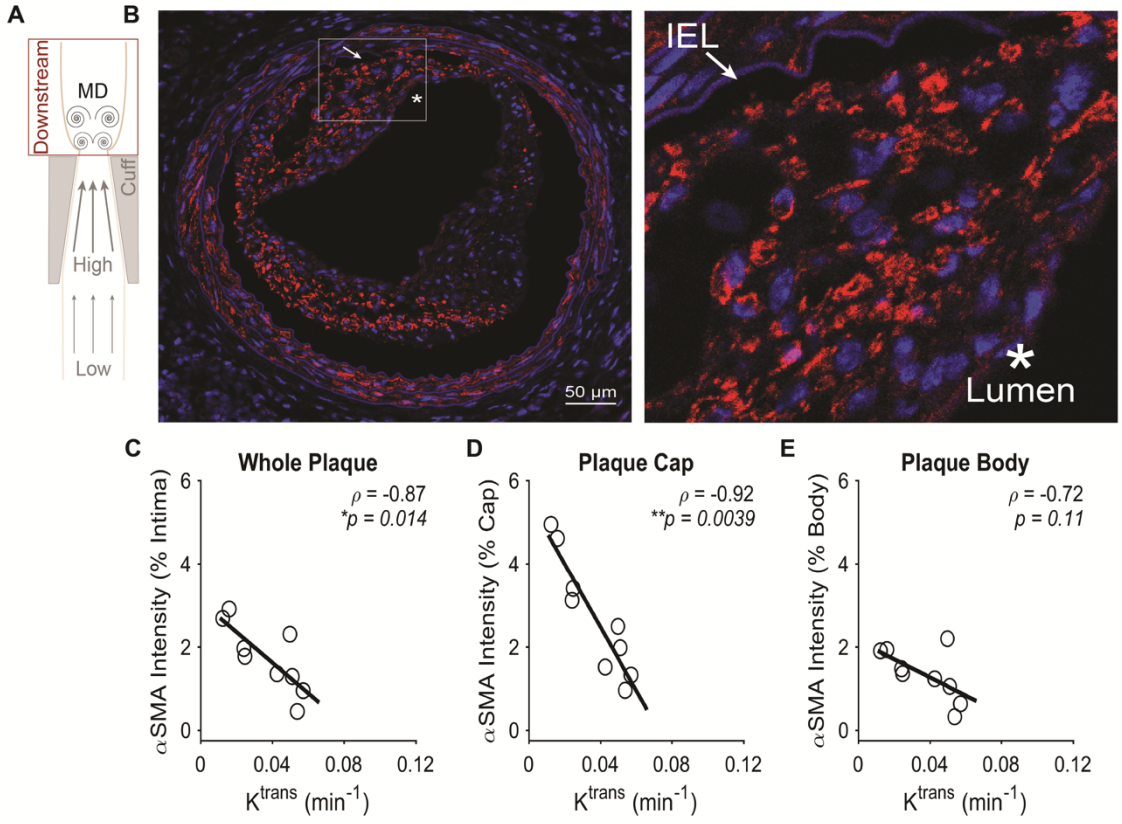

Figure 2.12. (A) Diagram of the instrumented carotid artery highlighting the focus of this part of the figure on the multidirectional WSS (downstream) region. **(B)** A representative histology section and higher magnification insert of the plaque region. **(C-E)** The correlation between α-SMA and K^{trans} in different regions of the plaques induced by multidirectional WSS, including the **(C)** entire plaque, **(E)** plaque cap (13.3 μm), and **(E)** plaque body minus the cap. Each data point of each plot represents the mean α-SMA fluorescence intensity normalized by intimal area across all histological sections associated with a DCE-MRI slice, from which K^{trans} was obtained (in mice with viable histological sections associated with more than one DCE-MRI slice, more than one pairing was used; all mice injected with NPs (n=5) are represented in all plots). The black line in each plot represents a linear regression of the data to visualize the trend. Spearman's correlation coefficient, ρ, and associated p-value are also given. *P<0.05 is considered statistically significant.

Collagen in plaques induced by low WSS exhibited a complementary trend to α-SMA, but with lower absolute correlation coefficients that did not achieve statistical significance. The correlation between K^{trans} and collagen was 0.70 (p=0.13) in the whole plaque and 0.73 (p=0.093) in the plaque body but exhibited a much lower value in the plaque cap of 0.10 (p=1) (Figure 2.13A-E). Collagen in plaques induced by multidirectional WSS showed similar results to α-SMA, where none of the plaque

components demonstrated marked or significant correlation coefficient values with K^{trans} (Figure 2.14A-E).

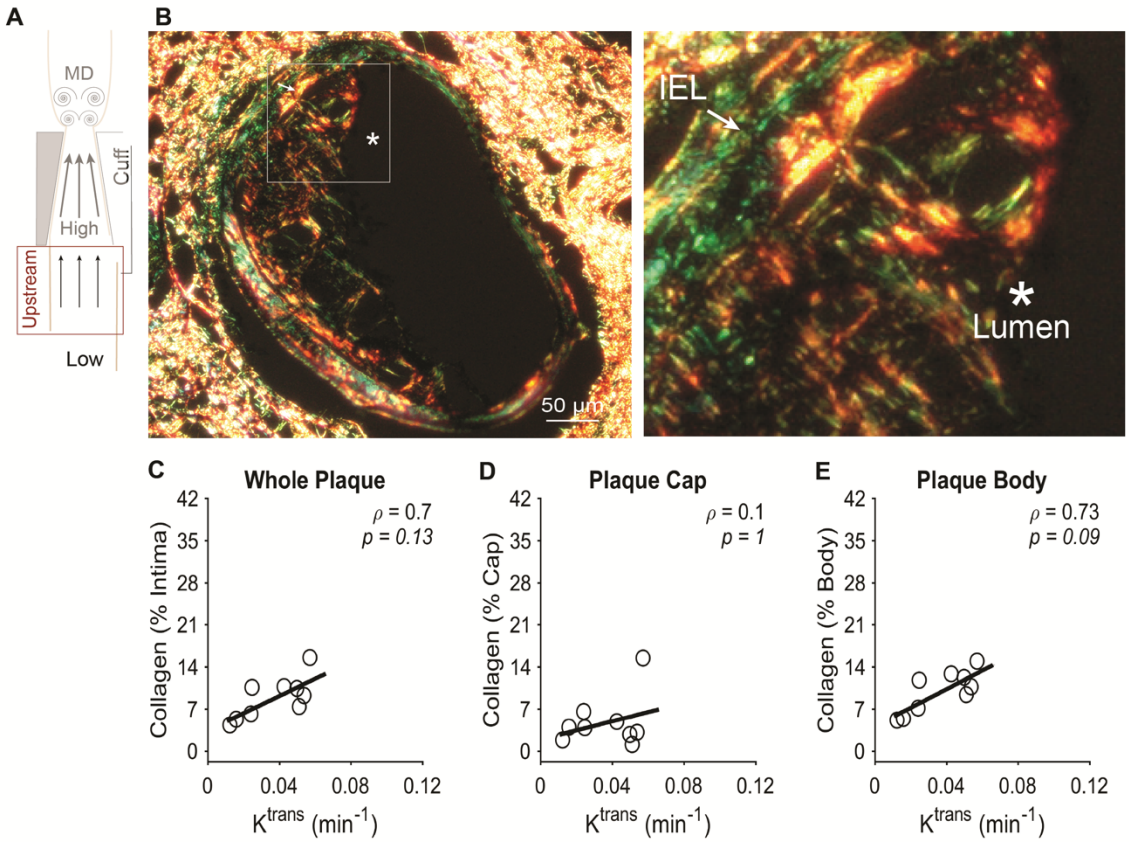

Figure 2.13. Correlation between collagen and NP accumulation assessed via K^{trans} at 9 weeks after cuff placement. **(A)** Diagram of the instrumented carotid artery highlighting the focus of this part of the figure on the low WSS (upstream) region. **(B)** A representative histology section and higher magnification insert of the plaque region, where the lumen and internal elastic lamina (IEL) are identified. **(C-E)** The correlation between collagen and K^{trans} in different regions of the plaques induced by low WSS, including the **(C)** entire plaque, **(D)** plaque cap (13.3 μm), and **(E)** plaque body minus the cap. Each data point of each plot represents the mean collagen area normalized by intimal area across all histological sections associated with a DCE-MRI slice, from which K^{trans} was obtained (in mice with viable histological sections associated with more than one DCE-MRI slice, more than one pairing was used; all mice injected with NPs (n=5) are represented in all plots). The black line in each plot represents a linear regression of the data to visualize the trend. Spearman's correlation coefficient, ρ, and associated p-value are also given. *P<0.05 is considered statistically significant.

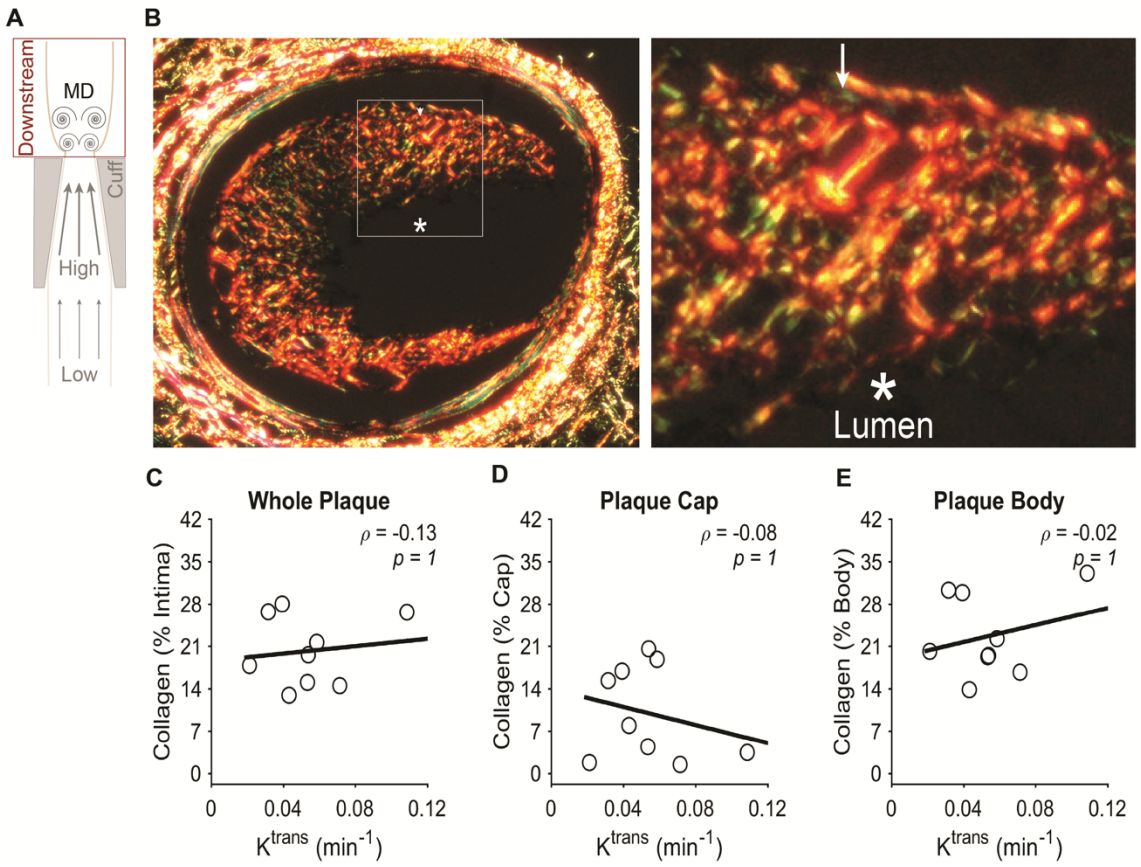

Figure 2.14. Correlation between collagen and NP accumulation assessed via K^{trans} at 9 weeks after cuff placement. **(A)** Diagram of the instrumented carotid artery highlighting the focus of this part of the figure on the multidirectional WSS (downstream) region. **(B)** A representative histology section and higher magnification insert of the plaque region. **(C-E)** The correlation between collagen and K^{trans} in different regions of the plaques induced by multidirectional WSS, including the **(C)** entire plaque, **(D)** plaque cap (13.3 μm), and **(E)** plaque body minus the cap. Each data point of each plot represents the mean collagen area normalized by intimal area across all histological sections associated with a DCE-MRI slice, from which K^{trans} was obtained (in mice with viable histological sections associated with more than one DCE-MRI slice, more than one pairing was used; all mice injected with NPs (n=5) are represented in all plots). The black line in each plot represents a linear regression of the data to visualize the trend. Spearman's correlation coefficient, ρ, and associated p-value are also given. *P<0.05 is considered statistically significant.

Lipid showed no correlation with K^{trans} in either segment of the instrumented vessel (Figure 2.15). In addition to these plaque constituents, we also evaluated the correlation between plaque area and K^{trans}. Plaque area exhibited a strong positive correlation with K^{trans} in plaques induced by low WSS (Figure 2.16A-D), particularly in the whole plaque (rho=0.95, $^{**}p$=0.0034) and body (rho=0.95, $^{**}p$=0.0034), but not the cap (rho=0.71,

p=0.17). There was no correlation between plaque area and K^{trans} in plaques induced by multidirectional WSS (Figure 2.16 E-H).

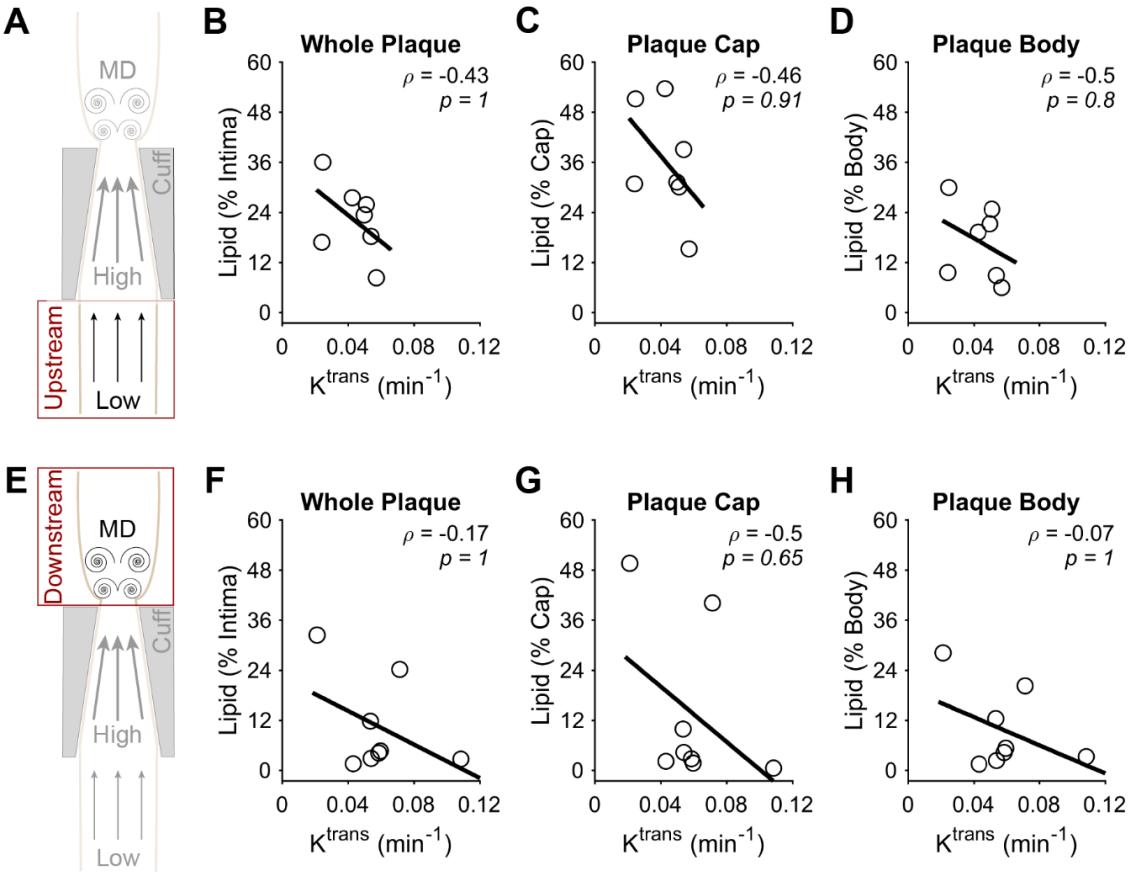

Figure 2.15. **Correlation between lipid and NP accumulation assessed via K^{trans} at 9 weeks after cuff placement**. **(A)** Diagram of the instrumented carotid artery highlighting the focus of this part of the figure on the low WSS (upstream) region. **(B-D)** The correlation between lipid and K^{trans} in different regions of plaques induced by low WSS, including the **(B)** entire plaque, **(C)** plaque cap (13.3 μm), and **(D)** plaque body minus the cap. **(E)** Diagram of the instrumented carotid artery highlighting the focus of this part of the figure on the multidirectional WSS (downstream) region. **(F-H)** The correlation between lipid and K^{trans} in different regions of plaques induced by multidirectional WSS, including the **(F)** entire plaque, **(G)** plaque cap (13.3 μm), and **(H)** plaque body minus the cap. Each data point of each plot represents the mean lipid (normalized by intima area) across all histological sections associated with a DCE-MRI slice, from which K^{trans} was obtained (in mice with viable histological sections associated with more than one DCE-MRI slice, more than one pairing was used; all mice injected with NPs (n=5) are represented in all plots). The black line in each plot represents a linear regression of the data to visualize the trend. Spearman's correlation coefficient, ρ, and associated p-value are also given. *P<0.05 is considered statistically significant.

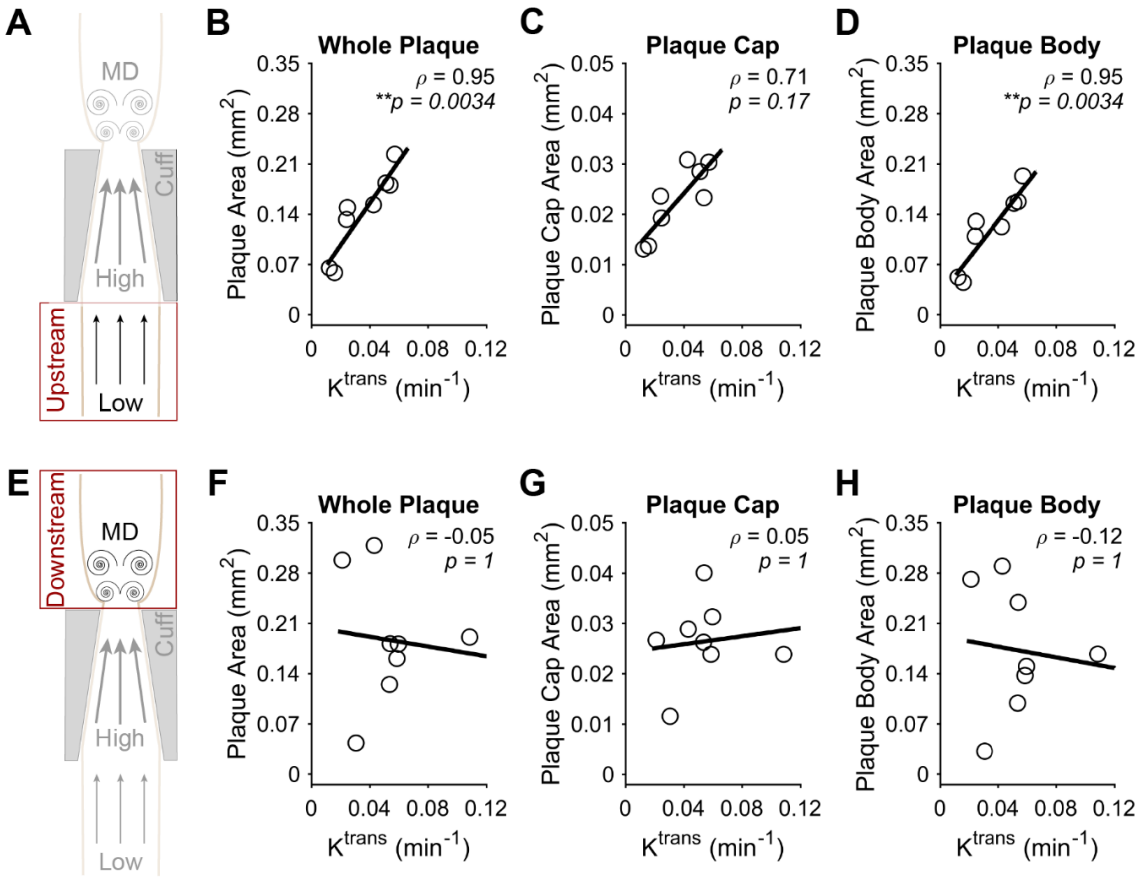

Figure 2.16. Correlation between plaque area and NP accumulation assessed via K^{trans} at 9 weeks after cuff placement. **(A)** Diagram of the instrumented carotid artery highlighting the focus of this part of the figure on the low WSS (upstream) region. **(B-D)** The correlation between plaque area and K^{trans} in different regions of the plaques induced by low WSS, including the **(B)** entire plaque, **(C)** plaque cap (13.3 μm), and **(D)** plaque body minus the cap. **(E)** Diagram of the instrumented carotid artery highlighting the focus of this part of the figure on the multidirectional WSS (downstream) region. **(F-H)** The correlation between plaque area and K^{trans} in different regions of the plaques induced by multidirectional WSS, including the **(F)** entire plaque, **(G)** plaque cap (13.3 μm), and **(H)** plaque body minus the cap. Each data point of each plot represents the mean plaque area across all histological sections associated with a DCE-MRI slice, from which K^{trans} was obtained (in mice with viable histological sections associated with more than one DCE-MRI slice, more than one pairing was used; all mice injected with NPs (n=5) are represented in all plots). The black line in each plot represents a linear regression of the data to visualize the trend. Spearman's correlation coefficient, ρ and associated p-value are also given. *P<0.05 is considered statistically significant.

Since there were strong correlations between smooth muscle, collagen, and plaque area in plaques induced by low WSS, but not MD WSS, we also evaluated differences in these plaque characteristics between the flow conditions at 9 weeks after cuff placement. Interestingly, neither plaque burden nor α-SMA were different between these regions (Figure 2.17A-B). However, plaques induced by low WSS exhibited a statistically

significantly higher amount of lipid (3.51-fold, **p=0.0005) and lower amount of collagen (0.48-fold, *p=0.030) compared to those induced by multidirectional WSS (Figure 2.17C-D). In addition, we evaluated a marker of cell proliferation, Ki67, which was also statistically higher in plaques induced by low WSS versus multidirectional WSS (3.70-fold, *p=0.015). Separate evaluation in the plaque cap region showed an even larger difference in Ki67 between these two plaque phenotypes of 4.80-fold (*p=0.018) (Figure 2.18).

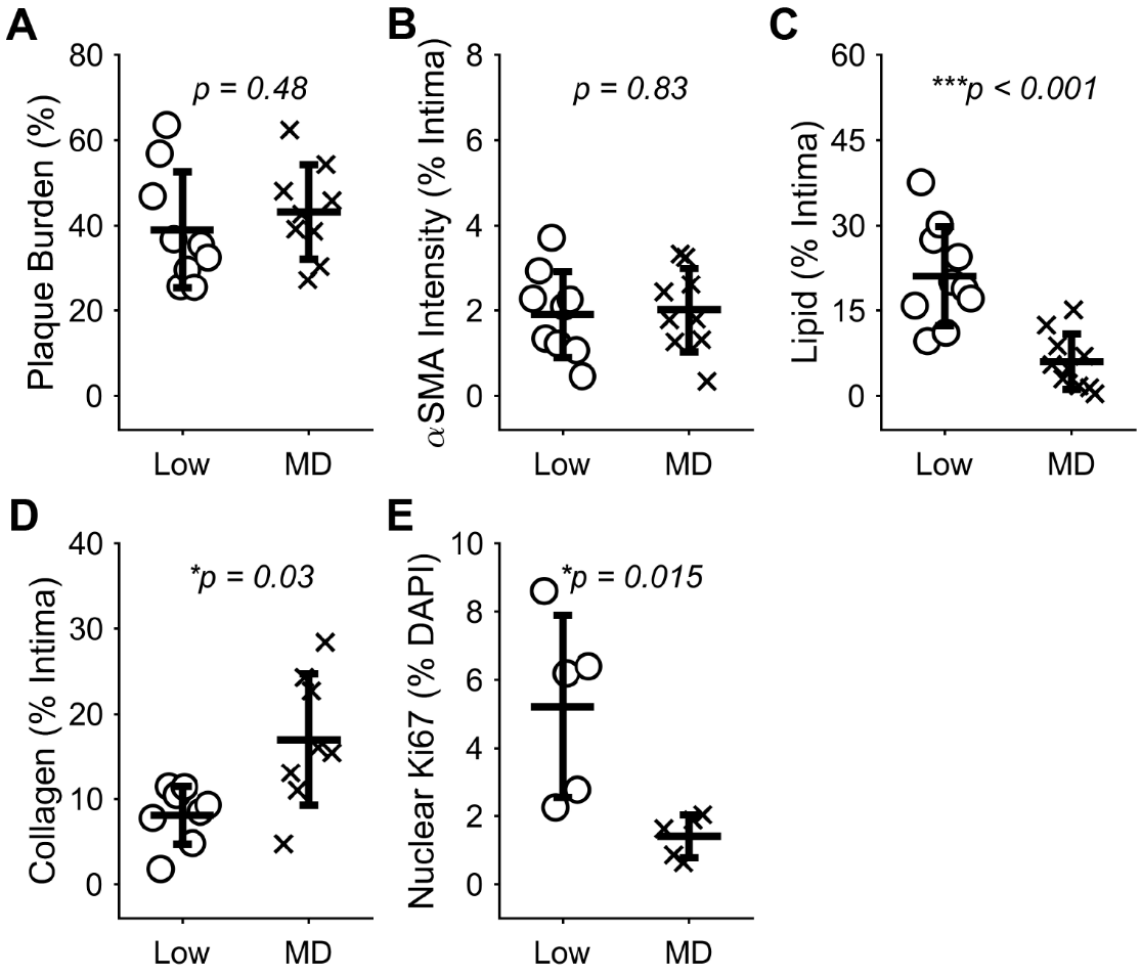

Figure 2.17. Characteristics of plaques induced by low WSS compared to multidirectional (MD) WSS. Plaque size and constituents assessed over the whole plaque, including: **(A)** Plaque burden (n=10 mice), **(B)** α-SMA intensity (n=10), (C) lipid (n=10), (D) Collagen (n=8), and **(E)** area of Ki67 in the nucleus of cells normalized by total cell nuclear (DAPI) area (n=5). Each data point of each plot represents the average of a given readout across all viable histological sections in each vessel segment of one mouse. Bars are mean±SD. *P<0.05 is considered statistically significant.

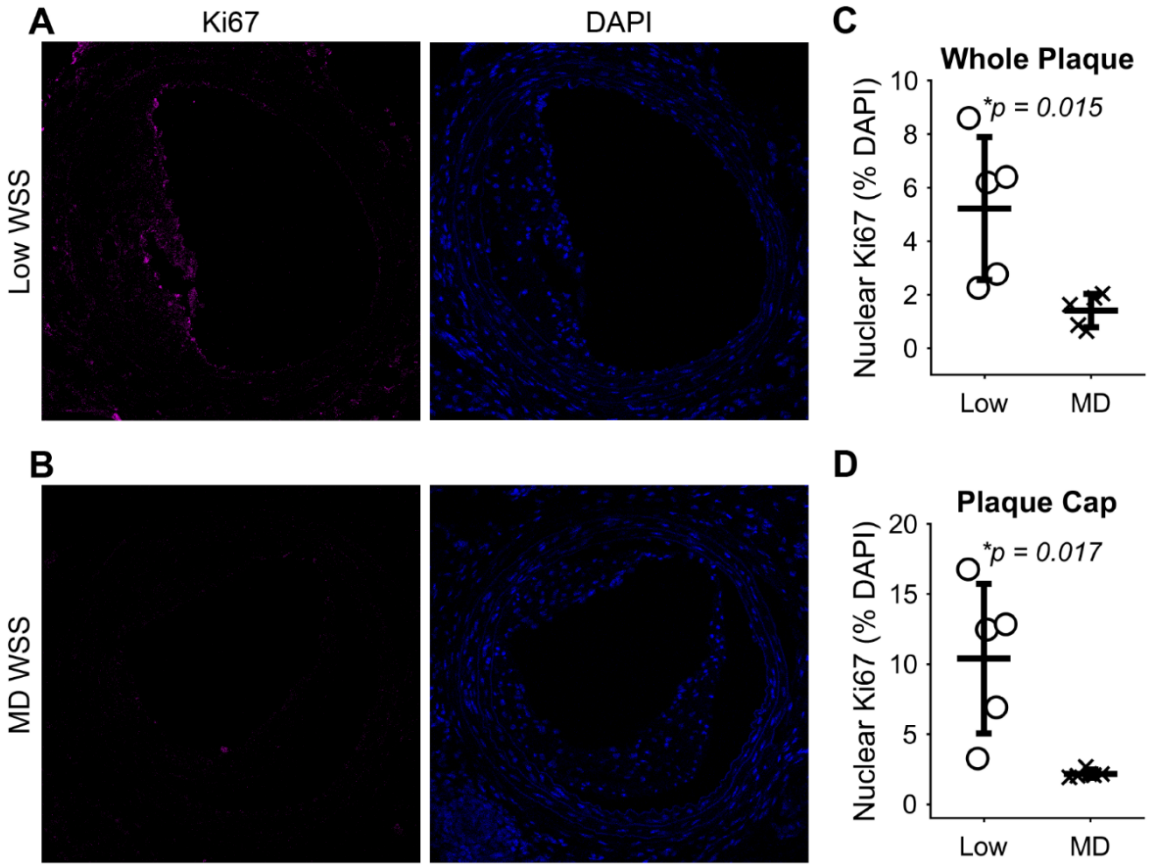

Figure 2.18. Comparison of Ki67 staining in plaques induced by low versus multidirectional WSS. Representative histology sections of Ki67 counterstained with DAPI in plaques induced by **(A)** low and **(B)** multidirectional WSS. Plots of nuclear Ki67 area as a percentage of total DAPI area in the **(C)** whole plaque and **(D)** plaque cap across all mice evaluated (n=5). Each data point of each plot represents the average nuclear Ki67 (% DAPI) across all viable histological sections in each vessel segment of one mouse. Bars are mean±SD. *P<0.05 is considered statistically significant.

2.5 Discussion

WSS in regions of disturbed blood flow promotes endothelial dysfunction and atherosclerosis, and many studies have demonstrated that specific disturbed blood flow conditions promote certain plaque phenotypes [25, 27, 28, 35]. In this study, we evaluated the influence of both the WSS condition and plaque phenotype on the accumulation of NPs within atherosclerotic arteries. At 5 weeks after cuff placement, we found that NP accumulation in the low WSS regions was statistically higher than the contralateral control arteries, which exhibit laminar flow, but there were no differences in accumulation between the two plaque phenotypes at this intermediate stage. However,

while NP accumulation was the same from 5 to 9 weeks in the multidirectional WSS region, NP accumulation was statistically lower in the low WSS region at 9 weeks compared to 5 weeks. Direct comparison of the two WSS regions at 9 weeks also demonstrated a statistically lower NP accumulation in the low WSS compared to multidirectional WSS regions. This delayed difference between the two WSS regions suggests that different disturbed blood flow conditions do not directly affect NP accumulation, at least not for the specific NPs used herein; rather, the effect is indirect in that the final plaque phenotypes induced by the two WSS regions drive differences in NP accumulation.

Following this observation, we found that the plaque constituent exhibiting the most significant (inverse) correlation with K^{trans} was α-SMA at the plaque-lumen interface (i.e., the cap) of plaques induced by low WSS (unstable plaque). Since there was no correlation between collagen and K^{trans} in the cap region of these plaques, our findings suggest that the presence of smooth muscle cells at this lumen interface was the principal determinant of NP transport. There was also no correlation between α-SMA or collagen and K^{trans} in plaques induced by multidirectional WSS. Interestingly, we found no difference in the relative amount of α-SMA between the two plaque phenotypes, although we did find that α-SMA significantly decreased and changed distribution from the IEL to the lumen in the unstable (low WSS) plaques, but not the stable (multidirectional WSS) plaques. In addition, the unstable plaques had higher lipid, lower collagen, and higher Ki67 expression compared to stable plaques, as expected and in line with previous studies that characterized the plaque phenotypes in this mouse model [25, 39, 67]. Together, these findings suggest that smooth muscle cells in the unstable plaques

are slightly more distributed towards the lumen and have a more synthetic phenotype compared to those in stable plaques, which may underlie the disruption to NP transport.

In humans, the fibrous cap (of a fibrous cap atheroma) has been described by Virmani et al. [16] as “a distinct layer of connective tissue completely covering the lipid core” that “consists purely of smooth muscle cells in a collagenous proteoglycan matrix.” In contrast, pathological intimal thickening is “characterized by the presence of smooth muscle cells interspersed within extracellular matrix towards the lumen and areas of extracellular lipid accumulation” [88], suggesting lesser organization. Our histological evaluation of the unstable and stable murine plaques herein suggests a similar organization of the smooth muscle to that seen in fibrous cap atheroma and pathological intimal thickening, respectively, in humans that leads to higher transport in more stable plaques. This fits with our observation of higher K^{trans} in stable plaques induced by multidirectional WSS compared to unstable plaques induced by low WSS. It is also supported by our observation of a positive correlation between collagen and K^{trans} in the body of plaques induced by low WSS that suggests the unstable plaques have some variability between them and those that are less advanced (e.g., more collagen) are more permeable to NPs. Plaque area was also found to positively correlate with K^{trans} in plaques induced by low WSS, but this may be simply due to the larger space for NPs to accumulate (although no correlation was found in plaques induced by multidirectional WSS). Larger overall plaque size does not necessarily correspond to a more advanced phenotype [89, 90].

Previous studies in mice have also reported lower transport in unstable versus stable plaques, despite differences in experimental procedures (e.g., NP formulations)

from the present work. One study assessed the uptake of 16 nm micelles (similar to the 13 nm NPs used in this work) based on simple signal enhancement in a similar mouse model and showed a trending decrease in unstable plaque uptake with plaque progression, while uptake in the stable plaque did not show a decrease with progression [91]. Another study showed significantly decreased NP (90 nm hyaluronan NP) accumulation in the aortic arch of $ApoE^{-/-}$ mice (where atherosclerosis naturally develops) at 12 weeks compared to 6 weeks on a Western diet [85]. They attributed this decrease to a finding of increased endothelial cell junction continuity that improved barrier function with plaque progression (which may occur due to increased flow on the upstream side of plaques causing significant lumen stenosis) and changes in plaque morphology, wherein advanced plaques demonstrated smooth muscle cell migration into the intima, as found herein. Important to these observations is that NP uptake in mouse atherosclerotic plaques takes place predominantly across disrupted macrovascular endothelium [85]. Though neovascularization into the plaque from the adventitia has been noted in human studies [92, 93], work in mice has shown limited connection between plaque interior and adventitial microvasculature [94]. Other studies in a rabbit model [95] and human patients [96] have shown that extensive neovascularization was associated with plaque progression to a vulnerable phenotype and increased permeability due to the formation of immature and leaky micro-vessels.

Our observation of differential NP uptake in unstable versus stable murine plaques at the fully developed stage, but not an intermediate stage, of growth, suggests that these NPs, together with DCE-MRI, could be used as a non-invasive diagnostic of plaque phenotype in mouse models of atherosclerosis. Such a diagnostic would benefit

studies of plaque progression, as well as those examining the efficacy of novel therapeutics in promoting plaque regression, by eliminating the need for costly and time-consuming histological evaluation of the plaque at intermediate time points. Further characterization and development of this approach could also lead to a non-invasive diagnostic for patients to better characterize plaque stage. Future work will seek to improve the efficacy of this diagnostic by using NPs targeted to the dysfunctional endothelium (e.g., VCAM-1 [65]) or plaque components (e.g., CD146 on foam cells [97]) as well as identifying how NP size affects their accumulation across various stages of plaque development. While elegant work has been conducted comparing NP size in atherosclerosis [98], it was done in the context of improving therapy by mimicking high density lipoprotein at a single stage of plaque development. Tissue fluorescence-based comparisons between uptake in the aortic arch were performed, but was not a focus of the study, so direct quantitative size-accumulation comparisons were not made; however, smaller NPs showed higher aorta-to-spleen accumulation ratios as compared to larger NPs. The reduction in accumulation in larger NPs is likely a result of the level of disruption of the macrovascular endothelium at the advanced stage of plaque development in their model ($ApoE^{-/-}$ mice fed a high-fat diet, 42% calories from fat, for 16 weeks).

2.6 Conclusion

NPs may offer an impactful strategy for the development of a novel diagnostic of atherosclerotic plaque phenotype. To accomplish this goal, there is a need for better understanding of how the blood flow environment and plaque characteristics affect NP accumulation and retention. Using a mouse model of atherosclerosis where one carotid

artery was instrumented with a constrictive cuff to induce low WSS upstream of the cuff and multidirectional WSS downstream of the cuff, we found that accumulation and retention kinetics of folic acid-coated gadolinium (FA-Gd) NPs were not directly influenced by the WSS condition, but rather, the plaque phenotype that develops in each WSS condition. In particular, the plaques in both regions at 5 weeks showed the same NP accumulation, but those induced by low WSS at 9 weeks exhibited lower NP accumulation than plaques induced by multidirectional WSS. Correlations of NP accumulation to the features of plaques induced by low WSS revealed that this difference may be due to the presence of smooth muscle cells at the plaque-lumen interface (i.e., the cap). Overall, this result demonstrates the ability of NPs to identify different plaque phenotypes based on differences in passive accumulation. Future work will investigate NP-based diagnostics that employ active targeting strategies of the dysfunctional endothelium and plaque components to maximize accumulation and retention within different plaque types.

CHAPTER 3

Restoration of Normal Blood Flow in Atherosclerotic Arteries Promotes Plaque Stabilization

Published in iScience 2023.

3.1 Abstract

Blood flow is a key regulator of atherosclerosis. Disturbed blood flow promotes atherosclerotic plaque development, whereas normal blood flow protects against plaque development. We hypothesized that normal blood flow is also therapeutic, if it were able to be restored in atherosclerotic arteries. Apolipoprotein E-deficient ($ApoE^{-/-}$) mice were initially instrumented with a blood flow-modifying cuff to induce plaque development and then five weeks later the cuff was removed to allow restoration of normal blood flow. Plaques in decuffed mice exhibited compositional changes that indicated increased stability compared to plaques in mice with the cuff maintained. The therapeutic benefit of decuffing was comparable to atorvastatin and the combination had an additive effect. In addition, decuffing allowed restoration of lumen area, blood velocity, and wall shear stress to near baseline values, indicating restoration of normal blood flow. Our findings demonstrate that the mechanical effects of normal blood flow on atherosclerotic plaques promote stabilization summarized in Figure 3.1.

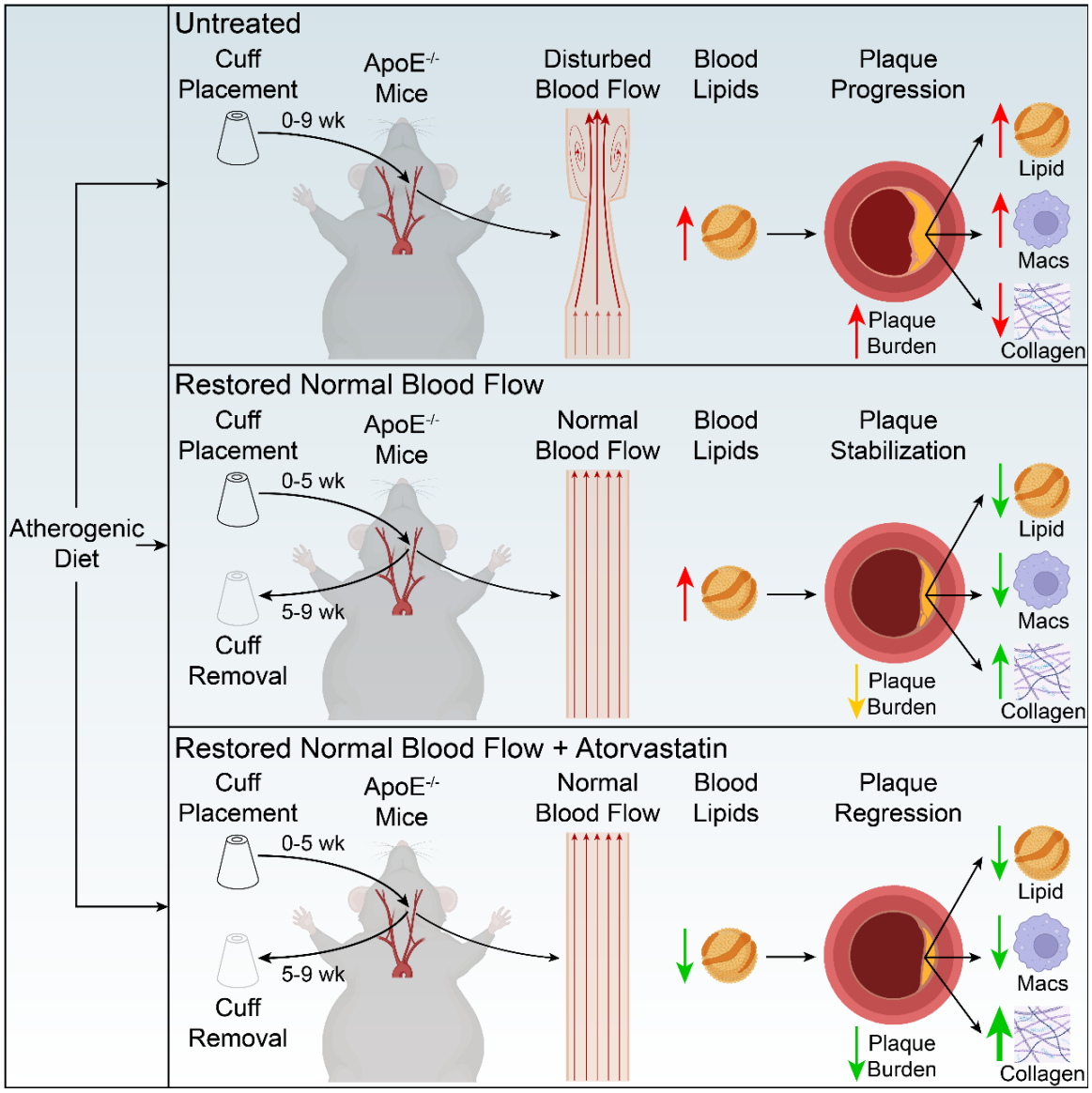

Figure 3.1. A graphical abstract. Overview of experimental study, procedures, and results.

3.2 Introduction

Blood flow within an artery is central to both the initiation and progression of atherosclerotic plaques [28, 66]. The interaction of blood flow with arteries of different geometries induces different mechanical shear stresses onto the endothelium of the inner artery wall [65]. The shear stress condition plays a key role in determining the susceptibility of an arterial segment to chronic inflammation and the accumulation of cholesterol-containing low density lipoprotein to form plaques [2]. Arterial segments

with bifurcations or high curvature that contain so-called disturbed blood flow and associated shear stresses promote plaque development [2, 66]. On the other hand, relatively straight arterial segments contain normal blood flow or unidirectional flow at a normal magnitude that protects against plaque development [65, 99]. While these relationships are well accepted, our understanding remains incomplete. It is still unknown what effect normal blood flow has on existing plaques, if it were able to be restored within atherosclerotic arteries.

Studies investigating the importance of blood flow in atherosclerosis have focused on associations between wall shear stress (WSS) metrics of disturbed flow and plaque features. They have consistently shown that plaques exposed to low WSS are associated with significantly increased burden, necrotic core area, lipids, and macrophages, as well as reduced fibrous cap thickness [27, 34, 35]. Pig studies have shown broadly similar results, demonstrating that arterial segments with low WSS are associated with the vulnerable plaque phenotype, thin cap fibroatheroma (TCFA), and numerous plaque features, including: increased plaque size, lipids, macrophages and other inflammatory markers, as well as decreased collagen and fibrous cap thickness [1, 12]. In addition to low WSS, studies in pigs and humans have also demonstrated that multidirectional WSS and the combination of low/multidirectional WSS is associated with many of these advanced plaque features [26, 100].

An important limitation of these studies is that they do not demonstrate a causal relationship between blood flow and plaque progression. Our study in pigs demonstrated that implantation of stenotic stents in the coronary arteries induced disturbed blood flow and caused the development of TCFA in regions of persistently low WSS [28]. This pig

model was motivated by a similar ApoE$^{-/-}$ mouse model wherein disturbed blood flow is induced by placement of a tapered cuff around one of the carotid arteries [25]. The arterial segments upstream and downstream of the cuff experience low WSS and low/multidirectional WSS, respectively, which causes plaque development in each region [39]. The upstream plaque exhibits an unstable phenotype that is lipid-rich with increased macrophages and inflammatory mediators and decreased collagen compared to the more stable downstream plaque [25, 33, 39, 67]. In line with the known atheroprotective effects of normal and high unidirectional WSS [65], neither the arterial segment within the tapered cuff nor the contralateral control artery develop plaques, despite the presence of severe hypercholesterolemia [25].

To date, studies of the relationship between blood flow and atherosclerosis have entirely focused on the deleterious effects of disturbed flow. This single direction of inquiry has greatly improved our ability to understand and predict atherosclerosis development. Yet, there remains a need for complementary studies investigating the potentially beneficial effects of normal blood flow that could lead to the development of novel therapeutics for atherosclerosis. The atheroprotective nature of normal blood flow suggests that it could be therapeutic, but this has not been directly evaluated. Therefore, in this study, we investigated the hypothesis that restoration of normal blood flow within atherosclerotic arteries promotes plaque stabilization. Our ApoE$^{-/-}$ mouse model provided the ideal platform for this investigation by allowing cuff placement to induce atherosclerosis followed by cuff removal or decuffing to restore normal blood flow. Flow restoration as a result of decuffing was demonstrated using serial *in vivo* magnetic resonance (MR) imaging and Doppler ultrasound. CFD modeling demonstrated restored

normal WSS conditions. Histology was performed to evaluate plaque burden, lipids, macrophages, and collagen. We found that plaques in decuffed mice, particularly those in the unstable plaque region, had significantly improved stability compared to those in the untreated cuffed mice. The extent of this plaque stabilization in decuffed mice was comparable to cuffed mice treated with atorvastatin and the combination of the two had an additive therapeutic effect.

3.3 Methods

3.3.1 Mouse Model and Experimental Groups

This study was carried out in strict accordance with the recommendations in the Guide for the Care and Use of Laboratory Animals of the National Institutes of Health. The protocol was approved by the Institutional Animal Care and Use Committee of the University of Nebraska-Lincoln (Project ID: 2007). A total of 75 Female ApoE$^{-/-}$ mice on a C57BL/6J background were acquired at 11 weeks of age (Jackson Labs, strain#002052) and maintained in cages with bedding and ad libitum food and water in an environmentally-controlled animal facility. Mice were immediately placed on an atherogenic diet (Envigo, TD.88137) that was maintained for the entirety of the experiments. Two weeks later (denoted week 0), all mice were instrumented with a blood flow-modifying cuff (Promolding) around the left common carotid artery and the contralateral carotid artery served as a control [25]. Surgeries were performed under isoflurane gas anesthesia (4-5% induction and 2-3% for maintenance) and sustained-release buprenorphine (1 mg/kg via subcutaneous injection) was given at the time of surgery to provide analgesia for 72 hrs.

Mice were randomly assigned to one of the following five experimental groups: (1) untreated with the cuff maintained for five weeks (5U), (2) untreated with the cuff maintained for nine weeks (9U), (3) treated with atorvastatin daily after five weeks of cuff placement and maintained with the cuff for an additional four weeks (9A), (4) treated with decuffing (to restore normal blood flow) after five weeks of cuff placement and maintained without the cuff for an additional four weeks (9D), and (5) treated with the combination of atorvastatin plus decuffing (9AD). All treatments commenced five weeks after initial cuff placement (denoted week 5) when plaques are at an intermediate stage of development.[25, 33] Both atorvastatin groups received 0.22 mg (~10 mg/kg) in an ORA-plus suspension vehicle by oral gavage daily from week 5 until the endpoint of the study at week 9. Total cholesterol was measured from a retro-orbital bleed in a subset of mice after a 4-hour fast at weeks -1 (prior to cuff placement), 4, 6 and 9 using a Piccolo Xpress blood chemistry analyzer (Abbott). Due to severe hypercholesterolemia, blood was mixed with an equal amount of PBS and measured. The resulting value was then doubled to get total cholesterol. Mice from all groups were humanely sacrificed at week 9, except the 5U group, which was humanely sacrificed at week 5 (Figure 3.2)

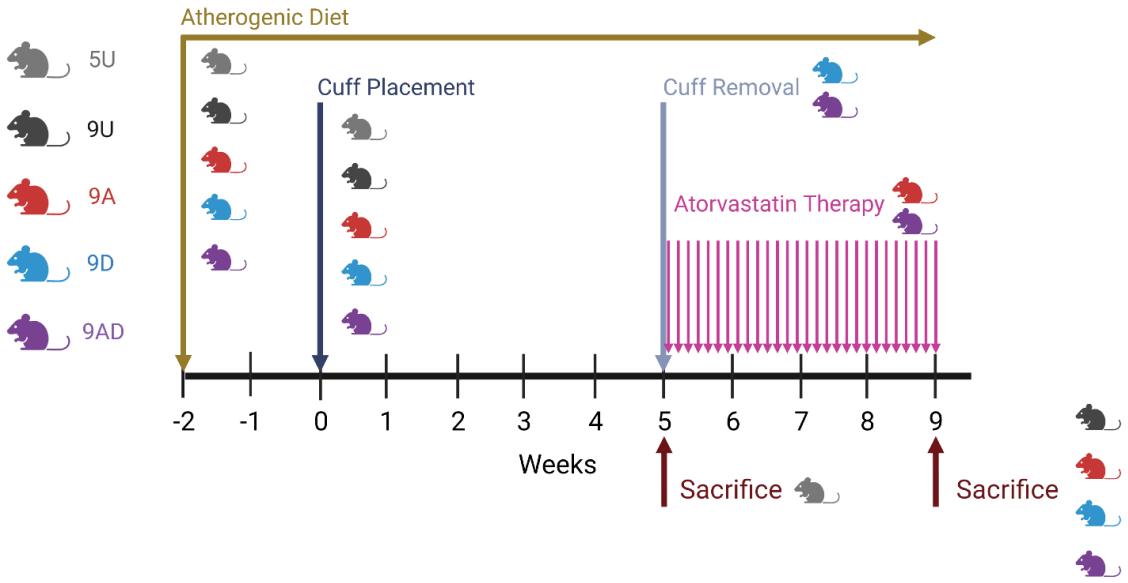

Figure 3.2. Diagram of the study experimental design. The experimental groups are: 5-Untreated (5U), 9-Untreated (9U), 9-Atorvastatin (9A), 9-Decuffed (9D), and 9-Atorvastatin-Decuffed (9AD). Created with BioRender.com.

3.3.2 Histology

Atherosclerotic plaque burden and constituents were assessed by histological processing of both carotid arteries from all mice. Mice were perfusion-fixed using 4% paraformaldehyde (Fisher Scientific) in PBS at mean arterial pressure. The carotid arteries, including the upper aortic arch and carotid bifurcations, were then extracted, embedded in OCT medium (Sakura), and snap frozen in a mixture of dry ice and isopentane (Sigma). The tissue block was cryosectioned at 8 µm thickness (Leica 1900CM) and serially collected from the innominate bifurcation of the right carotid artery to the bifurcation of both carotid arteries (thus, each cryosection contained one section from both the right and left carotid arteries). Sections were collected in a way to allow evaluation of multiple stains over the length of the arteries. This method provided an interval of 96 µm between sections for a given stain group.

Two basic stains were evaluated in this study. Oil red O (Sigma) staining was performed for evaluation of plaque burden and lipids. Picrosirius red (Sigma) staining

was used for evaluation of collagen. Plaque burden was computed as the percentage of plaque area to external elastic lamina area [101]. Basic stains were imaged with a Zeiss Axio Observer 5 microscope at 10X magnification using brightfield and polarized light, respectively. Stained regions of the oil red O and collagen section images were identified using a color threshold in ImageJ to render the images binary (for the collagen, two thresholds were used, one for red/yellow and the other for blue/green, and the results were summed). The threshold for each stain group of each mouse was the average identified by two independent observers who were masked to the identity of the experimental group (in the case of discrepancy, the two observers would discuss until a consensus was reached). The identified threshold was held constant for all images of a stain group in each mouse.

CD68 immunofluorescence staining was also performed to identify macrophages. The sectioned tissue was fixed in -20°C acetone for 10 min prior to staining. It was then incubated at room temperature with a rat polyclonal anti-CD68 primary antibody (BioLegend) in 10% goat serum (1:250) for 1 hour. The tissue was then washed with PBS and incubated at room temperature in the dark with goat polyclonal anti-rat preadsorbed secondary antibody conjugated to Alexa Fluor 647 (Abcam) in 10% goat serum (1:250) for 1 hour. The sections were then counterstained with DAPI (0.0025%, Abcam) and embedded in Prolong Gold Antifade Mountant (Thermo Fisher) with a coverslip. Imaging was performed on a Zeiss LSM 800 confocal microscope using a 2x2 tile scan at 20x magnification with excitation/emission wavelengths of 650/651-800 nm. All confocal parameters were held constant across all sections of all mice. The fluorescence images were then converted to greyscale.

Quantification of all stains was done using a custom MATLAB program, as previously described [33]. Briefly, each histological section was manually segmented using this program to identify the lumen, internal elastic lamina (IEL), and external elastic lamina (EEL) (for fluorescence images, a phase image was taken for each section that was used for segmentation). Once manually segmented, the program automatically identified the intima based on deviations between the lumen and internal elastic lamina contours (intima area was zero for non-diseased arterial sections). The binary (0 or 1) or greyscale (0 to 105) pixel values within the intima were then summed and normalized by the total number of pixels in the intima. For the greyscale CD68 stain, pixel values for all histological images of all mice were additionally normalized by 30 based on a manually identified threshold (mean value found across multiple sections of several representative mice) to allow the resultant magnitude to closely represent the percentage of stain area to intima area (versus stain intensity per intima area). For binarized stains (lipid and collagen), values are reported as the percentage of stain area to intima area. Since sections were serially collected, all viable sections from the middle of each plaque in each arterial segment immediately upstream and downstream of the cuff within each mouse were included in the quantitative analysis for each stain. Sections were excluded if they were missing, damaged, or at the ends of the plaque where clear tapering was evident. Viable sections were identified by two independent observers in a blinded manner. The mean percentage of stain area to intima area was typically obtained from 3-4 sections and used as the value for a given stain/arterial segment/mouse (represented as a single data point on the given plot).

3.3.3 Magnetic resonance imaging

Lumen patency of the instrumented carotid arteries was evaluated in mice from the 9U and 9D groups using serial MRI at -1 (before cuff placement), 1, 4, 7, and 9 weeks after initial cuff placement (the same mice were followed over all time points). Prior to imaging, mice were anesthetized using 2% isoflurane gas and affixed in a cylindrical animal holder to maintain head and body position during imaging. Breathing rates were monitored by a pressure-based sensor (SA Instruments), maintaining 50 to 80 breaths per minute over the course of the imaging sequence. The carotid arteries were imaged over 14 slices with 0.5 mm thickness per slice from the carotid bifurcation towards the aortic arch using a 9.4 T (400 MHz) 89 mm vertical bore Varian magnet with a 4 cm millipede RF imaging probe with triple axis gradients (100 G/cm max). Images were collected as a gradient echo sequence (GEMS) with FOV of 23x23 mm and 256x256 matrix for an in-plane resolution of 90 μm with a TR of 120 ms, TE of 4.29 ms and four averages. The left and right carotid arteries were both segmented from the MRI slices using ITK-SNAP and then imported into ImageJ to measure the lumen cross-sectional area and diameter of each carotid artery over the 14 slices (Figure 3.3A). Lumen area of the instrumented arteries at the point of maximum stenosis are reported as a percentage of lumen area prior to cuff placement (i.e., week -1).

3.3.4 Ultrasound

Blood velocity at the inlet of the carotid arteries was evaluated in a subset of the 9D mice used for MRI at the same weekly time points using the Vevo3100 (Fujifilm VisualSonics, Toronto, Canada) ultrasound system. An MX550D transducer (40 MHz center frequency) was used for Doppler Ultrasound imaging. Mice were anesthetized using 1-2% isoflurane with balance 100% O_2 and placed on a heated stage (37°C) in the

supine position. Hair on the neck region was removed (Nair) and ultrasound gel was applied liberally to the region. The transducer was placed in the sagittal plane along the carotid artery. Pulsed-wave Doppler measured blood velocity at the center of each artery over the cardiac cycle about 3 mm from the aortic bifurcation on both the left and right carotid arteries. Analysis of the data was done using Vevo Lab (version 5.6.1) offline. For comparisons over time, the average blood velocity at peak systole over three cardiac cycles is reported relative to baseline (i.e., week -1). For CFD analysis, the blood velocity averaged over three cardiac cycles was used for the inlet boundary condition.

3.3.5 Computational fluid dynamics

Mouse-specific CFD simulations were created using the MRI (vessel geometry) and Doppler ultrasound (inlet blood velocity) measurements (Figure3.3A and Figure 3.4, respectively) to determine wall shear stress in the instrumented artery at -1, 1, and 9 weeks after initial cuff placement (the same mice were followed over time). A custom MATLAB code was used to construct a point cloud of the artery by placing the best-fit lumen diameters from MRI on a straightened vessel centerline, thus neglecting the small curvature of the arteries from VMTKLab (Orobix). Flow extensions were added to the inlet and outlet at a length of 1.5- and 7-fold of each diameter, respectively, following previous work [27, 39, 100]. The surface of the artery was then converted into an STL file, and the fluid domain was fully meshed with tetrahedral elements using Tetgen (WIAS). The surface of the artery was then converted into an STL file, and the fluid domain was fully meshed with tetrahedral elements using TetGen (WIAS). We focused our analysis on the segments of the instrumented artery over the first 2 mm immediately upstream and downstream of the cuff because this is where plaque formation occurs (at

the time prior to cuff placement or after decuffing when the exact location of the previous cuff placement could not be determined, the central portion of the artery was used). Here, a maximum element side length of 0.013 mm was assigned. The portions of the artery beyond these regions were assigned slightly courser mesh densities based on maximum element side lengths of 0.025 mm (2-3 mm away from the cuff) and 0.05 mm for the rest of the artery. This approach resulted in a total mesh density of approximately 2M elements for the cuffed arteries (week 1) and 2.5M elements for the baseline (week -1) and decuffed (week 9) arteries. The final mesh density was determined using a convergence test with a criteria of <2% in time-averaged wall shear stress (TAWSS).

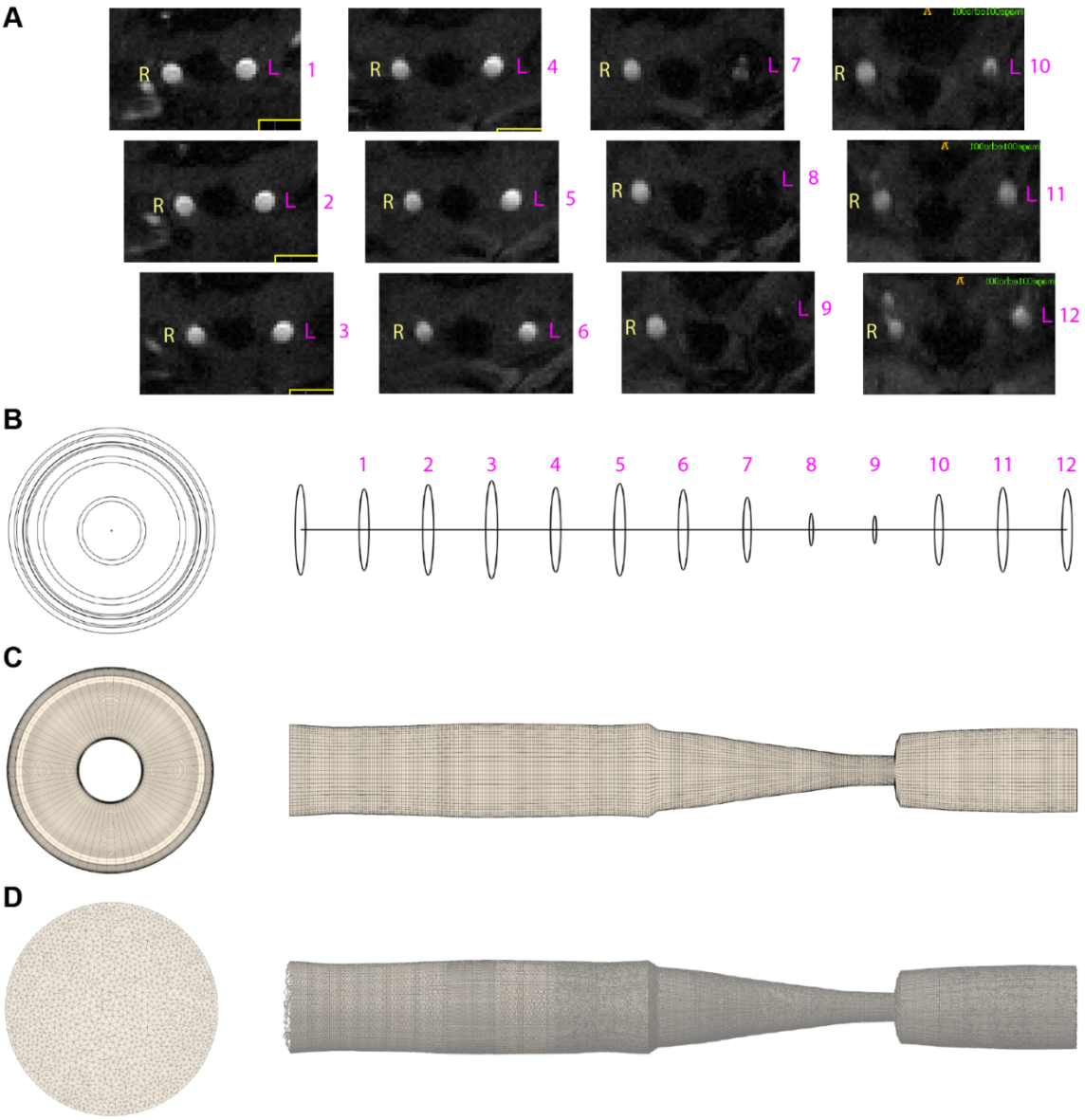

Figure 3.3. Workflow for developing CFD meshes of the carotid arteries from MRI, related to STAR Methods. (A) MRI slices through both carotid arteries of a representative mouse instrumented with a blood flow-modifying cuff around the left carotid artery. The left (L) and right (R) arteries are identified in each image. (B-D) The cuffed artery reconstruction at three stages showing both cross-section and side views. **(B)** The best-fit diameter obtained from each MRI slice was placed along a straightened centerline (curvature of the arteries was neglected in our CFD models). **(C)** Each artery segment—upstream, cuff, and downstream—was smoothed and the vessel discretized using a user-defined number of nodes for export as a surface mesh. **(D)** The surface mesh was imported into TetGen and the fluid domain meshed using tetrahedral elements. Note: inlet and outlet vessel extensions are not shown for clarity.

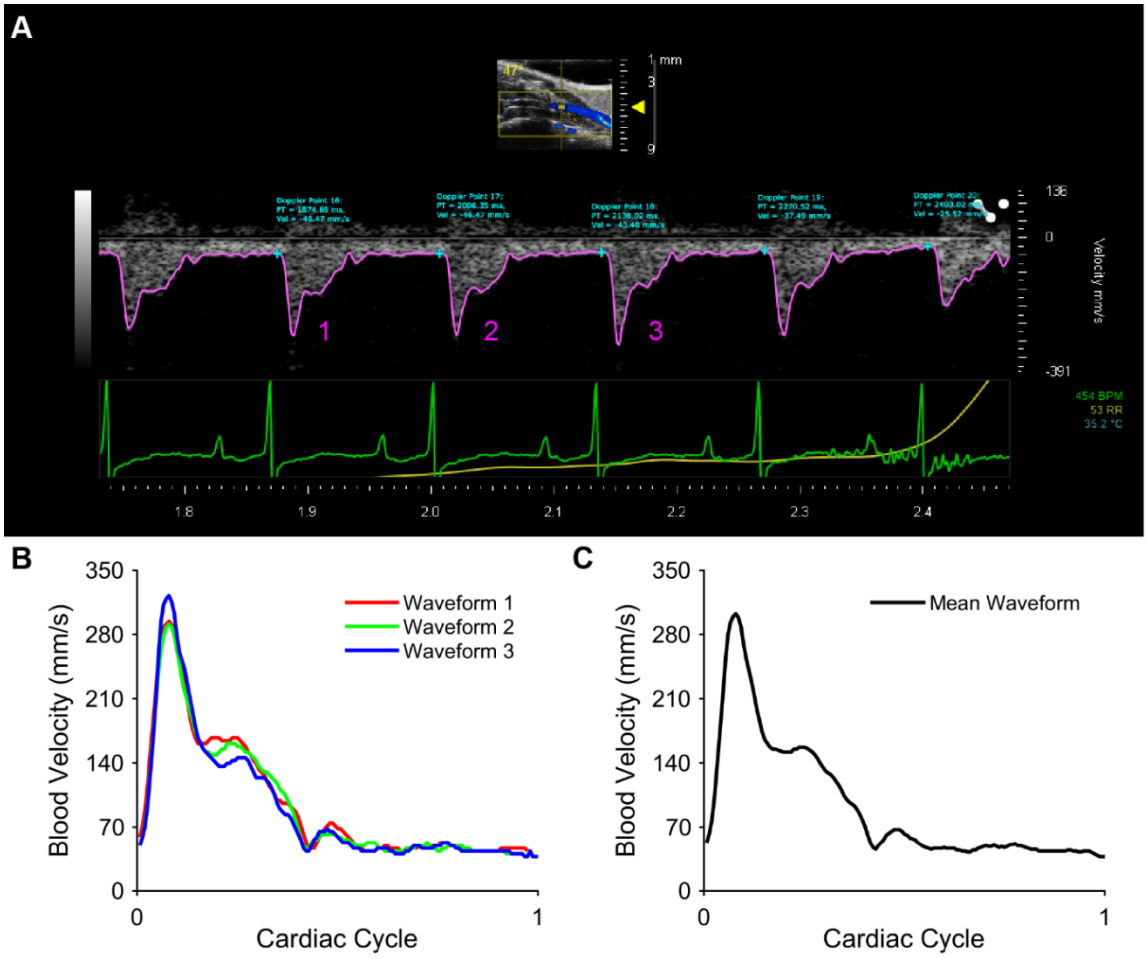

Figure 3.4. Workflow for creating inlet blood velocity waveforms from Doppler ultrasound for the CFD models, related to STAR Methods. (A) Raw blood velocity waveforms (pink lines) measured with Doppler ultrasound and heart rate (green line) from the left carotid artery of a representative mouse prior to cuff placement (week -1). **(B)** Plot of three waveforms extracted from the raw ultrasound data. **(C)** Mean of the three waveforms, which is used as the inlet boundary condition for the CFD model associated with this mouse and time point.

Each meshed artery was imported into Abaqus to perform CFD on a computing cluster in the Holland Computing Center at the University of Nebraska using 256 cores per simulation (Figure 3.3 C&D). CFD models were setup using the same general approach as our previous work [39]. Briefly, blood was assumed to be an incompressible Newtonian fluid with a viscosity of 3.5 mPa.s and density of 1050 kg/m^3. The inlet of each artery was prescribed the mean pulsatile blood velocity waveform over the cardiac cycle obtained from Doppler ultrasound for each mouse at each time point and we

assumed a plug profile over the vessel cross-section (Figure 3.3B). The outlet was prescribed a pressure of zero and the artery wall was prescribed a no-slip boundary condition. Each simulation was run over three cardiac cycles to ensure fully-developed flow (Figure 3.4B). We observed that shear stress values between the second and third cardiac cycles changed less than 2%, demonstrating convergence. A WSS vector was obtained for each element of the mesh from the third cardiac cycle and imported into a custom MATLAB program to quantify the magnitude of WSS at peak systole, TAWSS, and oscillatory shear index (OSI) [28, 39]. Mean values of WSS at peak systole and mean non-zero values of OSI are reported over the 2 mm artery segments immediately upstream and downstream of the cuff (OSI was averaged over elements containing non-zero values—greater than or equal to 0.01—within the analysis regions because OSI localizes to particular portions of recirculation zones; when no values of OSI were greater than or equal to 0.01, the mean was taken over the entire artery segment).

3.3.6 Statistical Analysis

All statistical tests were performed in Minitab. Quantities are reported as mean ± standard deviation (SD). For unpaired data, if the data were normally distributed (determined by a Shapiro-Wilk test), group comparisons were performed using a one-way analysis of variance (ANOVA) and pairwise comparisons, including those post-hoc of the ANOVA, were performed using an unpaired *t* test with equal or unequal variances based on an F-test. Otherwise, a Kruskal-Wallis test (group comparisons) and Mann Whitney U test (pairwise comparisons) with Levene's test for variances were used. For paired data, a repeated-measures ANOVA for group comparisons and paired *t*-test for individual comparisons was used for normally distributed data, otherwise a Friedman test and

Wilcoxon ranked-sum test were used. Pairwise comparisons were done using a one-tailed approach when the hypothesized effect was direction dependent or a two-tailed approach when it was not. Multiple comparisons were accounted for using a Bonferroni-Holm correction method. An adjusted *p*-value of less than 0.05 was considered statistically significant.

3.4 Results

All mice were placed on an established atherogenic diet for the entirety of the experiments that induced severe hypercholesterolemia (Figure 3.1), in line with previous reports [102, 103]. All treatments (decuffing, atorvastatin, and decuffing plus atorvastatin) started five weeks after initial cuff placement. Cholesterol was plotted at 4 different time points to ensure that mice had equally high cholesterol before and after cuffing and decuffing procedures. Additionally, it was shown that atorvastatin significantly lowered cholesterol the last 4 weeks of the study while the mice not treated with atorvastatin maintained high cholesterol (Figure 3.5).

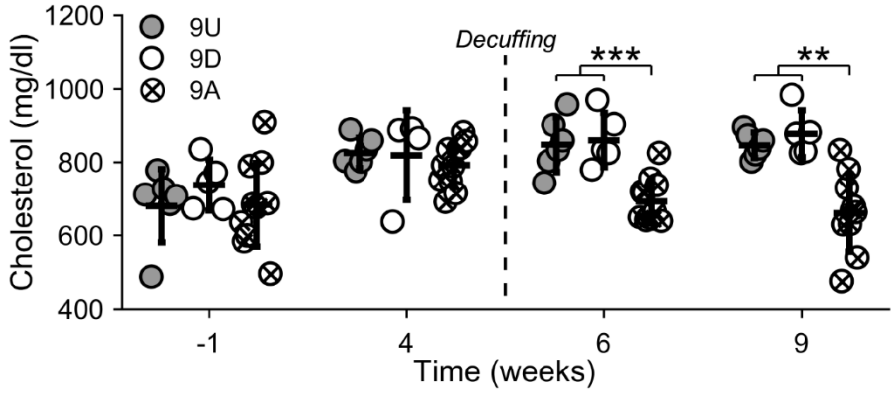

Figure 3.5. The Envigo (Teklad) Atherogenic Diet fed to ApoE$^{-/-}$ mice induces severe hypercholesterolemia and atorvastatin reduces cholesterol levels, a validation related to STAR Methods. Total cholesterol (n=5-11 mice per group) was measured from a retro-orbital bleed after a 4 h fast using a Piccolo Xpress blood chemistry analyzer (Abbott) in the 9-Untreated (9U), 9-Decuffed (9D), and 9-Atorvastatin (9A) over time. Bars represent mean±SD. *Indicates statistically significant difference for comparison given parenthetically, wherein **p<0.01 and ***p<0.001.

3.4.1 Decuffing promotes plaque stabilization comparable to treatment with atorvastatin and the combination has an additive therapeutic effect

To evaluate the therapeutic benefit of decuffing alone and in combination with atorvastatin, mice were randomly assigned to one of the following five experimental groups: (1) untreated with the cuff maintained for five weeks (5U), (2) untreated with the cuff maintained for nine weeks (9U), (3) treated with atorvastatin daily after five weeks of cuff placement and maintained with the cuff for an additional four weeks (9A), (4) treated with decuffing (to restore normal blood flow) after five weeks of cuff placement and maintained without the cuff for an additional four weeks (9D), and (5) treated with the combination of atorvastatin plus decuffing (9AD). All treatments commenced five weeks after initial cuff placement (denoted week 5) when plaques are at an intermediate stage of development [13, 15]. A summary of the experimental protocol is given in Figure 3.1.

Placement of a blood flow-modifying cuff around the left carotid artery of $ApoE^{-/-}$ mice induced the development of plaques in both the unstable (upstream) and stable (downstream) plaque regions. In the unstable plaque region, decuffed mice exhibited significant changes in plaque composition (Figure 3.6A). In this treatment group (9D) compared to untreated groups (5U and 9U), lipid content was lower (4.8±4.5% versus 8.9±2.3% (p=0.04) and 17.2±9.4% (p=0.005), respectively) (Figure 3.6B), plaque macrophage (CD68+ cells) content was lower (9.3±6.9% versus 25.9±8.5% (p=0.0002) and 4.0±1.8% (p=0.001), respectively) (Figure 3.6C), and plaque collagen content was higher (9.3±3.1% versus 3.8±2.1% (p=0.004) and 4.9±2.0% (p=0.005), respectively) (Figure 3.6D). Similar results were seen in mice treated with atorvastatin (9A) and there were no significant differences in plaque composition between the 9A and 9D groups.

The mice treated with the combination of atorvastatin plus decuffing (9AD) exhibited similar plaque lipid and macrophage contents, but higher collagen content compared to the individual treatment groups (15.7±4.2% versus 8.2±5.4% (p=0.01) and 9.3±3.1% (p=0.008) for the 9A and 9D groups, respectively) (Figure 3.6B-D).

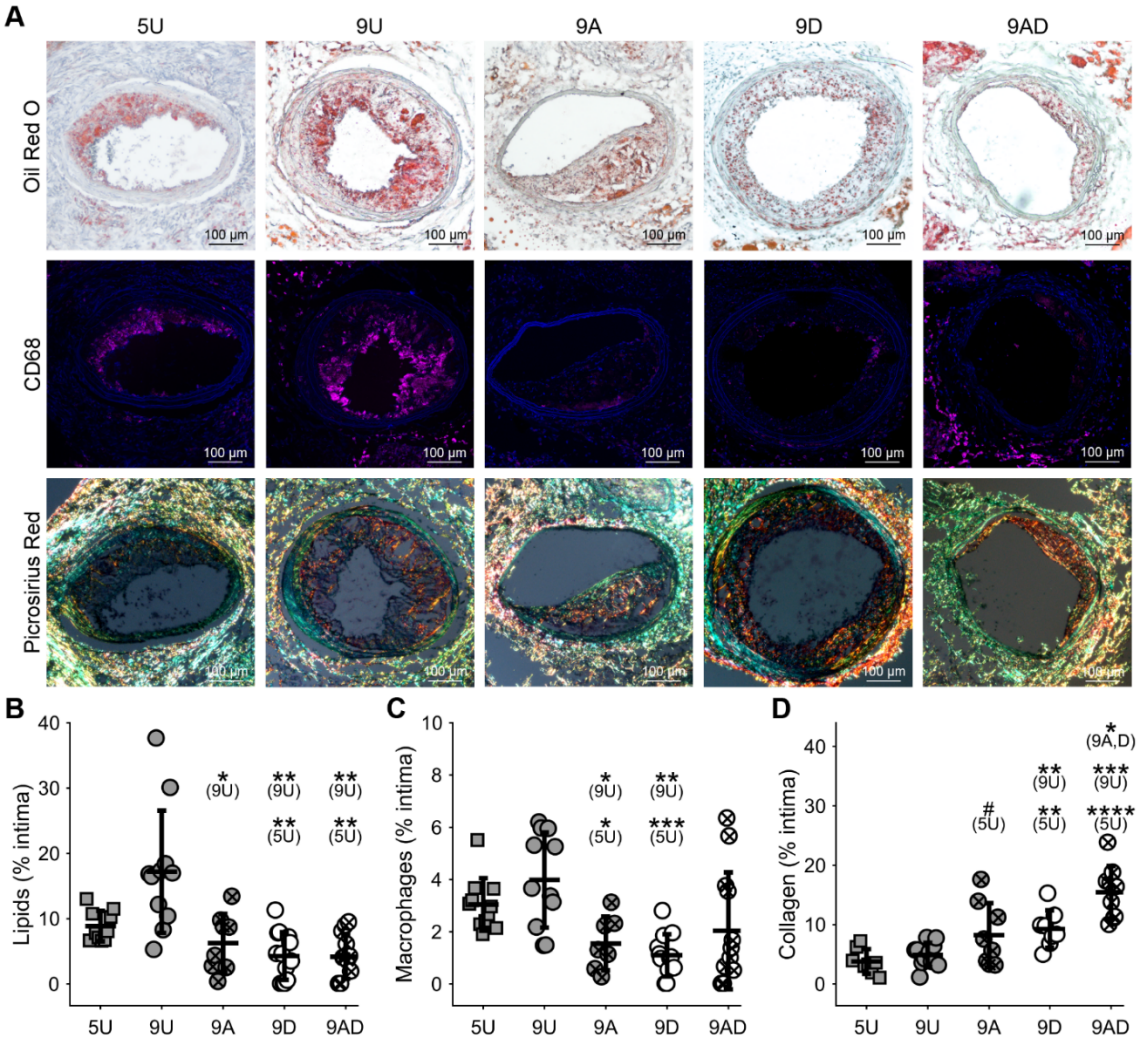

Figure 3.6. Decuffing to restore normal blood flow promotes increased stability of plaques in the unstable (upstream) plaque region comparable to treatment with atorvastatin and the combination induces an additive therapeutic effect. (A) Representative histology sections stained for oil red O (lipids), CD68 (macrophages), and picrosirius red (collagen) for the 5-Untreated (5U), 9-Untreated (9U), 9-Atorvastatin (9A), 9-Decuffed (9D), and 9-Atorvastatin-Decuffed (9AD) groups. **(B-D)** Box plots of **(B)** lipids (n=8-13 mice per group), **(C)** macrophages (n=7-12 mice per group), and **(D)** collagen (n=8-11 mice per group) content. Bars represent mean±SD. *Indicates statistically significant difference for comparison given parenthetically, wherein $^{\#}p<0.1$, $^{*}p<0.05$, $^{**}p<0.01$, $^{***}p<0.001$, and $^{****}p<0.0001$. See also **Table S3.1** for statistical anaylsis.

In the stable plaque region, the 9AD group also exhibited the most substantial changes in plaque composition (Figure 3.7A). Here, plaque lipid content was similar between experimental groups, except the 9AD group, which exhibited a lower value (3.0±1.9%) compared to the 5U (6.7±4.8%, p=0.07), 9U (7.8±5.4%, p=0.07), and 9D (6.0±3.8%, p=0.07) groups, though the adjusted p-values were just above the threshold for significance (Figure 3.7B). The 9AD group also exhibited the lowest plaque macrophage content compared to the other groups, though none of the comparisons reached significance (Figure 3.7C). However, collagen content was significantly higher in all treatment groups compared to the untreated groups (except 9A versus 5U) and the 9AD group had the highest plaque collagen content of 24.5±6.2%. This value was significantly higher than the 5U (9.3±4.3%, p<0.0001), 9U (9.6±5.4%, p<0.0001), and 9D (17.1±5.0%, p=0.03) groups (Figure 3.7D).

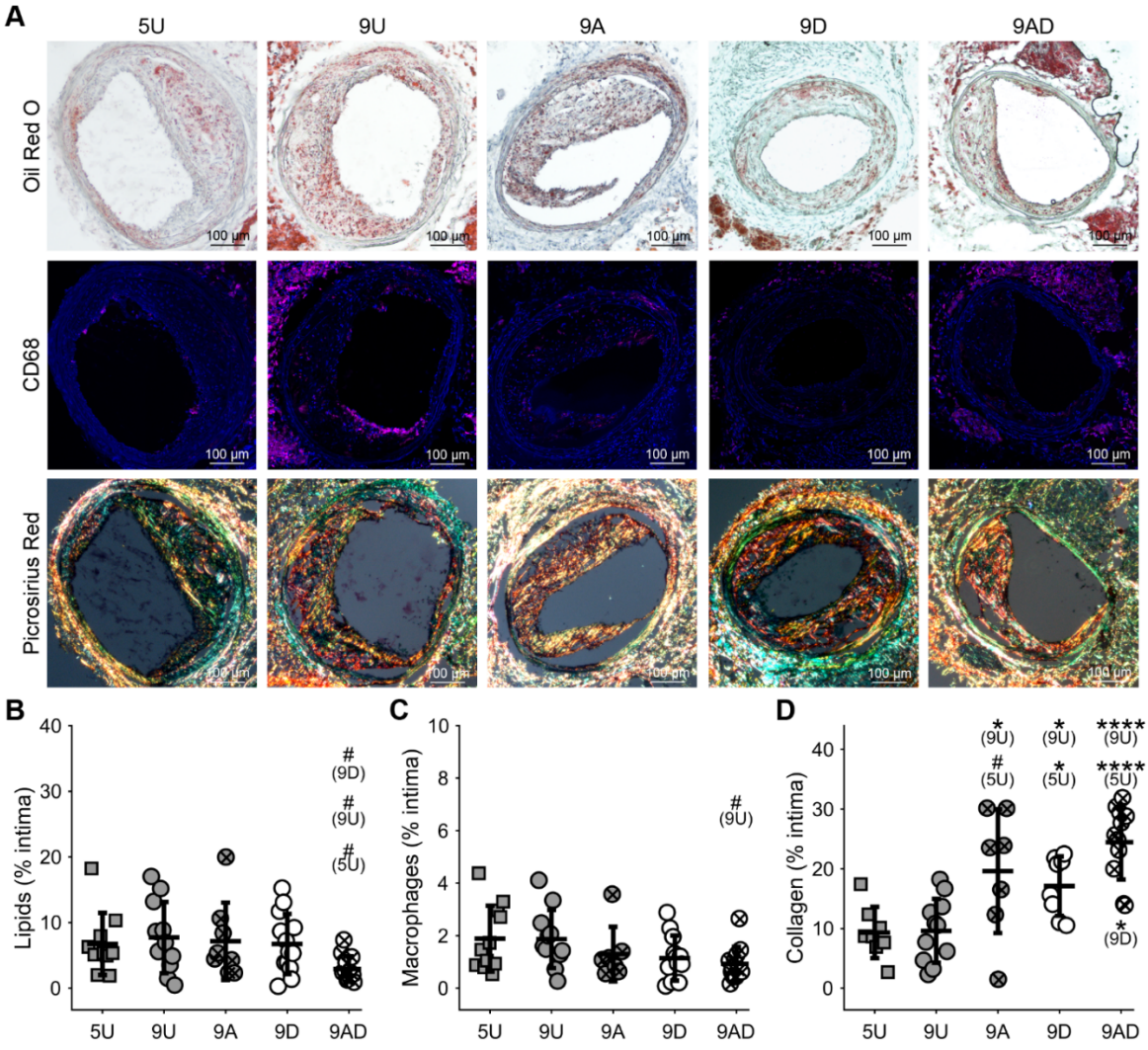

Figure 3.7. Decuffing to restore normal blood flow promotes increased stability of plaques in the stable (downstream) plaque region comparable to treatment with atorvastatin and the combination induces an additive therapeutic effect. (A) Representative histology sections stained for oil red O (lipids), CD68 (macrophages), and picrosirius red (collagen) for the 5-Untreated (5U), 9-Untreated (9U), 9-Atorvastatin (9A), 9-Decuffed (9D), and 9-Atorvastatin-Decuffed (9AD) groups. **(B-D)** Box plots of **(B)** lipids (n=8-13 mice per group), **(C)** macrophages (n=7-12 mice per group), and **(D)** collagen (n=7-11 mice per group) content. Bars represent mean±SD. *Indicates statistically significant difference for comparison given parenthetically, wherein $^{\#}p<0.1$, $^{*}p<0.05$, and $^{****}p<0.0001$. See **Table S3.2** for statistical analysis.

All treatment groups had reduced plaque vulnerability compared to the 5U and 9U groups, but it was only significant in the upstream region (Figure 3.8 A&B). The upstream plaque had significantly different vulnerability indices with all treatment group having more stability that the 5U and 9 U groups ($p<0.01$). Vulnerability index is the ratio between the product of lipid and macrophage concentration, to the concentration of

collagen. This suggests that the upstream is in fact a more vulnerable or unstable plaque compared to the downstream. All treatment groups had reduced plaque burden compared to the 9U group, but it was only significant in the 9AD group. This reduction was found in both the unstable (22.7±18.0% versus 43.5±12.8%, p=0.02) and stable (28.9±10.7% versus 47.2±13.6%, p=0.007) plaque regions (Figure 3.8 C&D). These results indicate that the combination of restored normal blood flow and atorvastatin promotes plaque regression, as well as improved plaque stability.

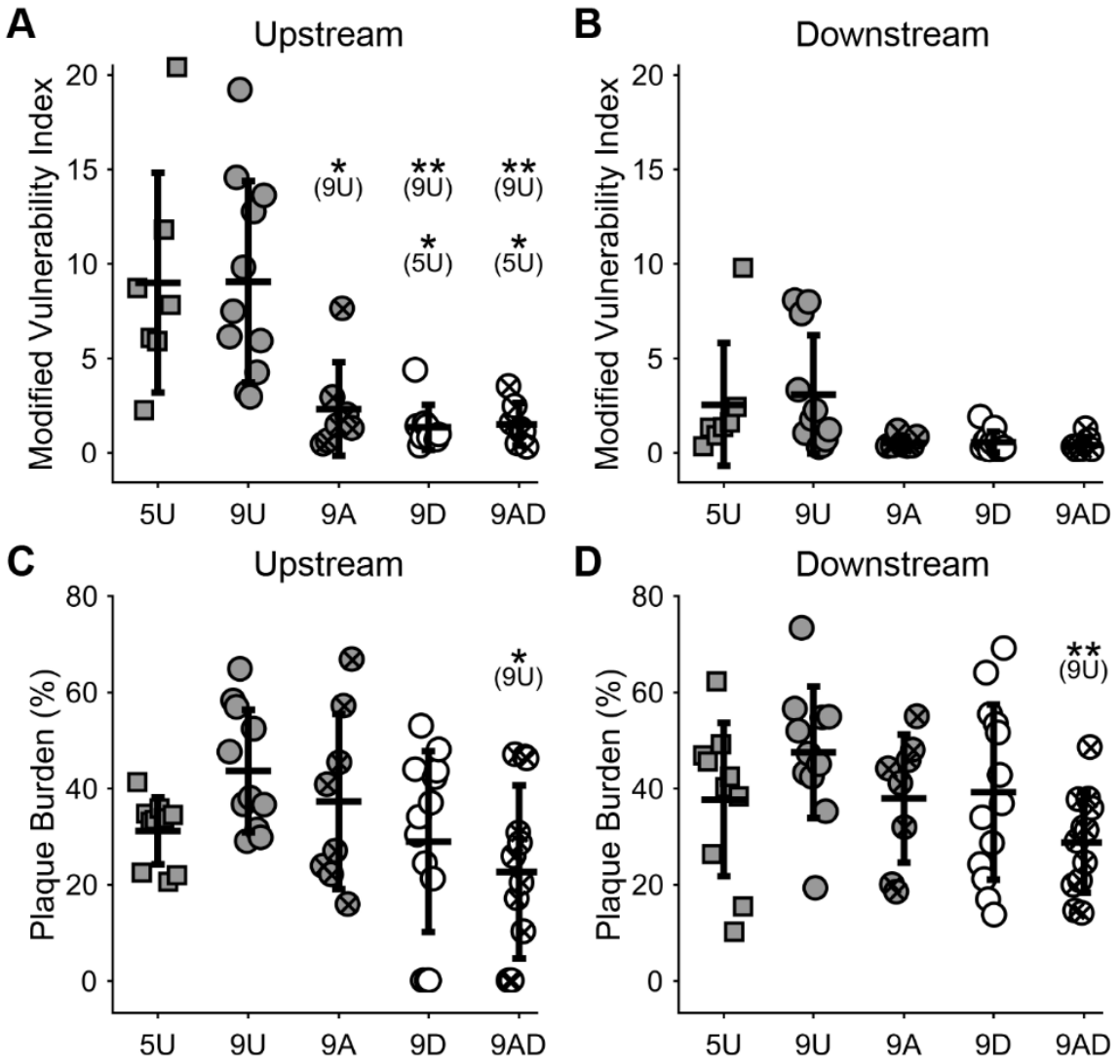

Figure 3.8. The combination of atorvastatin and decuffing reduces plaque burden and vulnerability index. Plaque burden in the **(A&C)** upstream (unstable plaque) and **(B&D)** downstream (stable plaque) regions of the instrumented artery (n=8-13 mice per group). Experimental groups include the 5-Untreated (5U), 9-Untreated (9U), 9-Atorvastatin (9A), 9-Decuffed (9D), and 9-Atorvastatin-Decuffed (9AD). *Indicates statistically significant difference for comparison given parenthetically, wherein *$p<0.05$ and **$p<0.01$. See also **Table S3.3** for statistical analysis.

3.4.2 Decuffing restores artery lumen area, blood velocity, and wall shear stress

To demonstrate that decuffing restores normal blood flow, we evaluated lumen area at the point of maximum stenosis using MRI and inlet blood velocity using Doppler ultrasound for both the left (instrumented) and right (uninstrumented control) carotid arteries of decuffed mice (9D) at -1 (baseline), 1 (cuffed), 4 (cuffed), 7 (two weeks after

decuffing), and 9 (four weeks after decuffing) weeks after initial cuff placement. These data are reported relative to baseline (i.e., before initial cuff placement). One week after initial cuff placement, the left carotid artery of 9D mice exhibited a dramatic reduction in lumen area at the point of maximum stenosis compared to the control artery (13.7±5.2% versus 99.6±17.4%, $p<0.0001$) (Figures 3.9). This reduction was similar at four weeks (16.7±5.8% versus 100.5±11.6%, $p<0.0001$). Two weeks after decuffing, the maximum stenosis had dramatically improved (74.8±21.2% versus 103.9±19.5%, $p=0.004$) and, at four weeks after decuffing, there was no significant difference between the left and right carotid arteries of the 9D mice (84.3±18.1% versus 97.3±14.6%, $p=0.07$). We also evaluated lumen area restoration in 9D versus 9U mice (Figure 3.10). No statistical differences were seen at 1 and 4 weeks after cuffing, but at 7 and 9 weeks, as lumen area was restored in the 9D mice, both time points were significantly different between the two groups (74.8±21.2% versus 20.1±10.2% ($p<0.0001$) and 84.3±18.1% versus 21.0±9.6% ($p<0.0001$) at 7 and 9 weeks, respectively).

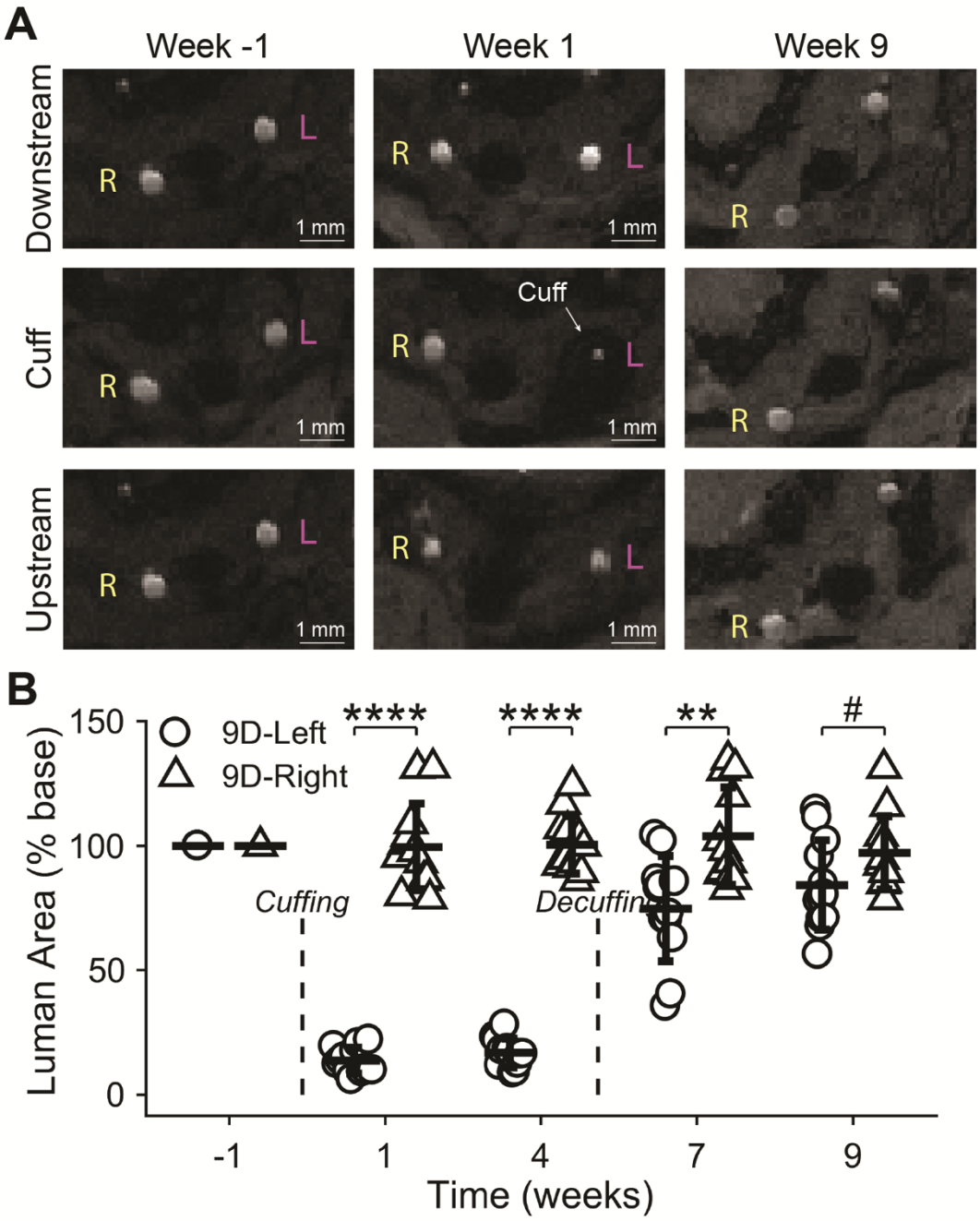

Figure 3.9. Decuffing restores normal carotid artery lumen patency. Imaging and modeling data from the 9-Decuffed (9D) group of mice. **(A)** Representative MRI slices of the downstream (stable plaque), cuff, and upstream (unstable plaque) regions of an instrumented carotid artery at -1 (baseline), 1 (cuffed), and 9 (decuffed) weeks after initial cuff placement. **(B)** Box plot of lumen area as a percentage of baseline in the instrumented versus contralateral control arteries at -1, 1, 4, 7, and 9 weeks (n=12 mice). Bars represent mean±SD. *Indicates statistically significant difference for given comparison, wherein $^{\#}p<0.1$, $^{*}p<0.05$, $^{**}p<0.01$, $^{***}p<0.001$, and $^{****}p<0.0001$. See **Table S3.4.**

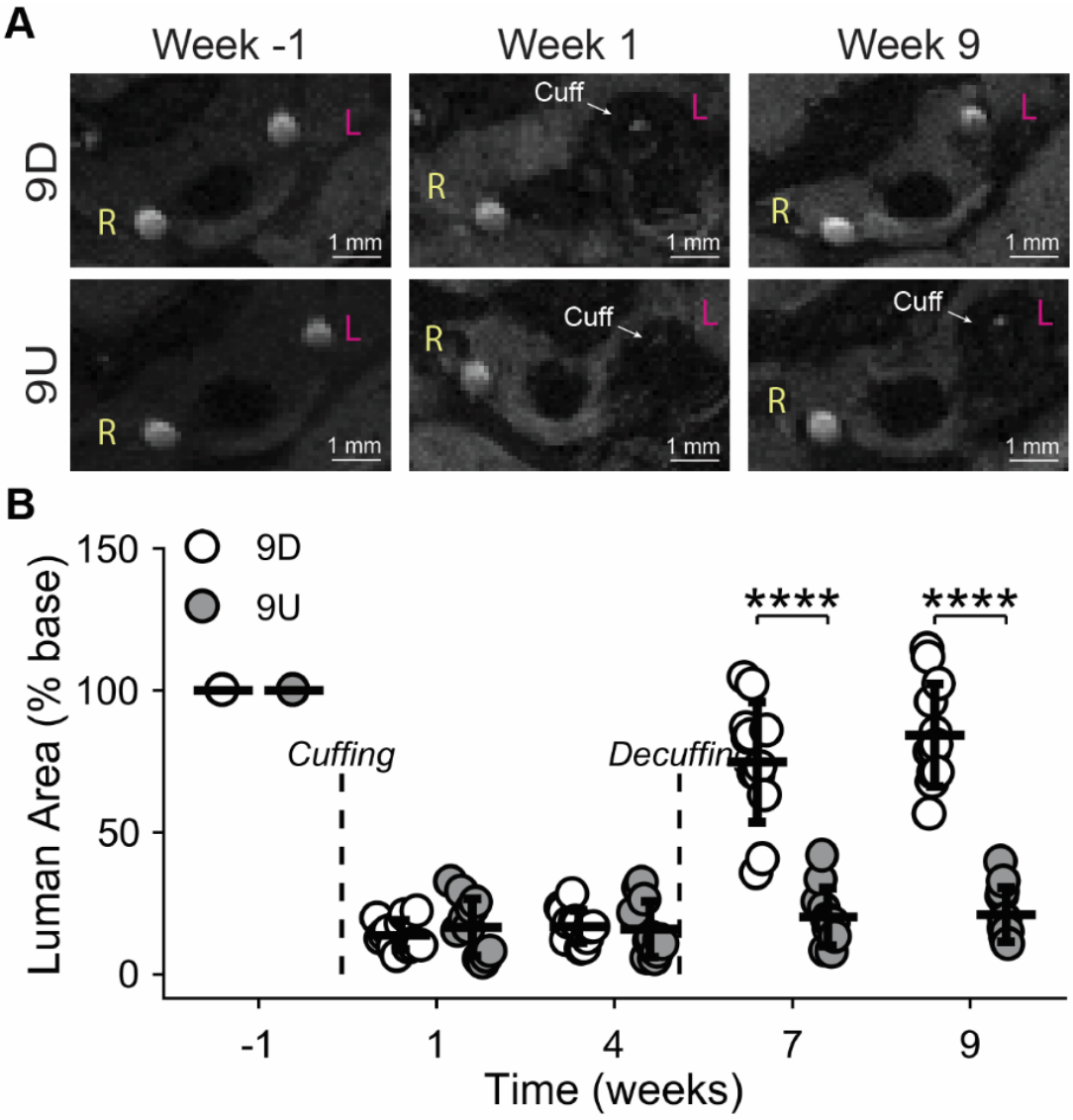

Figure 3.10. Decuffing restores carotid artery lumen patency compared to maintaining the cuff for the duration of the experiments, related to Figure 5. (A) Representative MRI slices within the cuff region (or center of the artery in the case of baseline) from the 9-Decuffed (9D) and 9-Untreated (9U) groups. **(B)** Box plot of lumen area as a percentage of baseline in the instrumented arteries from the 9D (n=12 mice) versus 9U (n=11 mice) groups at -1, 1, 4, 7, and 9 weeks after initial cuff placement. Bars represent mean±SD. *Indicates statistically significant difference for given comparison, wherein ****p<0.0001. See also **Table S3.4**.

Peak systolic blood velocity at the inlet of each carotid artery of the 9D mice from Doppler ultrasound showed a nearly identical trend to the MRI data. The left carotid artery exhibited a dramatic reduction in blood velocity compared to the control artery at both one (55.9±8.8% versus 107.9±16.8%, p<0.0001) and four (56.5±10.6% versus

113.8±18.5%, p<0.0001) weeks after initial cuff placement (Figures 3.11). Two weeks after decuffing, the blood velocity had increased in the instrumented arteries and was no longer statistically different from the control arteries (84.0±21.6% versus 104.0±30.3%, p=0.37). Similar blood velocities were seen at four weeks after decuffing (82.6±20.2% versus 93.9±17.7%, p=0.31).

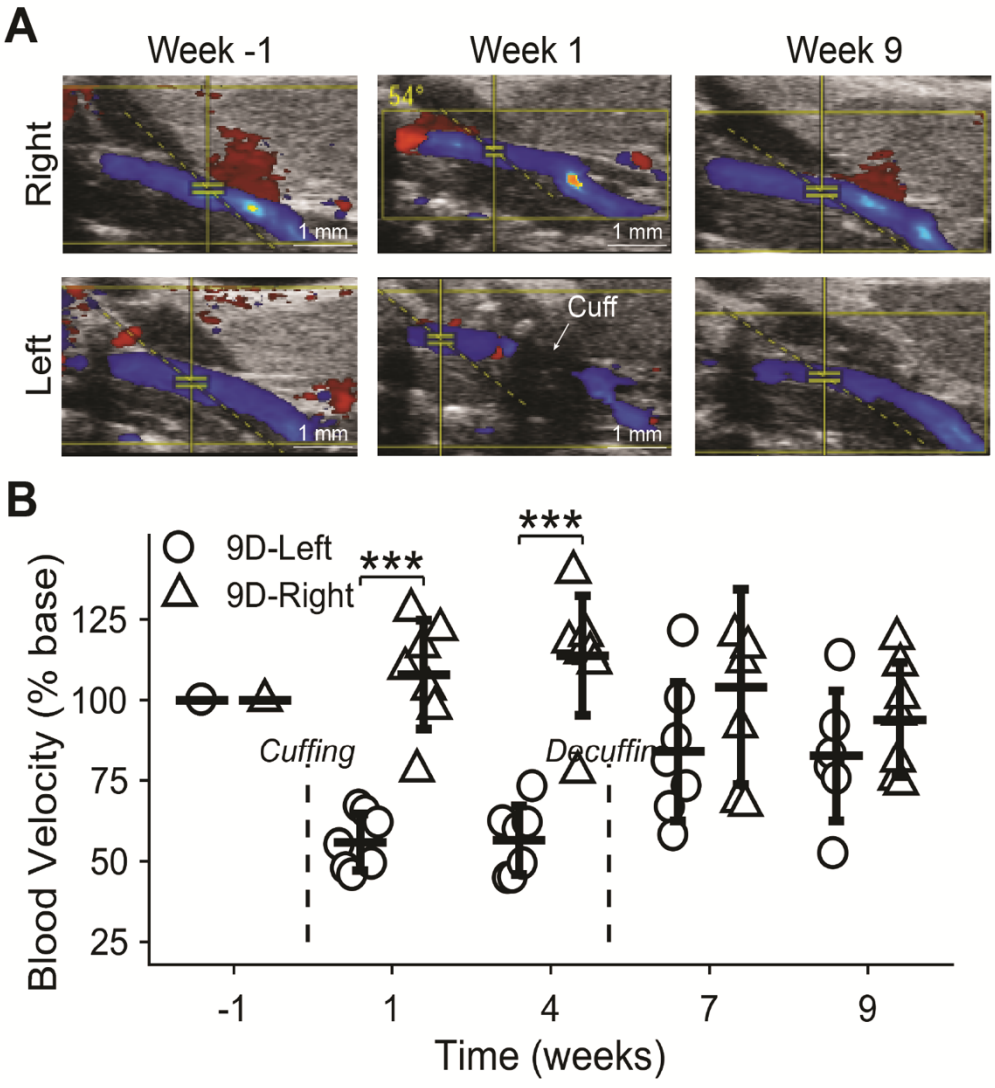

Figure 3.11. Decuffing restores normal carotid artery blood velocity. (A) Representative ultrasound images of the instrumented and contralateral control arteries at -1, 1, and 9 weeks. **(B)** Box plot of blood velocity as a percentage of baseline over time after initial cuff placement (n=7 mice). Bars represent mean±SD. *Indicates statistically significant difference for given comparison, wherein #p<0.1, *p<0.05, **p<0.01, ***p<0.001, and ****p<0.0001. **See Table S3.4**.

Finally, since WSS is the mechanical metric of flow that is most often associated with atherosclerosis, we also performed CFD of the instrumented carotid arteries of 9D mice at -1, 1, and 9 weeks after initial cuff placement to characterize the degree of WSS restoration that results from decuffing. Simulations were performed in a mouse-specific manner using the vessel geometry from MRI and inlet blood velocity over the cardiac cycle from ultrasound (Figure 3.12A) for a given mouse at each time point with the same mice followed over time. This approach provided a complete picture of the effects of decuffing on WSS by evaluating the same arteries at baseline (week -1), after cuff placement (week 1), and then four weeks after decuffing when lumen area (MRI) and blood velocity (ultrasound) were maximally restored (week 9). We evaluated two WSS metrics, WSS at peak systole (pWSS) to quantify magnitude and oscillatory shear index (OSI) to quantify multidirectionality over the cardiac cycle.

Importantly, our CFD models predicted trends over time that were consistent with the MRI and ultrasound data. The CFD models at 9 weeks (four weeks after decuffing) clearly demonstrated resolution of disturbed flow in the instrumented artery, including the complex flow profile in the downstream segment (Figure 3.12B). Evaluation of mean WSS at peak systole and oscillatory shear index (OSI, a metric of shear multidirectionality over the cardiac cycle) demonstrated no significant differences in either metric between baseline (week -1) and four weeks after decuffing (week 9) for either the upstream (unstable plaque) or downstream (stable plaque) regions (Figure 3.13). In the upstream region, pWSS was dramatically reduced by cuff placement (week 1) compared to both baseline at week -1 (7.8±2.3 Pa versus 14.4±3.3 Pa, p=0.009) and decuffed at week 9 (7.8±2.3 Pa versus 12.8±2.3 Pa, p=0.009). In addition, there was no

difference between the baseline and decuffed time points (p=0.37), demonstrating that WSS magnitude was restored (the upstream segment does not experience multidirectional flow, so OSI was zero across all time points). Similar peak WSS results were seen in the downstream region, though values did not reach significance. In addition, mean OSI in the downstream region at week 1 (0.18±0.08) was significantly higher compared to baseline (0.00±0.00, p=0.003) and week 9 (0.00±0.00, p=0.003). Thus, in both the upstream and downstream segments, WSS magnitude and directionality returned to baseline. These results demonstrate that cuff placement induced WSS conditions associated with disturbed blood flow, while cuff removal allowed restoration of normal wall shear stress conditions.

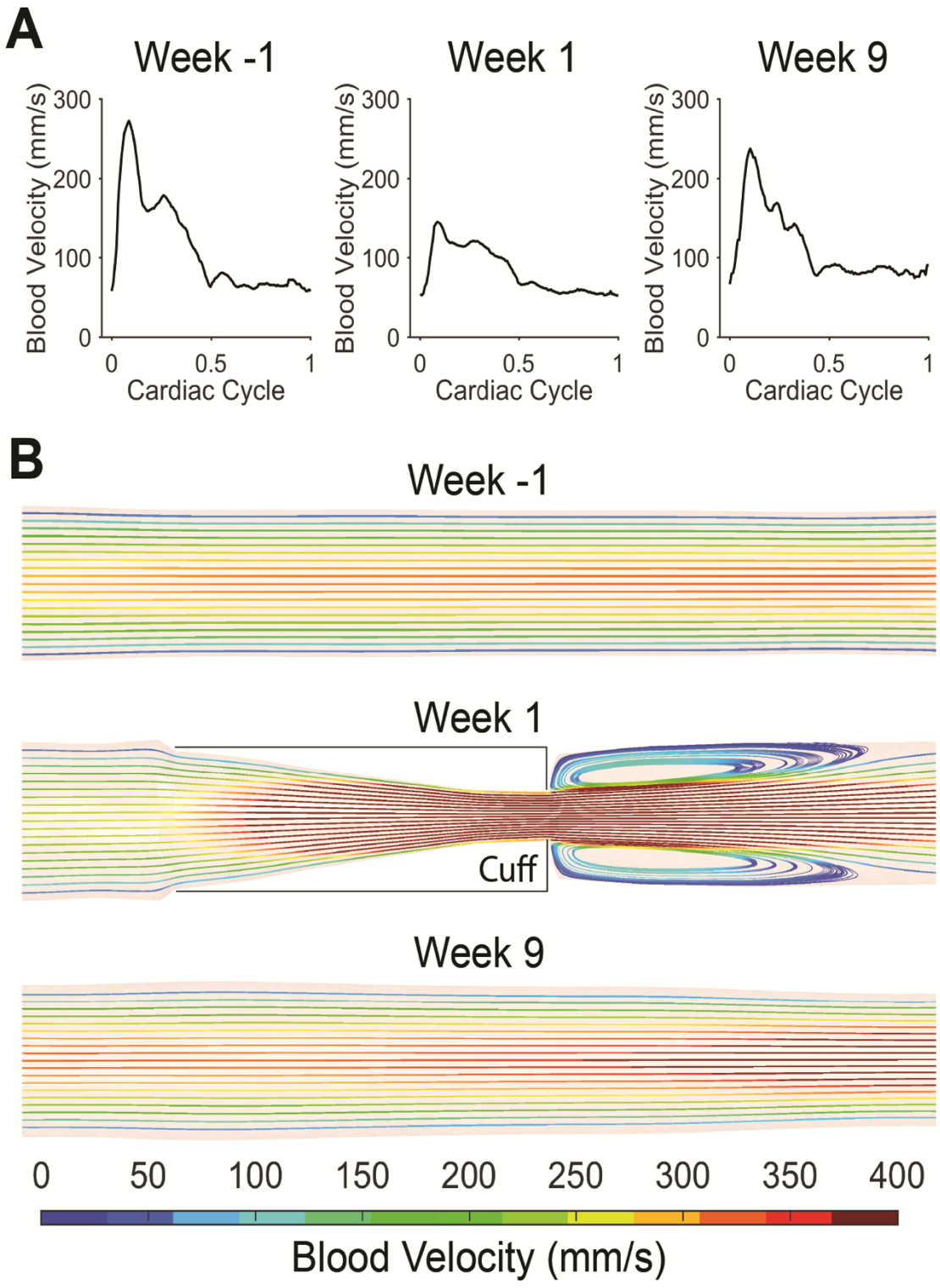

Figure 3.12. (A) Representative blood velocity waveforms over the cardiac cycle (time is normalized) from one 9D mouse. **(B)** Representative CFD model of the instrumented carotid artery with blood velocity streamlines from one 9D mouse over time (blood flow is left to right).

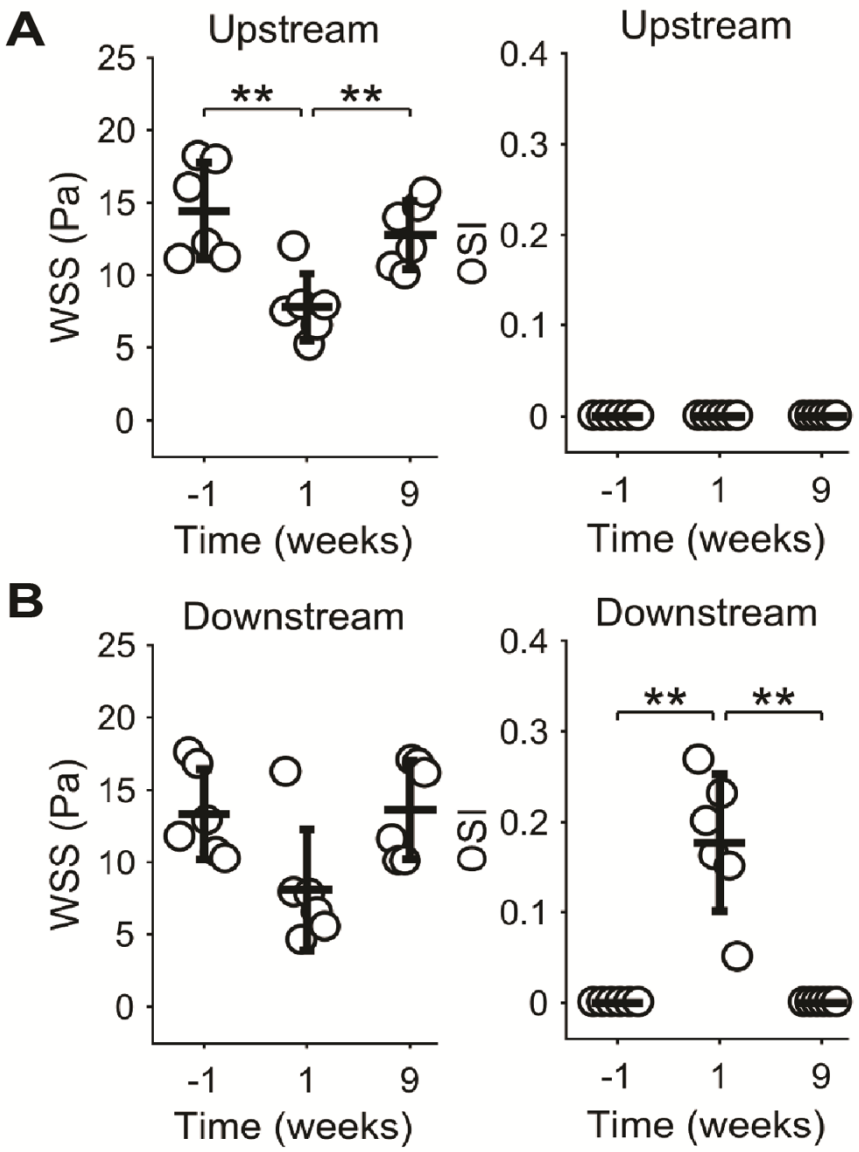

Figure 3.13. Wall shear stress (WSS) at peak systole and maximum oscillatory shear index (OSI) in the **(A)** unstable and **(B)** stable plaque regions (n=6 mice). Bars represent mean±SD. *Indicates statistically significant difference for given comparison, wherein $^{\#}p<0.1$, $*p<0.05$, $**p<0.01$, $***p<0.001$, and $****p<0.0001$. **See Table S3.4.**

3.5 DISCUSSION

Decades of research has established that the presence of disturbed blood flow within local arterial segments is a key aspect of the initiation and progression of atherosclerotic plaques in humans [27, 35, 65, 66, 100, 104-106] and animal models [1,

12, 25, 28, 39, 107, 108]. Yet, a complete understanding of the relationship between blood flow and atherosclerosis also requires evaluation of the effects of normal flow on plaque fate. Herein, we filled this knowledge gap by demonstrating for the first time a causal relationship between restoration of normal blood flow within atherosclerotic arteries and plaque stabilization. A blood flow-modifying cuff was used to induce atherosclerosis in an artery that would otherwise remain nondiseased, while later decuffing allowed blood flow to return to normal. MR imaging, Doppler ultrasound, and CFD confirmed that decuffing allows recovery of lumen area, blood velocity, and WSS to near baseline values. Despite some variability in these mechanical data over the rather short four-week therapeutic window employed in this study, we consistently observed that, compared to untreated mice (5U and 9U), plaques in the decuffed mice had higher collagen in both the unstable (+141% and +87%, respectively) and stable (+86% and +80%) regions, lower lipid (-52% and -75%) in the unstable region, and lower macrophages (-69% and -75%) in the unstable region. This dramatic modification in plaque composition indicates that even partial restoration of normal blood flow causes plaque stabilization.

It is remarkable that the degree of plaque stabilization in mice treated with restored normal blood flow was comparable to those treated with atorvastatin, given the well-documented efficacy of the latter as a first-line therapeutic for atherosclerosis in patients that reduces the 10-year incidence of heart attack by ~23% [109]. Another interesting parallel is that statins induce this beneficial effect primarily by promoting plaque stabilization. For example, the EASY-FIT (Effect of AtorvaStatin therapY on FIbrous cap Thickness in coronary atherosclerotic plaque) trial with 70 patients found a

significant increase in fibrous cap thickness (+69%), decrease in lipid arc (-27%), and decrease in macrophage grade (i.e., accumulation) (-38%) with 12 months of moderate atorvastatin therapy (20 mg/day) [110]. Similarly, another trial with 44 patients found a significant decrease in lipid-core burden index (-23%) with only 7 weeks of high-dose rosuvastatin (40 mg/day) [111]. Importantly, this study showed no change in plaque burden over this shorter timeframe. Although other clinical trials of statins over longer follow-up times (6 to 24 months) have shown decreases in plaque volume (typically, less than 10%) [112], these changes are more modest compared to changes in plaque composition. These results closely align with ours herein for restoration of normal blood flow. Interestingly, we also found that the combination of atorvastatin and restored normal blood flow induced an additive beneficial effect that not only caused further reductions in lipid and increases in collagen, but also caused a significantly lower plaque burden compared to the untreated mice at 9 weeks (-48%). This result indicates that the combined therapy promotes both plaque stabilization and regression. It also suggests that the therapeutic effects of statins and normal blood flow operate through different signaling pathways, which aligns with previous work demonstrating that statins and blood flow differentially regulate many endothelial genes [113, 114].

Although our study appears to be the first to directly consider the therapeutic effects of normal blood flow on atherosclerosis, previous studies provide indirect evidence of its beneficial effects. One clinical trial evaluating the association between disturbed flow and atherosclerosis in 374 patients demonstrated that, while the presence of low WSS in arterial segments at baseline was associated with decreased lumen area and increased plaque burden at 6 months follow-up, moderate and high WSS were

associated with increased lumen area and decreased plaque burden [35]. Another patient study showed similar results [27]. In addition, studies of exercise, which increases blood flow, have also shown beneficial effects on atherosclerosis [115]. Studies in ApoE$^{-/-}$ mice have demonstrated that exercise promotes the formation of more stable plaques compared to sedentary controls with similar compositional changes to those reported herein, including higher collagen content [116, 117]. In humans, it is well accepted that regular exercise reduces the risk of cardiovascular events, likely by promoting more stable atherosclerotic plaque phenotypes [118].

In conclusion, blood flow is a key regulator of the atherosclerotic state of an artery. It is well established that disturbed blood flow promotes plaque initiation and progression, while normal blood flow is protective. Herein, we demonstrated that restoring normal blood flow in atherosclerotic arteries is also therapeutic by promoting plaque stabilization. These findings motivate the development of novel therapeutic approaches that leverage the mechanosensitive nature of atherosclerosis, either through direct biomechanical modulation of the atherosclerotic artery or the administration of pharmaceuticals. Our results suggest that such a therapeutic could provide an additive beneficial effect when administered in parallel to traditional pharmacologic strategies such as statins.

3.6 Limitations of the study

There are five primary limitations of our study to consider addressing in future work. First, we only used female ApoE$^{-/-}$ mice. Because this study is the first to evaluate the therapeutic effects of a beneficial mechanical stimulus in the context of any vascular disease, we sought to minimize the potential of biological variables impacting our ability

to observe differences between the treated and untreated groups. However, previous work showed that the size and distribution of atherosclerotic plaques is similar between male and female ApoE$^{-/-}$ mice [11, 119], suggesting that plaques in male mice would respond similar to the treatment regimens used herein. Second, we assessed our therapeutics at an intermediate stage of plaque development. This approach limited growth of the plaques into the lumens of the arteries and their impact on blood flow because arteries undergo outward remodeling to compensate for plaque development (up to ~40% of plaque burden). This is a widely accepted phenomenon that was first shown in patients [120] and later animal models, including ApoE$^{-/-}$ mice [121]. Since plaques exist over a range of phenotypes that may influence their response to therapeutics, future work is needed to assess the effects of normal blood flow on more advanced plaques. Third, we applied our therapeutics over a relatively short timeframe of four weeks. Since the MRI data demonstrated improvement of lumen recovery over time, the beneficial effects stemming from restored normal blood flow were likely not established for that entire period. Nevertheless, we still observed highly significant improvements in plaque composition towards a more stable phenotype in mice treated with restored normal blood flow, suggesting that a longer timeframe of treatment would only lead to more dramatic improvements in these outcomes. Future work focusing on larger and more advanced plaque phenotypes should particularly consider longer time frames. Fourth, we did not consider curvature of the arteries in our CFD models due to a technical issue with the software (VMTK) used to detect the vessel centerline through the narrow lumen of the instrumented carotid artery in the cuff region (week 1) of decuffed mice. However, CFD simulations at the other time points were also run with curvature, which showed a

negligible effect compared to the straightened models. Future work seeking to evaluate local shear and histological features (versus the current approach of averaging over the whole vessel segments) may need to include this complexity. Fifth, we did not directly correlate shear metrics to histology. While many of the 9D (and 9U) mice used for histology were also imaged with MRI, Doppler ultrasound and CFD were performed late in the study with different mice (MRI was performed in these mice as well) for the sole purpose of supporting the MRI data in demonstrating that decuffing restores normal blood flow. However, directly correlating shear metrics to histological features may require a more sophisticated experimental approach. The MRI system used herein had an in-plane resolution of 90 μm and longitudinal resolution of 500 μm. While this was sufficient for determining the maximum stenosis of the arteries and relative differences over time in the shear metrics averaged over the whole upstream and downstream segments, higher spatial (and possibly temporal) resolution may be required to correlate features of the local shear environment to those of the local plaque environment. One could also consider additional complexities in the modeling approach, such as using fluid-structure interaction modeling for more realistic boundary conditions. Thus, there are many technical challenges to consider when performing such correlation analyses that warrant additional studies.

.

3.7 Supplemental Statistics Tables

Table S3.1. Results of all statistical comparisons for data in Figure 3.6 (histology of the unstable plaque region). In the case of multiple comparisons, p-values were corrected using the Holm-Bonferroni method.

A

	p-value
ANOVA	0.00069

	Comparison	Normality	Variance	Tails	p-value	Rank	Corr Factor	Adjusted p-value	Stars
1	5U v 9D	yes	equal	1	0.00807	5	5	0.04035	*
2	5U v 9A	yes	equal	1	0.06582	6	4	0.26328	-
3	5U v 9AD	yes	equal	1	0.00070	2	8	0.00560	**
4	9U v 9D	yes	unequal	1	0.00072	3	7	0.00507	**
5	9U v 9A	yes	unequal	1	0.00210	4	6	0.01258	*
6	9U v 9AD	yes	unequal	1	0.00047	1	9	0.00422	**
7	9D v 9A	yes	equal	2	0.46500	9	1	0.46500	-
8	9D v 9AD	yes	equal	1	0.35470	8	2	0.70939	-
9	9A v 9AD	yes	equal	1	0.12332	7	3	0.36997	-

B

	p-value
ANOVA	0.00013

	Comparison	Normality	Variance	Tails	p-value	Rank	Corr Factor	Adjusted p-value	Stars
1	5U v 9D	yes	equal	1	0.00002	1	9	0.00020	***
2	5U v 9A	yes	equal	1	0.00265	4	6	0.01588	*
3	5U v 9AD	yes	equal	1	0.09246	6	4	0.36986	-
4	9U v 9D	yes	unequal	1	0.00016	2	8	0.00130	**
5	9U v 9A	yes	equal	1	0.00225	3	7	0.01576	*
6	9U v 9AD	yes	equal	1	0.01680	5	5	0.08399	-
7	9D v 9A	yes	equal	2	0.34600	7	3	1.00000	-
8	9D v 9AD	yes	equal	1	0.90753	9	1	0.90753	-
9	9A v 9AD	yes	equal	1	0.72180	8	2	1.00000	-

C

	p-value
ANOVA	0.000012

	Comparison	Normality	Variance	Tails	p-value	Rank	Corr Factor	Adjusted p-value	Stars
1	5U v 9D	yes	equal	1	0.00053	3	7	0.00372	**
2	5U v 9A	yes	unequal	1	0.02983	7	3	0.08949	#
3	5U v 9AD	yes	equal	1	0.00000	1	9	0.00003	****
4	9U v 9D	yes	equal	1	0.00088	4	6	0.00528	**
5	9U v 9A	yes	unequal	1	0.06858	8	2	0.13715	-
6	9U v 9AD	yes	unequal	1	0.00002	2	8	0.00015	***
7	9D v 9A	yes	equal	2	0.64338	9	1	0.64338	-
8	9D v 9AD	yes	equal	1	0.00159	5	5	0.00793	**
9	9A v 9AD	yes	equal	1	0.00309	6	4	0.01236	*

Table S3.2. Results of all statistical comparisons for data in Figure 3.7 (histology of the stable plaque region). In the case of multiple comparisons, p-values were corrected using the Holm-Bonferroni method.

A

	p-value
KW	0.054

	Comparison	Normality	Variance	Tails	p-value	Rank	Corr Factor	Adjusted p-value	Stars
1	5U v 9D	no	equal	1	0.46329	8	2	0.92659	-
2	5U v 9A	no	equal	1	0.41210	7	3	1.00000	-
3	5U v 9AD	no	unequal	1	0.00805	1	9	0.07243	#
4	9U v 9D	yes	equal	1	0.17765	5	5	0.88825	-
5	9U v 9A	no	equal	1	0.29573	6	4	1.00000	-
6	9U v 9AD	yes	unequal	1	0.00880	2	8	0.07038	#
7	9D v 9A	no	equal	2	0.85633	9	1	0.85633	-
8	9D v 9AD	yes	unequal	1	0.01013	3	7	0.07088	#
9	9A v 9AD	no	unequal	1	0.02457	4	6	0.14742	-

B

	p-value
KW	0.064

	Comparison	Normality	Variance	Tails	p-value	Rank	Corr Factor	Adjusted p-value	Stars
1	5U v 9D	yes	equal	1	0.05600	4	6	0.33600	-
2	5U v 9A	no	equal	1	0.18300	7	3	0.54900	-
3	5U v 9AD	no	equal	1	0.01400	2	8	0.11200	-
4	9U v 9D	yes	equal	1	0.04700	3	7	0.32900	-
5	9U v 9A	no	equal	1	0.06200	5	5	0.31000	-
6	9U v 9AD	no	equal	1	0.00890	1	9	0.08010	#
7	9D v 9A	no	equal	2	0.96629	9	1	0.96629	-
8	9D v 9AD	no	equal	1	0.23500	8	2	0.47000	-
9	9A v 9AD	no	equal	1	0.16600	6	4	0.66400	-

C

	p-value
ANOVA	0.000054

	Comparison	Normality	Variance	Tails	p-value	Rank	Corr Factor	Adjusted p-value	Stars
1	5U v 9D	yes	equal	1	0.00240	3	7	0.01680	*
2	5U v 9A	yes	unequal	1	0.02209	7	3	0.06627	#
3	5U v 9AD	yes	equal	1	0.00001	2	8	0.00007	****
4	9U v 9D	yes	equal	1	0.00326	4	6	0.01956	*
5	9U v 9A	yes	equal	1	0.00769	6	4	0.03077	*
6	9U v 9AD	yes	equal	1	0.00000	1	9	0.00003	****
7	9D v 9A	yes	equal	2	0.55043	9	1	0.55043	-
8	9D v 9AD	yes	equal	1	0.00690	5	5	0.03450	*
9	9A v 9AD	yes	equal	1	0.11652	8	2	0.23303	-

Table S3.3. Results of all statistical comparisons for data in Figure 3.8 C&D (plaque burden). In the case of multiple comparisons, p-values were corrected using the Holm-Bonferroni method.

A

	p-value
ANOVA	0.038

	Comparison	Normality	Variance	Tails	p-value	Rank	Corr Factor	Adjusted p-value	Stars
1	5U v 9D	yes	equal	1	0.33454	7	3	1.00000	-
2	5U v 9A	yes	equal	1	0.82908	9	1	0.82908	-
3	5U v 9AD	yes	equal	1	0.08698	3	7	0.60883	-
4	9U v 9D	yes	equal	1	0.01630	2	8	0.13036	-
5	9U v 9A	yes	equal	1	0.19625	5	5	0.98125	-
6	9U v 9AD	yes	equal	1	0.00228	1	9	0.02051	*
7	9D v 9A	yes	equal	2	0.29930	6	4	1.00000	-
8	9D v 9AD	yes	equal	1	0.42623	8	2	0.85246	-
9	9A v 9AD	yes	equal	1	0.09298	4	6	0.55786	-

B

	p-value
ANOVA	0.035

	Comparison	Normality	Variance	Tails	p-value	Rank	Corr Factor	Adjusted p-value	Stars
1	5U v 9D	yes	equal	1	0.52810	7	3	1.00000	-
2	5U v 9A	yes	equal	1	0.54892	8	2	1.00000	-
3	5U v 9AD	yes	equal	1	0.05885	4	6	0.35309	-
4	9U v 9D	yes	equal	1	0.10035	6	4	0.40140	-
5	9U v 9A	yes	equal	1	0.09708	5	5	0.48541	-
6	9U v 9AD	yes	equal	1	0.00082	1	9	0.00737	**
7	9D v 9A	yes	equal	2	0.96177	9	1	0.96177	-
8	9D v 9AD	yes	equal	1	0.05585	3	7	0.39097	-
9	9A v 9AD	yes	equal	1	0.03435	2	8	0.27479	-

Table S3.4. Results of all statistical comparisons for data in Figure 3.9-3.13 (imaging and modeling of 9D mice). In the case of multiple comparisons, p-values were corrected using the Holm-Bonferroni method.

Figure 3.9

	Comparison	Normality	Variance	Tails	p-value	Rank	Corr Factor	Adjusted p-value	Stars
1	Week 1	yes	unequal	1	0.00000	2	3	0.00000	****
2	Week 4	yes	unequal	1	0.00000	1	4	0.00000	****
3	Week 7	no	equal	2	0.00200	3	2	0.00400	**
4	Week 9	yes	equal	2	0.06700	4	1	0.06700	-

Figure 3.10

	Comparison	Normality	Variance	Tails	p-value	Rank	Corr Factor	Adjusted p-value	Stars
1	Week 1	yes	equal	2	0.35900	3	2	0.71800	-
2	Week 4	yes	unequal	2	0.70900	4	1	0.70900	-
3	Week 7	yes	unequal	2	0.00000	2	3	0.00000	****
4	Week 9	yes	equal	2	0.00000	1	4	0.00000	****

Figure 3.11

	Comparison	Normality	Variance	Tails	p-value	Rank	Corr Factor	Adjusted p-value	Stars
1	Week 1	yes	equal	1	0.00000	1	4	0.00002	****
2	Week 4	yes	equal	1	0.00001	2	3	0.00002	****
3	Week 7	yes	equal	2	0.17900	3	2	0.35800	-
4	Week 9	yes	equal	2	0.30500	4	1	0.30500	-

Figure 3.13

	p-value
RM ANOVA	0.00300

	Comparison	Normality	Variance	Tails	p-value	Rank	Corr Factor	Adjusted p-value	Stars
1	-1 vs 1	yes	equal	1	0.00296	1	3	0.00888	**
2	-1 vs 9	yes	equal	2	0.37100	3	1	0.37100	-
3	1 vs 9	yes	equal	1	0.00430	2	2	0.00860	**

OSI-Up	**p-value**
Friedman	0.51300

WSS-Down	**p-value**
Friedman	0.13500

OSI-Down	**p-value**
RM ANOVA	0.0002

	Comparison	Normality	Variance	Tails	p-value	Rank	Corr Factor	Adjusted p-value	Stars
1	-1 vs 1	yes	Unequal	1	0.00114	1	3	0.00342	**
2	-1 vs 9	yes	Unequal	2	0.69100	3	1	0.69100	-
3	1 vs 9	yes	Unequal	1	0.00114	1	3	0.00342	**

CHAPTER 4

Developing a Microfluidics System to Examine Physiologic Flow Over Endothelial Cells

Data will be submitted with LIPUS study

4.1 Abstract

This chapter focuses on the methodology behind designing and implementing a reliable and relevant microfluidics system. While the system components were commercially available, we needed specific aspects of the system for promoting a more physiological relevant flow profile over longer times. Therefore, this chapter focuses on the troubleshooting progression of optimizing a microfluidics system. This experiment is the next step in examining the flow environment as a therapy for atherosclerosis. In this preliminary study, endothelial cells were placed under orbital, continuous, and pulsatile flow at a moderate and high shear stress. Endothelial cells sense the blood flow environment, thus, by stimulating endothelial cells with different flow types and different shear stresses, we can identify the most beneficial flow and shear stress for improving endothelial cell health. All flow environments proved to be beneficial compared to static conditions, however, orbital had the highest improvement in atheroprotective and atherogenic gene expression. This preliminary study demonstrated that microfluidics can be utilized to examine endothelial cell behavior in an anatomically relevant geometry and used to quantify how different flow types will change endothelial cell gene expression over a range of wall shear stresses.

4.2 Introduction

Since endothelial cells at the blood interface sense shear stress from blood flow on the vessel wall that causes a cascade of cell signaling, this preliminary study

investigated the development of a microfluidics platform to characterize the response of endothelial cells to different flow conditions with different shear stresses. Wall shear stress has been shown to be the most important mechanical stimulus due to blood flow on the endothelium. In particular, high shear stress levels (>2.0 Pa) regulate endothelial cells' homeostasis by suppressing inflammation, migration, and adhesion of leukocytes, thereby causing atheroprotective effects. Additionally, moderate shear stress (1.3-1.5 Pa) is considered normal in the vasculature. Finally, low shear stress (<0.5 Pa) has been shown to induce atherogenic effects.

Herein we designed, tested, and implemented an innovative microfluidics device capable of inducing this range of shear stresses onto isolated endothelial cells. Designing and then troubleshooting this flow system led to a stronger understanding of each component and how it regulated desired outcomes. This preliminary study focused on creating a more physiologically relevant flow profile by utilizing microfluidics. We took advantage of commercially available flow products from Elveflow, Darwin, and Ibidi. This allowed for less discrepancies between experiments by maintaining constant experimental parameters, like shear stress, as well as microchannel area, geometry, and material.

Once the microchannels were purchased, the flowrates for the desired shear stresses were calculated and the electrical components (pressure controller, flow sensor, and recirculator) of the system were optimized. We then began attempting cellular experiments to examine the biological response to a range of wall shear stresses under different flow types. We utilized a custom dynamic flow profile option through the Elveflow microfluidics system. In this preliminary study, this system was used to

demonstrate the mechanobiological response of human umbilical vein endothelial cells (HUVECs) by examining three atheroprotective and three atherogenic markers under different flow conditions. We examined both continuous flow at moderate (1.36 Pa) and high (1.88 Pa) WSS, and pulsatile flow at moderate (0.37-3.89 Pa with an average of 1.12 Pa) and higher (0.37-4.99 Pa with an average of 1.36 Pa) WSS. We also used a less physiologic flow type, orbital flow, as a comparator to further evaluate the importance of physiologic flow in determining the biological response. For these experiments, we examined different orbital velocities at similar wall shear stresses to those used in our microfluidics experiments, including: 250 (0.8-1.89 with an average of 1.36 Pa) and 350 (1-2.97 Pa with an average of 1.88 Pa) RPM. Future studies will examine a range of WSS over these different flow types to create a mechanical dose response curve on different microfluidics substrates. This would provide understanding of the most optimal flow type and shear stress that improves endothelial cell health in a more physiologically relevant flow environment.

4.3 Methods

4.3.1 Flow System

The experimental setup consisted of an air compressor, a pressure controller, a flow sensor, a MUX recirculation valve, a microfluidic system with two independent channels, connecting tubing, and two large reservoirs for recirculation of cell culture media. The channels and reservoirs were placed inside an incubator (37°C, 4% CO_2) and connected to the pressure controller, recirculation valve, flow sensor and air compressor on the outside of the incubator (Figure 4.1). This did make sterility more difficult due to the complexity with tubing and connection between the sterile and exterior environments, however, our system was compatible with ethanol, so contamination was typically

avoided. We did not have issue with bubbles generating within the tubing due to the system being closed, thus a bubble trap was unnecessary.

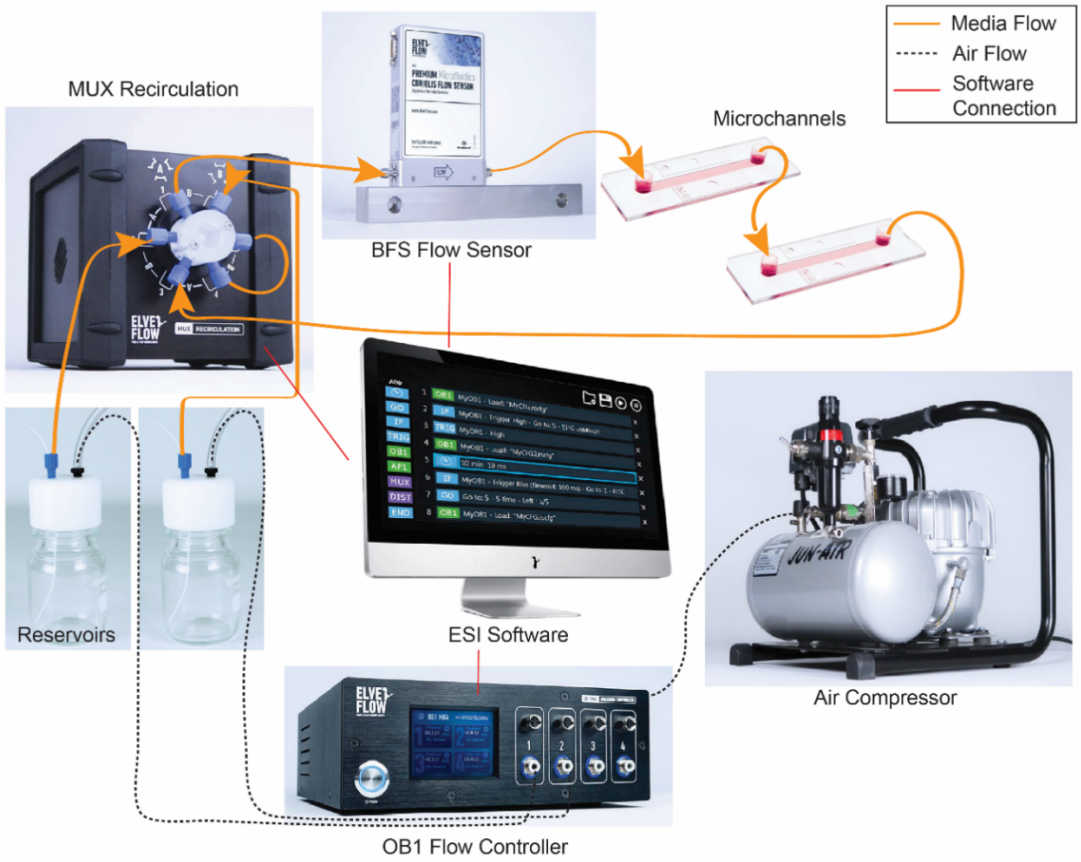

Figure 4.1. Pressure based microfluidics set up for recirculation of flow. (Elveflow, Ibidi, and Darwin products)

4.3.2 Pressure controller troubleshooting and optimization

Commercially available pressure controller, OB1, combined with an air compressor was used to drive cell culture medium through the system. This component utilized piezoelectric regulators to improve faster flow control than other pressure controllers on the market. This was important for our experimental set up, especially for pulsatile flow, because we needed a fast response for recirculation between pressure channels, and to reach systole and diastole peaks over a cardiac cycle.

The challenge with this component was realizing that the two pressure channels for each reservoir required different pressures for promoting the same flow rate. This was not an issue for shorter experiments, but the differences in pressure drops made the system more complex when running 48-hour experiments. To troubleshoot this issue, the system was turned on for an extended period of time to ensure that the system was warmed up and reached homeostasis. Since we had a more unique setup, the larger reservoirs required the OBI1 pressure controller to be calibrated with appropriate PID loop flow regulation values. Thus, the OBI1 controller was optimized before each experiment by auto-tuning each pressure channel based on the gain, integration time parameters, and max flowrate value. To understand this aspect of the pressure controller, I had to evaluate the PID types. Elveflow had a special algorithm that simplified the flow control for larger reservoirs, therefore response and stability PID values were updated automatically (Figure 4.2). To utilize this algorithm, pressure values were set to 0 and the control mode settings were clicked on. Once the feedback tab was selected, the Auto Tune was enabled, and system was calibrated for larger reservoirs.

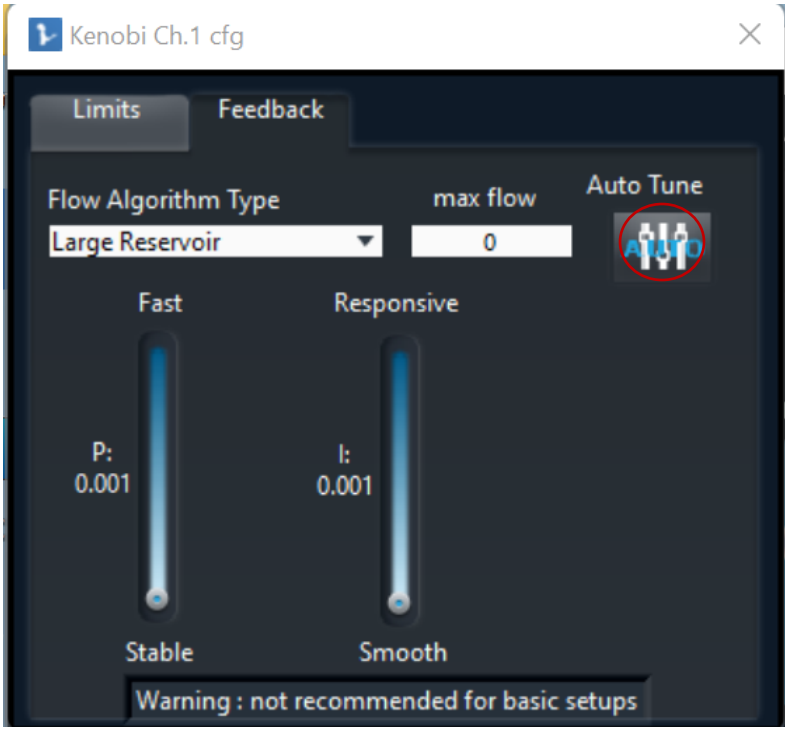

Figure 4.2. PID calibration for each pressure channel.

Additionally, each flow rate was first tested based on the flow regulator option of the flow controller (Figure 4.3). That way, the approximate pressure for each channel could be determined separately based on the desired flowrate. The system had to be maintained by the pressure regulator due to the flowrate sensor not adjusting to the higher flowrates as efficiently. This promoted more stability between the two pressure channels. Furthermore, since the BFS flow sensor was not created by Elveflow, it was difficult to connect both pressure channels to one flow sensor.

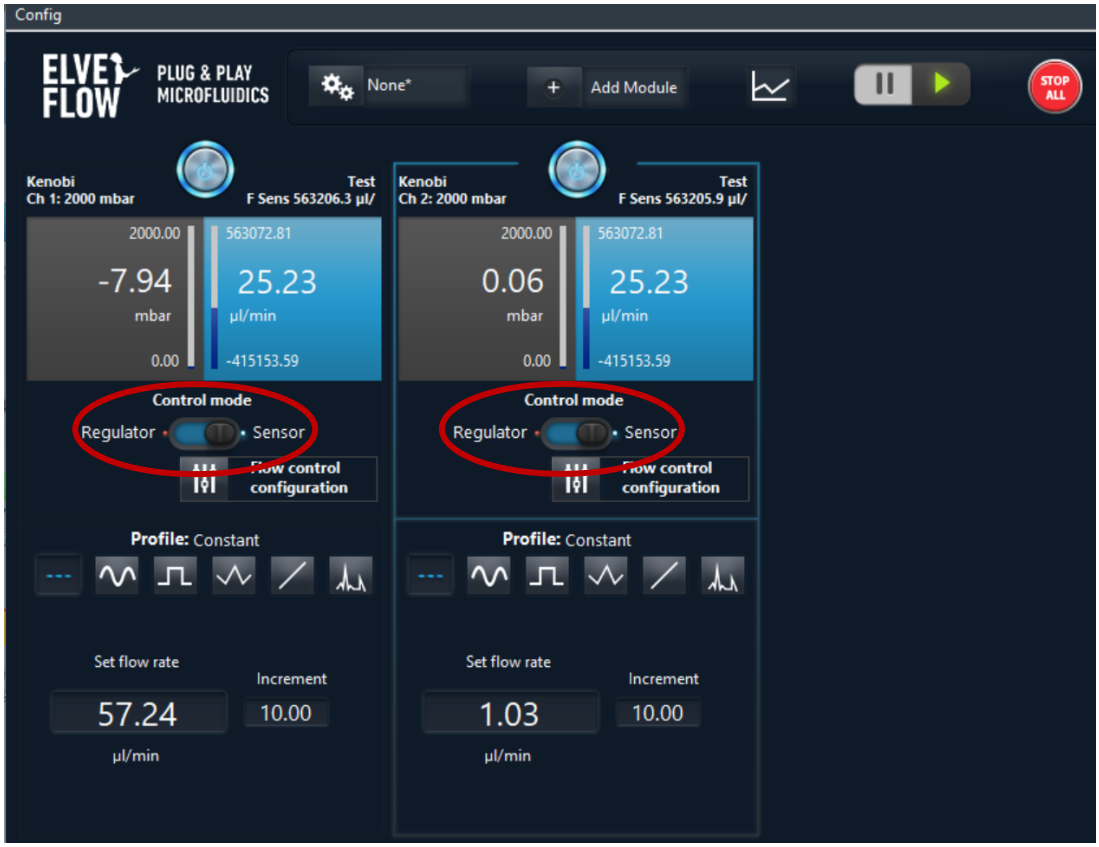

Figure 4.3. The system can be run based on flowrate or pressure. This displays the system as a flow regulator to make sure the chosen pressures were correct.

4.3.3 Flow sensor troubleshooting

The flow rate was controlled by a Bronkhorst Flow Sensor allowing for easy calculations between shear stress and flow rate. The desired flowrate was inputted into the ESI software that controlled all instruments. The desired flow rate was calculated from the viscosity of media at 37°C [122] and desired shear stress using Equation 4.1.

$$\text{Eqn. (4.1)} \qquad \tau = \frac{6\mu Q}{WH^2},$$

$$where \quad \mu = viscosity, \;\; Q = flowrate, \;\; W = channel\ width, \;\; H = channel\ height$$

This instrumental component of the system was necessary to make sure the desired shear stress was being reached. This flow sensor was chosen based on its high accuracy, fast

response, and extremely wide flow rate range. However, installation of this component was more complicated. This flow sensor typically is used for harder stainless-steel tubing and fittings, however, in our experiments we required soft tubing so the cellular aspects could remain within the incubator, and the electrical components could remain outside the incubator. Thus, the flow sensor had to be manually engineered for softer tubing and maintain a closed pressure-based system. The flow sensor was provided with soft red ferrules that were to act as a replacement for the metal components, however, these ferrules had too small of a diameter and ended up constricting the soft tubing and stopping flow from entering the flow sensor. Therefore, to replace the metal and provided ferrules, plumber tape was implemented to create a looser ferrule to allow for flow, but also to ensure the tubing was airtight within the metal luer locks. This so far has been the best method for experiment repeatability, long term stability, and no leakage.

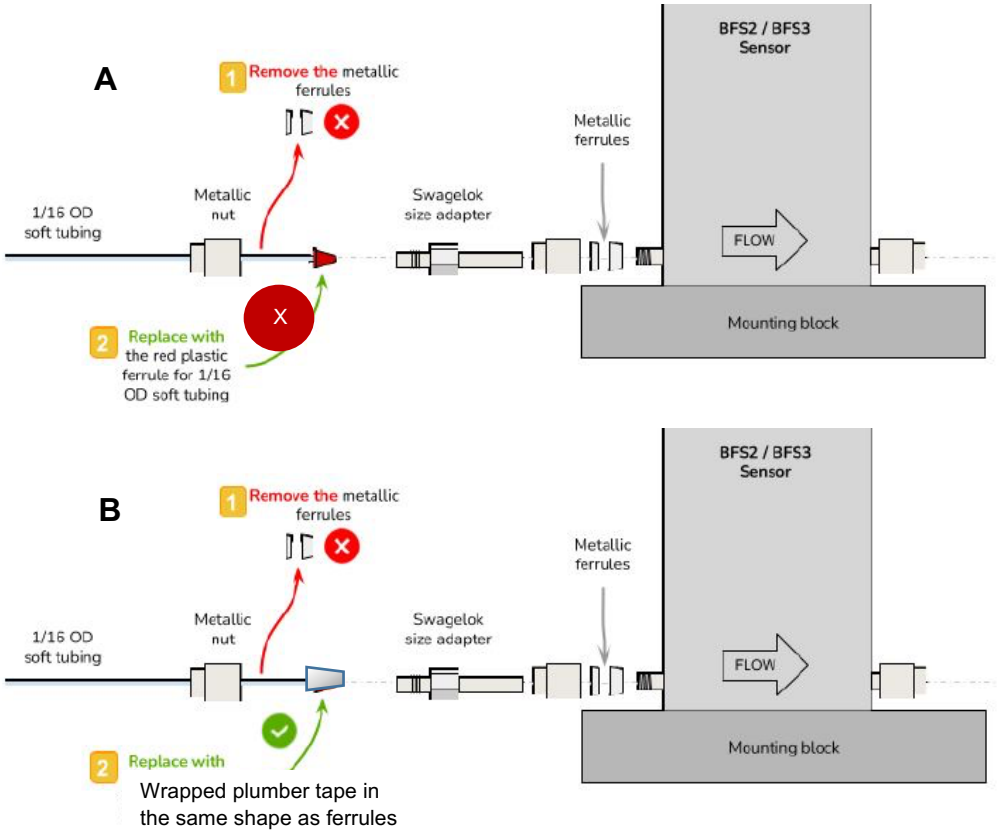

Figure 4.4. Troubleshooting the BFS flow sensor for maintaining flow with no leakage. (A) What the Elveflow instruction manuals suggest. (B) The solution to the flow sensors unique design.

4.3.4 Recirculation requirement

This set up allowed for recirculation of media for over 24 hours. The MUX recirculator was a requirement for our longer experimental times. The system needed to be run for 48 hours, therefore recirculation between two reservoirs was required. This component had its own challenges in understanding the two media flow positions. The soft tubing needed to be implemented in a specific way to ensure that media was flowing in the correct direction even when the MUX recirculator transitioned from position 1 to position 2 (Figure 4.5). This was done by trial and error and utilizing the Elveflow graphics for understanding how the different positions were implemented. Figures 4.1 and 4.5 demonstrate how the soft tubing needs to be attached in order for our system to run for long periods of time in the correct flow direction.

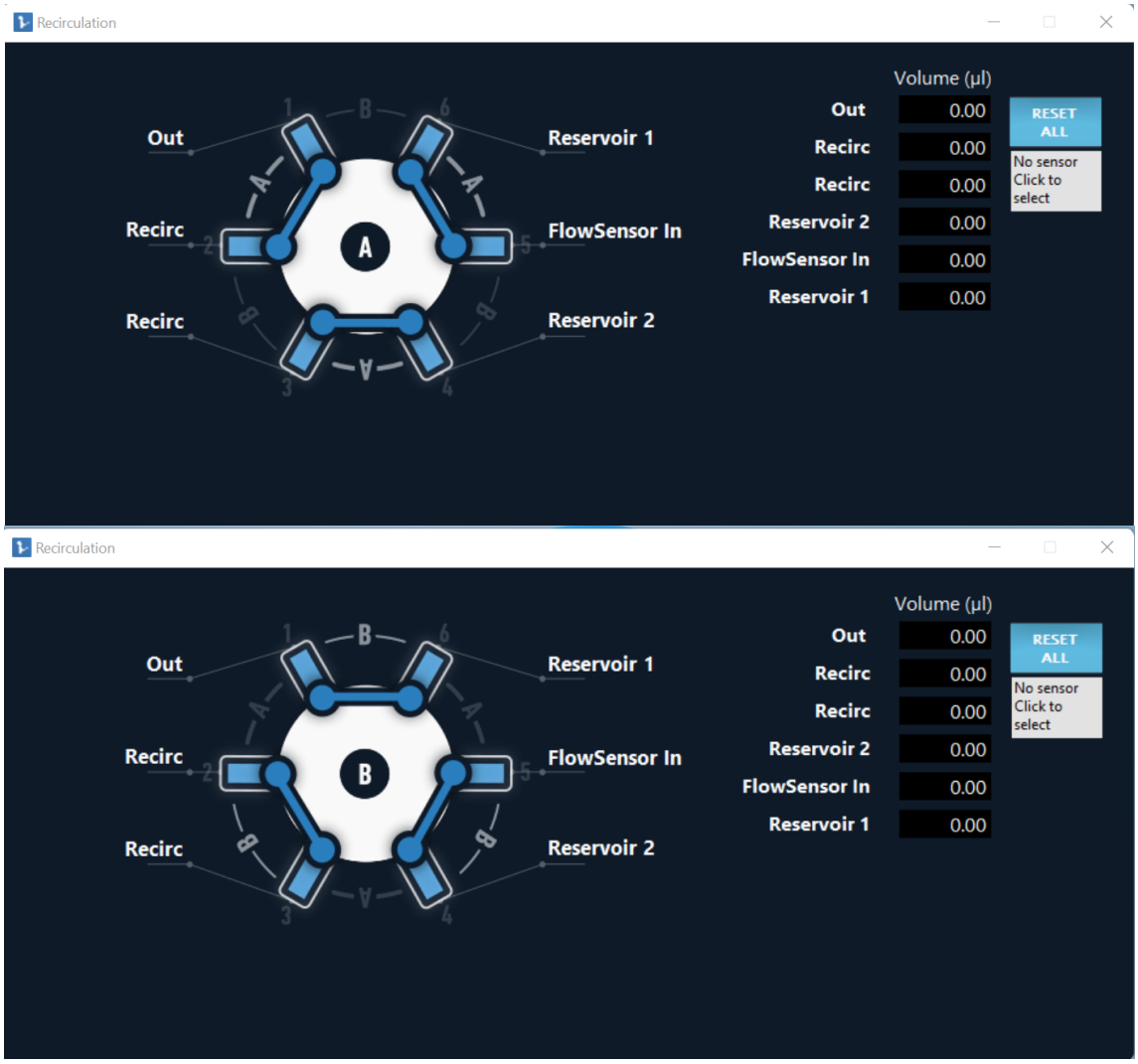

Figure 4.5. Displays the two recirculation configurations based on the flow direction and which reservoir is being pressurized. Position A is for reservoir 1 and OBI1 channel 1 (top), position B is for reservoir 2 and OBI1 channel 2 (bottom).

4.3.5 Implementing commercially available microfluidics channels

Commercially available glass microfluidic channels (Ibidi u-Slide I Luer Glass Bottom), and glass 6 well plates were used for culturing cells under different flow conditions. Static controls were seeded at the same density in plastic 12 well plates. The glass microchannels were tested in series and parallel arrangements to determine which would allow for the same flowrates between channels. The series tests were shown to be most effective, demonstrating that the channels were achieving similar flowrates and

results. Parallel flow was not as effective, most likely due to doubling the total flowrate to maintaining the desired flowrate in each of the channels.

At first, glass channels were chosen to create the same conditions as the orbital shaker glass well plates, however, this became problematic due to the microfluidics system remaining closed and pressure based. Glass does not allow gas exchange and did not show promising cell health compared to normal well plates. This will be adjusted in future studies by using polymer channels that allow for gas exchange.

4.3.6 Experimental set up

As a preliminary test of our system, flow experiments were performed using two different flow conditions, continuous and pulsatile, at two different shear stress levels, moderate and high. Experiments were run in series, allowing multiple channels to be used at once. Continuous and pulsatile flow conditions were monitored by the flow sensor readings (Figure 4.6). As an additional flow condition, we evaluated the response of cells under orbital flow at two different RPMs (250 and 350) and the same shear stress levels.

Figure 4.6. Side by side views for pulsatile flow versus continuous flow. Pressure channel 1 is implemented with pulsatile flow (left) and pressure channel 2 is implemented with continuous flow (right).

Continuous flow experiments were performed at 1.36 Pa and 1.88 Pa. Pulsatile flow patterns were completed for moderate shear stress at an average over the "cardiac cycle" of 1.12 Pa and a higher shear stress at 1.36 Pa, the latter of which contained the systole maximum shear stress (5 Pa) that could be achieved with this system. Pulsatile flow profiles were generated by importing basic flow rate curves of human systole and diastole cardiac movements from Onaizah *et al* then averaged to utilize desired shear stress (Figure 4.7) [123]. For the moderate profile, systole reached a shear stress peak magnitude of 3.89 Pa and diastole had a shear stress peak magnitude of 0.37 Pa. The high shear stress profile had a systole shear stress peak magnitude of 4.99 Pa and diastole had a shear stress peak magnitude of 0.37 Pa. Each pulsatile wave function was run at 60

beats per minute to mimic the anatomical environment. The orbital shaker had two shear stresses, 250 and 350 RPM, that were averaged over the periphery area of the well plate at 1.36 Pa, ranging from 0.8 to 1.89 Pa, and 1.88 Pa, ranging from 1 to 2.97 Pa, respectively.

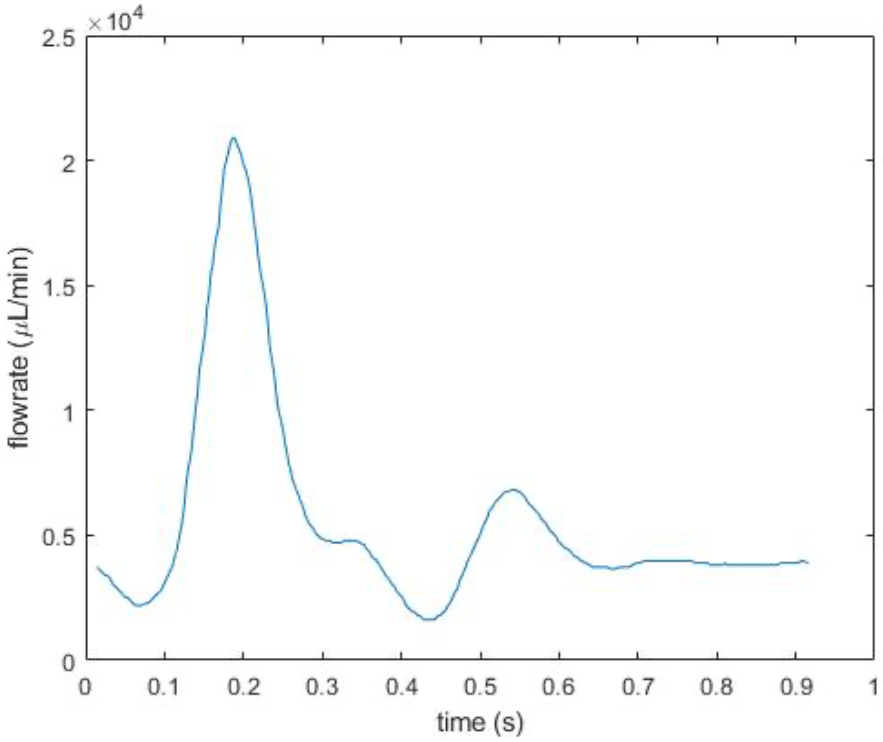

Figure 4.7. Pulsatile wave form imported into ESI software to generate systole and diastole relevant flow profile.

4.3.7 Creating a scheduler to maintain continuous flow for 48 hours

To maintain continuous media flow through the microfluidics system, the ESI software allows for the development of a scheduler. The scheduler controls each component of the system in a specific configuration to determine which pressure channel, recirculation valve position, reservoir, and flow profiles are being activated. Once the pressure controller, recirculation valve and flow sensor were calibrated, each component was set for a specific shear stress and the configuration of all components in a specific

orientation were saved. To create this synchronized scheduler, each configuration for each orientation and shear stress must be saved in the main ESI software, then dragged or placed into the scheduler application (Figure 4.8).

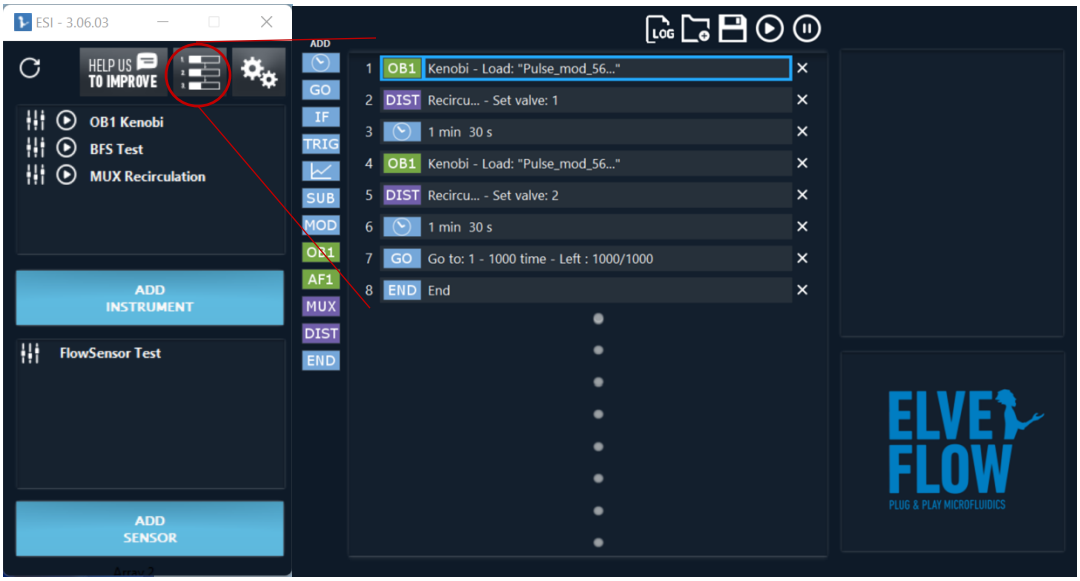

Figure 4.8. Implementing the scheduler for continuous media flow in a single flow direction.

4.3.8 Cell culture

HUVECs pooled from 10 donors were used for experiments from passages 4 to 6. Cells were maintained with vascular cell basal medium, containing endothelial cell growth kit-BBE and 0.1% Penicillin-Streptomycin-Amphotericin B Solution within a humidified incubator. Glass bottom micro-channels and well plates were coated with rat tail type I collagen and then seeded with cells at a density of 60,000 cells/cm^2 as per the distributor's instructions. Experiments were run one day after seeding with 200 µl of media syringed into each micro channel, and 2.41 ml of media pipetted per well. In each experiment, cells were either subjected to flow, or maintained under static conditions for 48 hours.

4.3.9 RT-qPCR

The gene expression for atheroprotective and atherogenic endothelial markers were evaluated using RT-qPCR. The atheroprotective genes were eNOS, KLF-2, and THBD and the atherogenic markers were ET-1, CTGF, and CAV-1. At the end of each experiment, total RNA was obtained from the cell layers. RNA was isolated using an RNeasy Micro kit. MRNA quality was assessed by measuring the 260/280 absorbance with a Take3 plate on a Cytation 5 plate reader (Biotek). Ratios between 1.8 and 2.1 were considered acceptable purity. Reverse transcription (RT) was done with an iScript kit converting the total RNA with a MiniAmp Thermal Cycler. Primers were designed and efficiencies tested with loading conditions from 500 pg/µl to 500 fg/µl in triplicate with SsoAdvanced Universal SYBR Green Supermix using QuantStudio 3 Real-Time PCR System. To be rigorous, triplicates that had standard deviations greater than 0.2 were examined and a triplicate was removed if it was determined to be an outlier.

Data was then analyzed with the delta-delta CT method. This approach computed the amount of gene expression by normalizing to a house keeping gene (HPRT-1) and then computing this value relative to the average across multiple static control cell layers. Each control was averaged over the moderate and high shear stress conditions for each flow type. The final value is then taken as $2^{-\Delta\Delta CT}$ to express the fold changes in gene expression.

4.4 Results

4.4.1 Flow type promotes different atherosclerosis gene expression

RT-qPCR was used to characterize the expression of atheroprotective and athoergenic genes. The expression of each gene was normalized by a housekeeping gene

(HPRT-1) and reported relative to averaged static controls. As stated, endothelial cell health is dependent on the flow environment and the amount of shear stress applied. Gene expression was evaluated on cell layers under continuous, pulsatile, and orbital flow with moderate and high shear stresses. While maintaining similar trends, preliminary results demonstrated that the different flow types had an effect on gene expression, however moderate and high shear did not seem to affect the gene expression as much as expected. Interestingly, orbital flow had the highest atheroprotective gene expression for KLF-2, eNOS, and THBD, and the lowest atherogenic gene expression for ET-1, CTGF, and CAV1, demonstrating it had the most beneficial effect on atherosclerotic gene expression (Figure 4.9D). Furthermore, between 250 and 350 RMP, the fold change was the same for atheroprotective and atherogenic genes (Figure 4.9D) with no significant differences between the two shear stresses. Continuous flow at moderate and high shear stress had nearly identical atheroprotective and atherogenic gene expression with no significant differences (Figure 4.9A). Continuous flow did not show upregulation of THBD and did not downregulate the atherogenic genes as well as the orbital shaker. However, it did show upregulation of eNOS and KLF-2. Pulsatile flow had similar fold change between the two WSS with slight increases in atheroprotective gene and small decreases in atherogenic gene at the high WSS (Figure 4.9B). When comparing continuous flow versus pulsatile flow at the moderate shear stress, atheroprotective gene expression was higher in the pulsatile flow even when the average shear stress rate was the same (Figure 4.9C). Interestingly, even though the average WSS was 1.36 Pa for both the continuous and pulsatile flow, continuous flow had a more beneficial biological response. Orbital

flow demonstrated the most beneficial effect on endothelial cells with atheroprotetive markers upregulated and atherogenic marker downregulated.

Improvements still need to be made to the microfluidics system in order to promote similar levels of cell health. Currently, the microfluidics systems does not have as optimal gas exchanged compared to the orbital shaker, thus the data is not demonstrating the optimal atheroprotective response with the current glass slides and pressurized close system. Thus, improvements need to be made to the choice of microchannels that allow for gas exchange between the cells and the incubator environment.

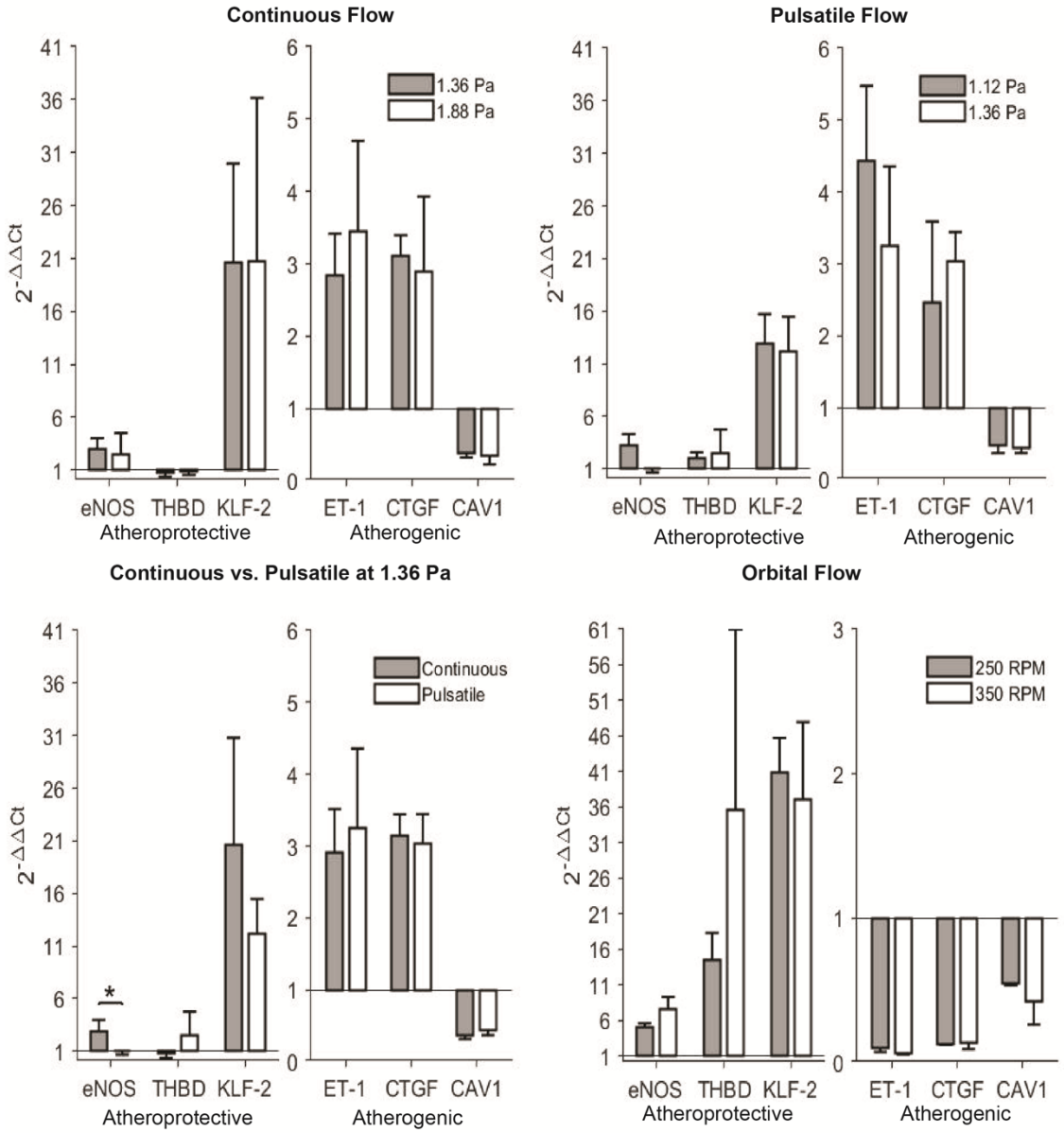

Figure 4.9. Atheroprotective and Atherogenic gene expression of the different flow environments at moderate and high shear stresses. (A) Moderate (1.36 Pa) and high (1.88 Pa) shear stress with continuous flow. (B) Moderate WSS (average WSS of 1.12 Pa) and high (average WSS of 1.36 Pa) shear stress with pulsatile flow. (C) Continuous flow vs Pulsatile flow at 1.36 Pa. (D) 250 (average WSS of 1.36 Pa) and 350 (average WSS of 1.88 Pa) RPM orbital flow.

4.5 Conclusion

It has been shown that endothelial cells under flow are healthy, however, no study has quantified multiple flow types at differing shear stresses to examine which flow and shear stress combination is the most beneficial. These findings demonstrate the endothelium's high sensitivity to changes in wall shear stress and flow. Many studies in

atherosclerosis have demonstrated strong associations between different plaque types and WSS conditions, including WSS magnitude and direction [105]. Despite these strong correlations, there still needs to be a better understanding of these relationships to further develop reliable indicators of plaque progression. Current studies lack in correlating the flow and WSS environment when designing their experimental set up. Typically, *in vitro* flow experiments pick a common flow type, WSS metric, and value as an afterthought, without truly understanding why. In this preliminary study, these WSS conditions demonstrated a causal relationship between WSS, flow, and disease progression. By designing and implementing a more relevant flow profile utilizing microfluidics, we can examine different flow profiles with different shear stresses. Creating a reliable methodology for this system is extremely important because, while the trends are the same between flow types seen in our preliminary results and current literature, there is clearly a difference in gene expression. Thus, quantifying endothelial cell behaviors over different flow types and a range of WSS conditions are important in improving the predictive tools to treat atherosclerosis.

CHAPTER 5

Future Direction

5.1 Conclusion

There have been many advances in the understanding of atherosclerosis within the last decade. Important clinical advances and therapeutic approaches have introduced many new avenues for researching this disease. However, despite the great progress, there are still many challenges moving forward. This dissertation emphasizes the recent developments of how atherosclerosis initiates, progresses, and finally, how it can be treated by examining the blood flow environment. The work presented in this dissertation can be extended in various ways to improve atherosclerosis patient outcomes.

Each chapter contains an important step forward in finding new therapies for atherosclerosis. In Chapter 2 we hypothesized that different blood flow profiles such as low and multidirectional flow, promoted differential nanoparticle uptake. However, what we found was that disturbed blood flow impacted nanoparticle accumulation in an indirect way by promoting different plaque phenotypes. These different phenotypes demonstrated different nanoparticle uptake based on the plaque composition. In the low flow region where unstable plaques are promoted with high lipid content, smooth muscle cells distributed near the lumen interface, and low collagen content, we found that nanoparticle accumulation was decreased from an intermediate plaque stage to a more advanced plaque stage. Multidirectional flow which promoted more stable plaques that have high lipid content, plaque burden, and smooth muscle cells distributed throughout the plaque, saw similar nanoparticle accumulation over time. Our findings suggest that nanoparticle accumulation was most influenced by the distribution and type of smooth

muscle cells within the different plaque phenotypes. The low flow region promoted a more synthetic smooth muscle cell caused by migration toward the lumen interface which inhibited nanoparticle uptake, and the multidirectional region contained more contractile smooth muscle cells allowing for nanoparticle diffusion into the plaque. The finding of differential accumulation of nanoparticles in different plaque phenotypes suggests that nanoparticles may be able to be used as a noninvasive diagnostic of plaque phenotype, including identifying the most advanced plaques that are vulnerable to rupture.

It has been established that disturbed blood flow is a primary reason for atherosclerosis initiation and progression. However, no study has examined the affect of restored normal blood flow on plaque fate. Chapter 3 was a proof-of-concept study that demonstrated that unstable and stable plaques caused by low and/or multidirectional blood flow, can be treated by restoring normal (laminar) flow. We found that normal flow promoted significant plaque stabilization with an efficacy comparable to treatment with atorvastatin. Specifically, both therapies showed a decrease in lipid and macrophages, and an increase in collagen. When the two treatment groups were combined, we found they had an additive therapeutic effect, including further improved plaque stability and reduced plaque size that indicated regression. These findings suggest that mechanical stimuli can have similar therapeutic effects as pharmacologic stimuli, but operating via different signaling pathways, suggesting that these two therapeutic avenues could be used in parallel to promote additive beneficial effects.

To further understand the relationship between blood flow and atherosclerosis, Chapter 4 focuses on developing a microfluidics system that can be used to evaluate the response of isolated vascular endothelial cells to physiologic flow regimens. We focused

on the endothelium because this is the cell type that sits at the interface between the artery wall and lumen and plays a key role in determining the susceptibility of an arterial segment to atherosclerosis. Thus, using a microfluidics system, we examined endothelial cell health in a more physiologically relevant geometry.

Despite the microfluidics system having commercially available components, optimizing this system came with many challenges. Each electrical component of the system had to be maintained on the exterior of an incubator, which made sterility more difficult. Additionally, the pressure controller had two channels that were attached to two reservoirs that required different pressures to reach the same flow rate. The flow sensor was a requirement for calculating desired shear stresses, however, the chosen flow sensor needed to be fined tuned to incorporate into the system. Finally, the mux recirculator was needed to maintain continuous flow through the system for 48 hours. On the cellular side of this system, we wanted to examine endothelial cells under different flow profiles over a range of shear stresses. Since endothelial cells are extremely sensitive to the flow environment, we were able to evaluate different endothelial functions by examining gene expression. In this preliminary study, comparing orbital, continuous, and pulsatile flow at different shear stresses, we were able to examine the atheroprotective markers that improve overall endothelial cell health. The glass microchannels used for these initial experiments did not allow for gas exchange and were problematic for examining gene expression. However, since the issue was recognized, future studies will use polymer microchannels to examine a range of WSS with different flow types to better understand the mechanical dose response.

5.2 Future Research

There are many important considerations for the development of therapies that target the multiple facets of atherosclerosis in a patient-specific manner. This type of precision medicine is necessary to treat this complicated disease. The chances of therapeutic strategies will depend on identifying at risk patients early on, and non-invasive targeted approaches, lowering the risk of the current procedures.

Delivering an ultrasound stimulus to soft tissue is an emerging technique in biomedical engineering. The ability of ultrasound to deliver this mechanical stimulus non-invasively, makes ultrasound an even more promising therapy for atherosclerosis. As mentioned, research has shown that mechanical forces play an essential role in cell growth, development, and repair by regulating cellular pathways. Despite the understanding that laminar flow protects against atherosclerosis, no study has attempted to engineer a mechanical stimulus that promotes the same beneficial effects. We have shown through different methods that flow can be therapeutic, but there is no mechanism to induce the same beneficial effects in arteries. Therefore, ultrasound may be able to be used to deliver a therapeutic mechanical stimulus to atherosclerotic arteries that activates the same beneficial signaling pathways as normal flow. It would also provide the first non-invasive and targeted therapeutic for atherosclerosis.

Ultrasound produces a series of mechanical waves that when propagated through a medium can induce a mechanical load and, in the case of biological materials, a biological effect [59, 124, 125]. Numerous studies have examined the efficacy of ultrasound for tissue regeneration, drug delivery, thrombosis treatment, and bone fractures [125, 126]. More importantly, ultrasound has been proven to induce beneficial

cell biological responses in soft tissue by producing a body force that enhances cell proliferation, matrix synthesis, sprouting, and cell differentiation [125-128]. *In vitro* studies using low-intensity ultrasound on endothelial cells have shown upregulations of VEGF and eNOS, as well as morphological changes from polygonal cobblestone to elongated shape [124]. Additionally, it has been demonstrated that ultrasound improved endothelium function similar to that of laminar blood flow, wherein ultrasound increased atheroprotective markers; nitric oxide, VE-Cadherin, CD31, and decreased smooth muscle cell proliferation and FSP-1 which affects vascular remodeling [129, 130]. *In vivo* experiments have shown efficacy in the context of the post-infarcted myocardium. In a mouse and porcine model, researchers demonstrated that ultrasound increased regional myocardial blood flow, improved mortality, and increased VEGF, eNOS, and bFGF compared to untreated controls [131, 132]. Therefore, these studies provide strong evidence that ultrasound can activate a beneficial response that promotes an atheroprotective endothelial phenotype. Demonstrating this would relate the hemodynamic and other aspects of the arterial mechanical environment to an external stimulus that could overcome the invasive and untargeted limitations of pharmacologic interventions for atherosclerosis. Because atherosclerosis is primarily caused by disturbed blood flow, which causes a dysfunctional endothelium, endothelial cells will be stimulated with ultrasound to promote beneficial cell biological effects. By characterizing the mechanical stimulus imposed by ultrasound onto the cell layer, we can create a therapeutic regimen to promote disease regression.

Furthering the understanding of ultrasound as a therapy will require many studies to narrow down the parameters for beneficial cell signaling. Currently in our laboratory,

ultrasound was applied to static cells, however, future work will include endothelial cells under flow in combination with ultrasound to mimic the physiologic environment. Additionally, a study where endothelial cells are preconditioned with disturbed flow is necessary to determine if ultrasound can reverse a dysfunctional endothelium. These studies are pertinent to creating a therapeutic for atherosclerotic patients. Once ultrasound has demonstrated to be effective in endothelial cells, *in vivo* experiments will need to be attempted. By using the same cuffed mouse model, we can apply ultrasound to the diseased carotid arteries and compare the results to our previous work.

On a broader scale, the development of a therapy targeted to endothelial cells can be extended to other mechanosensitive diseases. Endothelial dysfunction is not only important in atherosclerosis, but can also promote strokes, kidney failure, angiogenesis in cancer, hypertension, heart attacks, heart failure, and other vascular diseases [31]. Thus, this would be a multifaceted therapy and individualized based on the patient's needs.

References

1. Chatzizisis, Y.S., et al., *Prediction of the localization of high-risk coronary atherosclerotic plaques on the basis of low endothelial shear stress: an intravascular ultrasound and histopathology natural history study.* Circulation, 2008. **117**(8): p. 993-1002.
2. Chatzizisis, Y.S., et al., *Role of endothelial shear stress in the natural history of coronary atherosclerosis and vascular remodeling: molecular, cellular, and vascular behavior.* J Am Coll Cardiol, 2007. **49**(25): p. 2379-93.
3. da Luz, P.L., et al., *Endothelium in Atherosclerosis: Plaque Formation and Its Complications*, in *Endothelium and Cardiovascular Diseases*. 2018. p. 493-512.
4. Tsao, C.W., et al., *Heart Disease and Stroke Statistics-2022 Update: A Report From the American Heart Association.* Circulation, 2022. **145**(8): p. e153-e639.
5. Pahwa, R. and I. Jialal, *Atherosclerosis*, in *StatPearls*. 2022: Treasure Island (FL).
6. Barone Gibbs, B., et al., *Physical Activity as a Critical Component of First-Line Treatment for Elevated Blood Pressure or Cholesterol: Who, What, and How?: A Scientific Statement From the American Heart Association.* Hypertension, 2021. **78**(2): p. e26-e37.
7. Al-Mashhadi, R.H., et al., *Local Pressure Drives Low-Density Lipoprotein Accumulation and Coronary Atherosclerosis in Hypertensive Minipigs.* J Am Coll Cardiol, 2021. **77**(5): p. 575-589.
8. Bjorkegren, J.L.M. and A.J. Lusis, *Atherosclerosis: Recent developments.* Cell, 2022. **185**(10): p. 1630-1645.
9. Palmisano, B.T., et al., *Sex differences in lipid and lipoprotein metabolism.* Mol Metab, 2018. **15**: p. 45-55.
10. Gupta, R., et al., *Gender differences in 7 years trends in cholesterol lipoproteins and lipids in India: Insights from a hospital database.* Indian J Endocrinol Metab, 2016. **20**(2): p. 211-8.
11. Kumar, S., et al., *Loss of ADAMTS4 reduces high fat diet-induced atherosclerosis and enhances plaque stability in ApoE(-/-) mice.* Sci Rep, 2016. **6**: p. 31130.
12. Chatzizisis, Y.S., et al., *Augmented expression and activity of extracellular matrix-degrading enzymes in regions of low endothelial shear stress colocalize with coronary atheromata with thin fibrous caps in pigs.* Circulation, 2011. **123**(6): p. 621-30.
13. Li, M., et al., *Endothelial-Vascular Smooth Muscle Cells Interactions in Atherosclerosis.* Front Cardiovasc Med, 2018. **5**: p. 151.
14. Holzapfel, G.A., G. Sommer, and P. Regitnig, *Anisotropic mechanical properties of tissue components in human atherosclerotic plaques.* J Biomech Eng, 2004. **126**(5): p. 657-65.
15. Insull, W., Jr., *The pathology of atherosclerosis: plaque development and plaque responses to medical treatment.* Am J Med, 2009. **122**(1 Suppl): p. S3-S14.
16. Virmani, R., et al., *Lessons from sudden coronary death: a comprehensive morphological classification scheme for atherosclerotic lesions.* Arterioscler Thromb Vasc Biol, 2000. **20**(5): p. 1262-75.
17. Virmani, R., et al., *Atherosclerotic plaque progression and vulnerability to rupture: angiogenesis as a source of intraplaque hemorrhage.* Arterioscler Thromb Vasc Biol, 2005. **25**(10): p. 2054-61.

18. Koenig, W. and N. Khuseyinova, *Biomarkers of atherosclerotic plaque instability and rupture.* Arterioscler Thromb Vasc Biol, 2007. **27**(1): p. 15-26.
19. Dhawan, S.S., et al., *Shear stress and plaque development.* Expert Rev Cardiovasc Ther, 2010. **8**(4): p. 545-56.
20. Arzani, A. and S.C. Shadden, *Characterizations and Correlations of Wall Shear Stress in Aneurysmal Flow.* J Biomech Eng, 2016. **138**(1): p. 0145031-01450310.
21. Botts, S.R., J.E. Fish, and K.L. Howe, *Dysfunctional Vascular Endothelium as a Driver of Atherosclerosis: Emerging Insights Into Pathogenesis and Treatment.* Front Pharmacol, 2021. **12**: p. 787541.
22. Davignon, J. and P. Ganz, *Role of endothelial dysfunction in atherosclerosis.* Circulation, 2004. **109**(23 Suppl 1): p. III27-32.
23. De Wilde, D., et al., *Shear Stress Metrics and Their Relation to Atherosclerosis: An In Vivo Follow-up Study in Atherosclerotic Mice.* Ann Biomed Eng, 2016. **44**(8): p. 2327-2338.
24. Gnasso, A., et al., *In vivo association between low wall shear stress and plaque in subjects with asymmetrical carotid atherosclerosis.* Stroke, 1997. **28**(5): p. 993-8.
25. Cheng, C., et al., *Atherosclerotic lesion size and vulnerability are determined by patterns of fluid shear stress.* Circulation, 2006. **113**(23): p. 2744-53.
26. Hoogendoorn, A., et al., *Multidirectional wall shear stress promotes advanced coronary plaque development: comparing five shear stress metrics.* Cardiovasc Res, 2020. **116**(6): p. 1136-1146.
27. Samady, H., et al., *Coronary artery wall shear stress is associated with progression and transformation of atherosclerotic plaque and arterial remodeling in patients with coronary artery disease.* Circulation, 2011. **124**(7): p. 779-88.
28. Pedrigi, R.M., et al., *Inducing Persistent Flow Disturbances Accelerates Atherogenesis and Promotes Thin Cap Fibroatheroma Development in D374Y-PCSK9 Hypercholesterolemic Minipigs.* Circulation, 2015. **132**(11): p. 1003-12.
29. Davies, P.F., et al., *Enhanced Endothelial-Cell Turnover Is Caused by Turbulent Fluid Shear-Stress.* Clinical Hemorheology, 1985. **5**(5): p. 650-650.
30. Deng, Q., Y. Huo, and J. Luo, *Endothelial mechanosensors: the gatekeepers of vascular homeostasis and adaptation under mechanical stress.* Sci China Life Sci, 2014. **57**(8): p. 755-62.
31. Rajendran, P., et al., *The vascular endothelium and human diseases.* Int J Biol Sci, 2013. **9**(10): p. 1057-69.
32. Sahni, J., et al., *Characterizing nuclear morphology and expression of eNOS in vascular endothelial cells subjected to a continuous range of wall shear stress magnitudes and directionality.* J Mech Behav Biomed Mater, 2023. **137**: p. 105545.
33. Miller, H.A., et al., *Smooth muscle cells affect differential nanoparticle accumulation in disturbed blood flow-induced murine atherosclerosis.* PLoS One, 2021. **16**(12): p. e0260606.
34. Yamamoto, E., et al., *Low Endothelial Shear Stress Predicts Evolution to High-Risk Coronary Plaque Phenotype in the Future: A Serial Optical Coherence Tomography and Computational Fluid Dynamics Study.* Circ Cardiovasc Interv, 2017. **10**(8).

35. Stone, P.H., et al., *Prediction of progression of coronary artery disease and clinical outcomes using vascular profiling of endothelial shear stress and arterial plaque characteristics: the PREDICTION Study.* Circulation, 2012. **126**(2): p. 172-81.
36. Wang, C., et al., *Endothelial cell sensing of flow direction.* Arterioscler Thromb Vasc Biol, 2013. **33**(9): p. 2130-6.
37. Kok, A.M., et al., *The influence of multidirectional shear stress on plaque progression and composition changes in human coronary arteries.* EuroIntervention, 2019. **15**(8): p. 692-699.
38. Getz, G.S. and C.A. Reardon, *Animal Models of Atherosclerosis.* Animal Models for the Study of Human Disease, 2nd Edition, 2017: p. 205-217.
39. Pedrigi, R.M., et al., *Influence of shear stress magnitude and direction on atherosclerotic plaque composition.* R Soc Open Sci, 2016. **3**(10): p. 160588.
40. von der Thusen, J.H., T.J. van Berkel, and E.A. Biessen, *Induction of rapid atherogenesis by perivascular carotid collar placement in apolipoprotein E-deficient and low-density lipoprotein receptor-deficient mice.* Circulation, 2001. **103**(8): p. 1164-70.
41. Lee, Y.T., et al., *Animal models of atherosclerosis.* Biomed Rep, 2017. **6**(3): p. 259-266.
42. De Nisco, G., et al., *Comparison of Swine and Human Computational Hemodynamics Models for the Study of Coronary Atherosclerosis.* Front Bioeng Biotechnol, 2021. **9**: p. 731924.
43. Thim, T., et al., *Wall shear stress and local plaque development in stenosed carotid arteries of hypercholesterolemic minipigs.* J Cardiovasc Dis Res, 2012. **3**(2): p. 76-83.
44. Sasaki, T., et al., *A simple method of plaque rupture induction in apolipoprotein E-deficient mice.* Arterioscler Thromb Vasc Biol, 2006. **26**(6): p. 1304-9.
45. Schake, M.A., et al., *Restoration of normal blood flow in atherosclerotic arteries promotes plaque stabilization.* iScience, 2023.
46. Theodorou, K. and R.A. Boon, *Endothelial Cell Metabolism in Atherosclerosis.* Front Cell Dev Biol, 2018. **6**: p. 82.
47. Heo, K.S., K. Fujiwara, and J. Abe, *Shear stress and atherosclerosis.* Mol Cells, 2014. **37**(6): p. 435-40.
48. Libby, P., P.M. Ridker, and A. Maseri, *Inflammation and atherosclerosis.* Circulation, 2002. **105**(9): p. 1135-43.
49. Wentzel, J.J., et al., *Endothelial shear stress in the evolution of coronary atherosclerotic plaque and vascular remodelling: current understanding and remaining questions.* Cardiovasc Res, 2012. **96**(2): p. 234-43.
50. Lin, K., et al., *Molecular mechanism of endothelial growth arrest by laminar shear stress.* Proceedings of the National Academy of Sciences, 2000. **97**(17): p. 9385-9389.
51. Pamukcu, B., G.Y. Lip, and E. Shantsila, *The nuclear factor--kappa B pathway in atherosclerosis: a potential therapeutic target for atherothrombotic vascular disease.* Thromb Res, 2011. **128**(2): p. 117-23.
52. Mohamied, Y., et al., *Change of direction in the biomechanics of atherosclerosis.* Ann Biomed Eng, 2015. **43**(1): p. 16-25.

53. Mohammed, M., et al., *Studying the Response of Aortic Endothelial Cells under Pulsatile Flow Using a Compact Microfluidic System.* Anal Chem, 2019. **91**(18): p. 12077-12084.
54. Poznyak, A.V., et al., *A brief overview of currently used atherosclerosis treatment approaches targeting lipid metabolism alterations.* Am J Cardiovasc Dis, 2020. **10**(2): p. 62-71.
55. Nicholls, S.J., et al., *Lipid pharmacotherapy for treatment of atherosclerosis.* Expert Opin Pharmacother, 2014. **15**(8): p. 1119-25.
56. Antonopoulos, A.S., et al., *Statins as Anti-Inflammatory Agents in Atherogenesis: Molecular Mechanisms and Lessons from the Recent Clinical Trials.* Current Pharmaceutical Design, 2012. **18**(11): p. 1519-1530.
57. Pruthi, S. *Arteriosclerosis/atherosclerosis*. [cited 2023.
58. Flusty, B., et al., *Intracranial Atherosclerosis Treatment: Past, Present, and Future.* Stroke, 2020. **51**(3): p. e49-e53.
59. Biller, J., et al., *Guidelines for carotid endarterectomy: a statement for healthcare professionals from a Special Writing Group of the Stroke Council, American Heart Association.* Circulation, 1998. **97**(5): p. 501-9.
60. Falk, E., et al., *Update on acute coronary syndromes: the pathologists' view.* Eur Heart J, 2013. **34**(10): p. 719-28.
61. Al-Hijji, M.A., et al., *Safety and Risk of Major Complications With Diagnostic Cardiac Catheterization.* Circ Cardiovasc Interv, 2019. **12**(7): p. e007791.
62. Niccoli, G., et al., *Are the culprit lesions severely stenotic?* JACC Cardiovasc Imaging, 2013. **6**(10): p. 1108-1114.
63. Puri, R., et al., *High-risk coronary atheroma: the interplay between ischemia, plaque burden, and disease progression.* J Am Coll Cardiol, 2014. **63**(12): p. 1134-1140.
64. Lobatto, M.E., et al., *Atherosclerotic plaque targeting mechanism of long-circulating nanoparticles established by multimodal imaging.* ACS Nano, 2015. **9**(2): p. 1837-47.
65. Davies, P.F., et al., *The atherosusceptible endothelium: endothelial phenotypes in complex haemodynamic shear stress regions in vivo.* Cardiovasc Res, 2013. **99**(2): p. 315-27.
66. Frueh, J., et al., *Systems biology of the functional and dysfunctional endothelium.* Cardiovasc Res, 2013. **99**(2): p. 334-41.
67. Pfenniger, A., et al., *Shear stress-induced atherosclerotic plaque composition in ApoE(-/-) mice is modulated by connexin37.* Atherosclerosis, 2015. **243**(1): p. 1-10.
68. Segers, D., et al., *Atherosclerotic Plaque Stability Is Affected by the Chemokine CXCL10 in Both Mice and Humans.* Int J Inflam, 2011. **2011**: p. 936109.
69. Fraga-Silva, R.A., et al., *Diminazene enhances stability of atherosclerotic plaques in ApoE-deficient mice.* Vascul Pharmacol, 2015. **74**: p. 103-113.
70. Seneviratne, A.N., et al., *Low shear stress induces M1 macrophage polarization in murine thin-cap atherosclerotic plaques.* J Mol Cell Cardiol, 2015. **89**(Pt B): p. 168-72.

71. Xia, W., et al., *A functional folate receptor is induced during macrophage activation and can be used to target drugs to activated macrophages.* Blood, 2009. **113**(2): p. 438-46.
72. Bony, B.A., et al., *Ultrasmall Mixed Eu-Gd Oxide Nanoparticles for Multimodal Fluorescence and Magnetic Resonance Imaging of Passive Accumulation and Retention in TBI.* ACS Omega, 2020. **5**(26): p. 16220-16227.
73. Miller, H.A., et al., *Evaluating differential nanoparticle accumulation and retention kinetics in a mouse model of traumatic brain injury via K(trans) mapping with MRI.* Sci Rep, 2019. **9**(1): p. 16099.
74. Chamie, D., et al., *Optical Coherence Tomography and Fibrous Cap Characterization.* Curr Cardiovasc Imaging Rep, 2011. **4**(4): p. 276-283.
75. Chertok, B., et al., *Iron oxide nanoparticles as a drug delivery vehicle for MRI monitored magnetic targeting of brain tumors.* Biomaterials, 2008. **29**(4): p. 487-96.
76. Bony, B.A., Baeck, J. S., Chang, Y., Bae, J. E., Chae, K. S. Lee, G. H., *Water-soluble D-glucuronic acid coated ultrasmall mixed Ln/Mn (Ln = Gd and Dy) oxide nanoparticles and their application to magnetic resonance imaging.* Biomater Sci, 2014. **2**(9): p. 1287-1295.
77. Bonvin, D., et al., *Folic acid on iron oxide nanoparticles: platform with high potential for simultaneous targeting, MRI detection and hyperthermia treatment of lymph node metastases of prostate cancer.* Dalton Trans, 2017. **46**(37): p. 12692-12704.
78. Fengying Dai, M.D., Yingguo Liu, Guiying Liu, Qingjun Liu, Xin Zhang, *Folic acid-conjugated glucose and dextran coated iron oxide nanoparticles as MRI contrast agents for diagnosis and treatment response of rheumatoid arthritis.* Journal of Materials Chemistry B, 2014. **2**(16): p. 2240-2247.
79. Fang, J., et al., *Manipulating the surface coating of ultra-small Gd2O3 nanoparticles for improved T1-weighted MR imaging.* Biomaterials, 2014. **35**(5): p. 1636-42.
80. Marangoni, V.S., et al., *Enhancing T1 magnetic resonance imaging contrast with internalized gadolinium(III) in a multilayer nanoparticle.* Proc Natl Acad Sci U S A, 2017. **114**(27): p. 6960-6965.
81. Grumezescu, A.M., *Multifunctional systems for combined delivery, biosensing and diagnostics*. 2017, Amsterdam, Netherlands: Elsevier. xvi, 356 pages.
82. Zhang, W., et al., *Surface impact on nanoparticle-based magnetic resonance imaging contrast agents.* Theranostics, 2018. **8**(9): p. 2521-2548.
83. Zhou, Z., et al., *Structure-Relaxivity Relationships of Magnetic Nanoparticles for Magnetic Resonance Imaging.* Adv Mater, 2019. **31**(8): p. e1804567.
84. Longmire, M., P.L. Choyke, and H. Kobayashi, *Clearance properties of nano-sized particles and molecules as imaging agents: considerations and caveats.* Nanomedicine (Lond), 2008. **3**(5): p. 703-17.
85. Beldman, T.J., et al., *Nanoparticle-Aided Characterization of Arterial Endothelial Architecture during Atherosclerosis Progression and Metabolic Therapy.* ACS Nano, 2019. **13**(12): p. 13759-13774.

86. Sasayama, Y., et al., *In vivo activation of PEGylated long circulating lipid nanoparticle to achieve efficient siRNA delivery and target gene knock down in solid tumors.* J Control Release, 2019. **311-312**: p. 245-256.
87. Lobatto, M.E., et al., *Perspectives and opportunities for nanomedicine in the management of atherosclerosis.* Nat Rev Drug Discov, 2011. **10**(11): p. 835-52.
88. Otsuka, F., et al., *Natural progression of atherosclerosis from pathologic intimal thickening to late fibroatheroma in human coronary arteries: A pathology study.* Atherosclerosis, 2015. **241**(2): p. 772-82.
89. Poulsen, C.B., et al., *Plaque burden influences accurate classification of fibrous cap atheroma by in vivo optical coherence tomography in a porcine model of advanced coronary atherosclerosis.* EuroIntervention, 2018. **14**(10): p. 1129-1135.
90. Falk, E., *Why do plaques rupture?* Circulation, 1992. **86**(6 Suppl): p. III30-42.
91. van Bochove, G.S., et al., *Contrast enhancement by differently sized paramagnetic MRI contrast agents in mice with two phenotypes of atherosclerotic plaque.* Contrast Media Mol Imaging, 2011. **6**(1): p. 35-45.
92. Moreno, P.R., et al., *Plaque neovascularization is increased in ruptured atherosclerotic lesions of human aorta: implications for plaque vulnerability.* Circulation, 2004. **110**(14): p. 2032-8.
93. Kumamoto, M., Y. Nakashima, and K. Sueishi, *Intimal neovascularization in human coronary atherosclerosis: its origin and pathophysiological significance.* Hum Pathol, 1995. **26**(4): p. 450-6.
94. Rademakers, T., et al., *Plaque-associated vasa vasorum in aged apolipoprotein E-deficient mice exhibit proatherogenic functional features in vivo.* Arterioscler Thromb Vasc Biol, 2013. **33**(2): p. 249-56.
95. Phinikaridou, A., et al., *Increased Vascular Permeability Measured With an Albumin-Binding Magnetic Resonance Contrast Agent Is a Surrogate Marker of Rupture-Prone Atherosclerotic Plaque.* Circ Cardiovasc Imaging, 2016. **9**(12).
96. Dunmore, B.J., et al., *Carotid plaque instability and ischemic symptoms are linked to immaturity of microvessels within plaques.* J Vasc Surg, 2007. **45**(1): p. 155-9.
97. Luo, Y., et al., *Macrophagic CD146 promotes foam cell formation and retention during atherosclerosis.* Cell Res, 2017. **27**(3): p. 352-372.
98. Tang, J., et al., *Immune cell screening of a nanoparticle library improves atherosclerosis therapy.* Proc Natl Acad Sci U S A, 2016. **113**(44): p. E6731-E6740.
99. Traub, O. and B.C. Berk, *Laminar shear stress: mechanisms by which endothelial cells transduce an atheroprotective force.* Arterioscler Thromb Vasc Biol, 1998. **18**(5): p. 677-85.
100. Timmins, L.H., et al., *Oscillatory wall shear stress is a dominant flow characteristic affecting lesion progression patterns and plaque vulnerability in patients with coronary artery disease.* J R Soc Interface, 2017. **14**(127).
101. Antonacci, G., et al., *Quantification of plaque stiffness by Brillouin microscopy in experimental thin cap fibroatheroma.* J R Soc Interface, 2015. **12**(112).

102. Guy, E., et al., *Continued inhibition of atherosclerotic lesion development in long term Western diet fed CD36o /apoEo mice.* Atherosclerosis, 2007. **192**(1): p. 123-30.
103. Cherepanova, O.A., et al., *Novel Autoimmune IgM Antibody Attenuates Atherosclerosis in IgM Deficient Low-Fat Diet-Fed, but Not Western Diet-Fed Apoe(-/-) Mice.* Arterioscler Thromb Vasc Biol, 2020. **40**(1): p. 206-219.
104. Yoshida, Y., et al., *The effects of augmented hemodynamic forces on the progression and topography of atherosclerotic plaques.* Ann N Y Acad Sci, 1990. **598**: p. 256-73.
105. Stone, P.H., et al., *Role of Low Endothelial Shear Stress and Plaque Characteristics in the Prediction of Nonculprit Major Adverse Cardiac Events: The PROSPECT Study.* JACC Cardiovasc Imaging, 2018. **11**(3): p. 462-471.
106. Ku, D.N., et al., *Pulsatile flow and atherosclerosis in the human carotid bifurcation. Positive correlation between plaque location and low oscillating shear stress.* Arteriosclerosis, 1985. **5**(3): p. 293-302.
107. Tomita, H., et al., *Relationship between hemodynamics and atherosclerosis in aortic arches of apolipoprotein E-null mice on 129S6/SvEvTac and C57BL/6J genetic backgrounds.* Atherosclerosis, 2012. **220**(1): p. 78-85.
108. Nakashima, Y., et al., *ApoE-deficient mice develop lesions of all phases of atherosclerosis throughout the arterial tree.* Arterioscler Thromb, 1994. **14**(1): p. 133-40.
109. Silverman, M.G., et al., *Association Between Lowering LDL-C and Cardiovascular Risk Reduction Among Different Therapeutic Interventions: A Systematic Review and Meta-analysis.* JAMA, 2016. **316**(12): p. 1289-97.
110. Komukai, K., et al., *Effect of atorvastatin therapy on fibrous cap thickness in coronary atherosclerotic plaque as assessed by optical coherence tomography: the EASY-FIT study.* J Am Coll Cardiol, 2014. **64**(21): p. 2207-17.
111. Kini, A.S., et al., *Changes in plaque lipid content after short-term intensive versus standard statin therapy: the YELLOW trial (reduction in yellow plaque by aggressive lipid-lowering therapy).* J Am Coll Cardiol, 2013. **62**(1): p. 21-9.
112. Nicholls, S.J., et al., *Effect of two intensive statin regimens on progression of coronary disease.* N Engl J Med, 2011. **365**(22): p. 2078-87.
113. Rossi, J., et al., *Effect of simvastatin on Kruppel-like factor2, endothelial nitric oxide synthase and thrombomodulin expression in endothelial cells under shear stress.* Life Sci, 2010. **87**(3-4): p. 92-9.
114. Kumar, S., et al., *Atorvastatin and blood flow regulate expression of distinctive sets of genes in mouse carotid artery endothelium.* Curr Top Membr, 2021. **87**: p. 97-130.
115. Sangha, G.S., et al., *Preclinical techniques to investigate exercise training in vascular pathophysiology.* Am J Physiol Heart Circ Physiol, 2021. **320**(4): p. H1566-H1600.
116. Cardinot, T.M., et al., *Preventive and therapeutic moderate aerobic exercise programs convert atherosclerotic plaques into a more stable phenotype.* Life Sci, 2016. **153**: p. 163-70.

117. Moustardas, P., et al., *The complementary effects of atorvastatin and exercise treatment on the composition and stability of the atherosclerotic plaques in ApoE knockout mice.* PLoS One, 2014. **9**(9): p. e108240.
118. Aengevaeren, V.L., et al., *Exercise and Coronary Atherosclerosis: Observations, Explanations, Relevance, and Clinical Management.* Circulation, 2020. **141**(16): p. 1338-1350.
119. Dansky, H.M., et al., *T and B lymphocytes play a minor role in atherosclerotic plaque formation in the apolipoprotein E-deficient mouse.* Proc Natl Acad Sci U S A, 1997. **94**(9): p. 4642-6.
120. Glagov, S., et al., *Hemodynamics and atherosclerosis. Insights and perspectives gained from studies of human arteries.* Arch Pathol Lab Med, 1988. **112**(10): p. 1018-31.
121. Bonthu, S., et al., *Atherosclerosis, vascular remodeling, and impairment of endothelium-dependent relaxation in genetically altered hyperlipidemic mice.* Arterioscler Thromb Vasc Biol, 1997. **17**(11): p. 2333-40.
122. Poon, C., 2020.
123. Onaizah, O., T.L. Poepping, and M. Zamir, *A model of blood supply to the brain via the carotid arteries: Effects of obstructive vs. sclerotic changes.* Med Eng Phys, 2017. **49**: p. 121-130.
124. Uddin, S.M.Z., et al., *Low-Intensity Continuous Ultrasound Therapies-A Systematic Review of Current State-of-the-Art and Future Perspectives.* J Clin Med, 2021. **10**(12).
125. Montero, A.S., et al., *Ultrasound-Induced Blood-Spinal Cord Barrier Opening in Rabbits.* Ultrasound Med Biol, 2019. **45**(9): p. 2417-2426.
126. Dalecki, D., *Mechanical bioeffects of ultrasound.* Annu Rev Biomed Eng, 2004. **6**: p. 229-48.
127. Kyle, A., *BBB disruption with unfocused ultrasound alone-A paradigm shift*. 2012. p. 197-203.
128. Beccaria, K., et al., *Opening of the blood-brain barrier with an unfocused ultrasound device in rabbits.* J Neurosurg, 2013. **119**(4): p. 887-98.
129. Altland, O.D., et al., *Low-intensity ultrasound increases endothelial cell nitric oxide synthase activity and nitric oxide synthesis.* J Thromb Haemost, 2004. **2**(4): p. 637-43.
130. Mizrahi, N., D. Seliktar, and E. Kimmel, *Ultrasound-induced angiogenic response in endothelial cells.* Ultrasound Med Biol, 2007. **33**(11): p. 1818-29.
131. Hanawa, K., et al., *Low-intensity pulsed ultrasound induces angiogenesis and ameliorates left ventricular dysfunction in a porcine model of chronic myocardial ischemia.* PLoS One, 2014. **9**(8): p. e104863.
132. Shindo, T., et al., *Low-Intensity Pulsed Ultrasound Enhances Angiogenesis and Ameliorates Left Ventricular Dysfunction in a Mouse Model of Acute Myocardial Infarction.* Arterioscler Thromb Vasc Biol, 2016. **36**(6): p. 1220-9.
133. Phinikaridou, A., et al., *Noninvasive magnetic resonance imaging evaluation of endothelial permeability in murine atherosclerosis using an albumin-binding contrast agent.* Circulation, 2012. **126**(6): p. 707-19.

134. Yao, Y., et al., *In vivo imaging of macrophages during the early-stages of abdominal aortic aneurysm using high resolution MRI in ApoE mice.* PLoS One, 2012. **7**(3): p. e33523.

Appendix A

Mouse Model and Procedures

A.1 Cholesterol Measurements

Since the ApoE-/- mice used were on a high fat diet, they were extremely hypocholesterolemic, making cholesterol testing somewhat difficult. By using the Piccolo blood analyzer, we first tried measuring the whole blood. This, however, proved unaffected because the mice have such high cholesterol that it exceeded the bounds of the machine. Next we tried 3:4 ratio and a 1:2 ratio with fetal bovine serum which was not compatible with the machine. After further testing, we diluted the blood with PBS at the same ratios, and the most successful ratio was 1:2. By using heparin coated capillaries and Eppendorf tubes, blood was collected by an orbital bleed into one Eppendorf tube, then in a separate tube, 75 µl of PBS and 75 µl of blood was collected and mixed with a pipette. Next ~105 µl diluted blood was add to a lipid rotor and inserted into the Piccolo and a lipid panel was quantified.

A.2 Mice Tissue Extraction

On the day of culling, mice were injected with barbiturates and placed to sleep. Cholesterol was then measured for the final time point. Gravity fed fixation was utilized to fix each mouse by using a syringe reservoir attached to 35 cm of tubing. A butterfly needle was attached to the end of the tubing for injection of solutions. Mice were placed on an absorbent pad in a chemical hood. Their chests were opened with surgical scissors to access the heart. A butterfly need was inserted into the left ventricle of the heart and the right atrium was cut so 35 mL of saline and 35 mL of 4% PFA could circulate throughout the vasculature. Mice were considered well fixed when the liver and kidneys became transparent, and they had extremely stiff bodies.

Once the mice were fixed, tissue extraction was completed under a surgical dissection Leica microscope. Mice chests were opened further, by opening the ribcages and carefully cutting long the trachea all the way to the chin. Salivary glands and excess fat around the aortic arch and heart were removed. Connective tissue was loosened with tweezer to enable accessibility to the carotid arteries. For the left instrumented artery, scar tissue was removed and when needed, the sutures were cut and removed to take off the perivascular cuff from the artery and then the cuff was placed into isopropanol alcohol. To start extraction, tweezers were used to grip the aortic arch, and surgical micro scissors were used to remove the connection to the perivascular tissue on both carotid arteries. Once both arteries were targeted, the tissue was placed into an OCT filled well (Figure A.1) and snap frozen with -80°C Isopentane.

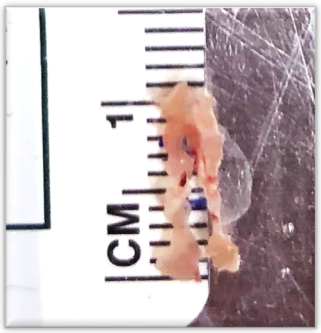

Figure A.1. Mice carotid arteries after extraction.

A.3 Atorvastatin Solution

Atorvastatin was purchased through the vet. Atorvastatin tablets (20 mg) were ground up with mortar and pestle and added to 20 mL of OraPlus suspension solution. This solution was stored at 4°C and warmed to room temperature before being used in oral gavage procedures.

A.4 Medical Imaging

A.4.1 MRI Procedure

A.4.1.1 MRI image acquisition

For image acquisition, mice were anesthetized and placed in an upright cylindrical small animal holder to maintain head and body position. Their breathing and heart rates were monitored with a pressure-based sensor. The imaging acquisition parameters were set to the following:

GEMS with 0.5mm slices 14

Matrix 256x256

Gradient echo sequence

Parameters

- TR: 78ms-100ms
- TE: 4.35ms
- Field of View: 21mm x 21mm
- Matrix: 256 x 256
- Averages/ NEX: 8
- Slices: 9-11

Images were then exported as DICOM files.

A.4.1.2 Image Revising

Time-of-flight MR angiography was done with a three-dimensional gradient-echo sequence. Sequence parameters were TR = 15 ms, TE = 2.5ms, flip angle = 20◦, FOV =

2.56 × 2.56 × 2.56 cm3, acquisition matrix=256 × 256 × 256, NA=2, total scan time=18 min. [91]
Alternate: 3-dimensional gradient recalled echo scout scan, contrast-enhanced angiography images were acquired for visualization of the aortic arch and the brachiocephalic and carotid arteries, with a field of view (FOV)=30x30x8 mm, matrix=200x200, in-plane resolution=0.15x0.15 mm (reconstructed=0.10x0.10 mm), slice thickness = 0.5 mm, repetition time/echo time= 15/6.1 ms, and flip angle=40° [133].

T1- and T2-weighted imaging in sagittal and transversal orientations was performed using a black-blood multi-slice spin-echo sequence. Black blood was achieved by placing two saturation slabs below and above the neck region saturating inflowing blood. Sequence parameters for **T1-weighted imaging** were TR=800 ms, TE=7.5ms, FOV=2.56×2.56 cm2, acquisition matrix=256×256, reconstruction matrix=512×512, slice thickness=0.5mm, NA=2, total scan time=8min. (Bochove, 2010)

Sequence parameters for **T2-weighted imaging** were TR= 2000 ms, TE=20 ms, FOV=2.56 × 2.56 cm2, acquisition matrix=256 × 256, reconstruction matrix=512 × 512, slice thickness=0.5mm, NA=2, total scan time=20 min. [91].
Alternate:
STEMS sequence. Imaging parameters were as follows: TR 1237.1 milliseconds, TE 12.8/34.2 milliseconds, FOV 2.5 cm, FA was 180°, matrix size 256 × 256, and in- plane resolution 98 μm × 98 μm; slice thickness of 0.5 mm, and four excitations [134].

Cine gradient echo sequence. Imaging parameters included the following: repetition time=RR interval/number of frames (typically ~10 ms), echo time1 ms, FOV=25x25 mm, matrix size=192x192, in-plane resolution=0.13x0.13 mm, slice thickness=1 mm, flip angle=40°, averages=3, slices=1, 1 k-space line per frame, 8 to 12 frames per cardiac cycle depending on the length of the RR interval, and scan time=8 minutes [133].

Image Contrast assessment T1 Mapping:
A 2-dimensional Look-Locker sequence planned perpendicular to the ascending aorta was used to determine the optimal inversion time for blood signal nulling. Acquisition parameters were as follows: FOV=30x30 mm, matrix=80x80, in-plane resolution=0.38x0.38 mm, slice thickness=2 mm, repetition time/echo time= 19/8.6 ms, repetition time between subsequent inversion recovery pulses=1000 ms, and flip angle_10° [133]
An inversion recovery 3-dimensional fast gradient echo sequence was acquired 30 minutes after injection and was used for DE MRI and visualization of contrast uptake. Imaging parameters were as follows:

FOV=30x30x8 mm, matrix=304x304, in-plane resolution=0.1x0.1 mm, measured slice thickness=0.5 mm, slices=32, repetition time/ echo time=28/8 ms, repetition time between subsequent inversion recovery pulses=1000 ms, and flip angle_30°.
T1 mapping was performed with the use of a sequence that employs 2 nonselective inversion pulses with inversion times ranging from 20 to 2000 ms, followed by 8 segmented readouts for 8 individual images.
The 2 imaging trains resulted in a set of 16 images per slice with increasing inversion times. For T1 mapping, the acquisition parameters were as follows: FOV=36x22x8 mm, matrix=192x102, in-plane resolution_0.18_0.22 mm, measured slice thickness=0.5 mm, slices=16, repetition time/echo time=9.6/4.9 ms, flip angle=10°. T1 values were computed on a pixel-by-pixel basis with the use of in-house Matlab software.

A.4.2.2 Ultrasound

The Vevo3100 (Fujifilm VisualSonics, Toronto, Canada) ultrasound system and MX550D transducer (40 MHz center frequency) were used for imaging. Mice were anesthetized using 1-2% isoflurane with balance 100% O2 and placed on a heated stage (37 oC) in the supine position. Hair in the neck region was removed (Nair) and ultrasound gel was applied liberally to the region. The transducer was placed in the sagittal plane along the carotid artery. M-mode imaging was done ~3-4 mm proximal to the carotid bifurcation on the left and right carotid arteries to measure vessel diameter. At the same location diameter was measured, Pulsed Wave Doppler measured maximum blood velocity. Analysis was done using Vevo Lab (version 5.6.1) offline and included maximum velocity, total blood volume estimated by velocity time integral analysis, and vessel diameter

A.5 Software Protocols

A.5.1 MRI analysis in ITK-Snap

MRI slices were imaged in such a way that 14 slices were taken from the carotid bifurcation to the aortic arch and saved in a .gem folder. This fold is then selected and imported into ITK-Snap for segmentation of the carotid arteries. This is done by magnifying the image 4x and then by selecting the polygon mode tool (Figure A.2). Each carotid artery is traced in the 3 slices that contain the cuff region on both the right and left vessels. The week 0 time point is segmented after the week 1 time point to ensure that the regions selected pertain the cuff throughout the study. The week 0 time point is then averaged over these 3 slices later in the quantification process and used to normalize the level of stenosis.

Figure A.2. Select segment tool in ITK-Snap software

A.5.2 ImageJ analysis of carotid artery area

Once the cuffed region is segmented in ITK-Snap, these segmentations are imported into ImageJ. Set measurements:
File menu Analyze->Set Measurements
Select Area, Perimeter, Bounding rectangle, Feret's diameter, Display Label
*Note: the Feret's diameter provides the major and minor axis of an ellipse fit
Then the carotid artery being quantified is selected with the Wand tool. Next the analyzing of area can take place with the overlay tool. Under Image < Overlay < Add Selection, this will add the first cross section. Then under Image < Overlay < to ROI Manager, all other sections can be quantified by adding or deleting slices for area and diameter calculations (Figure A.3). To measure the selection, in ROI manager, select Add [t], and then measure. For next artery cross section, select previous addition in ROI Manager and click delete, then select new cross section in image window with the wand tool and click Add [t], measure, and repeat this process for all sections. This can then be saved as a .csv file or copied into excel for further quantification and normalization.

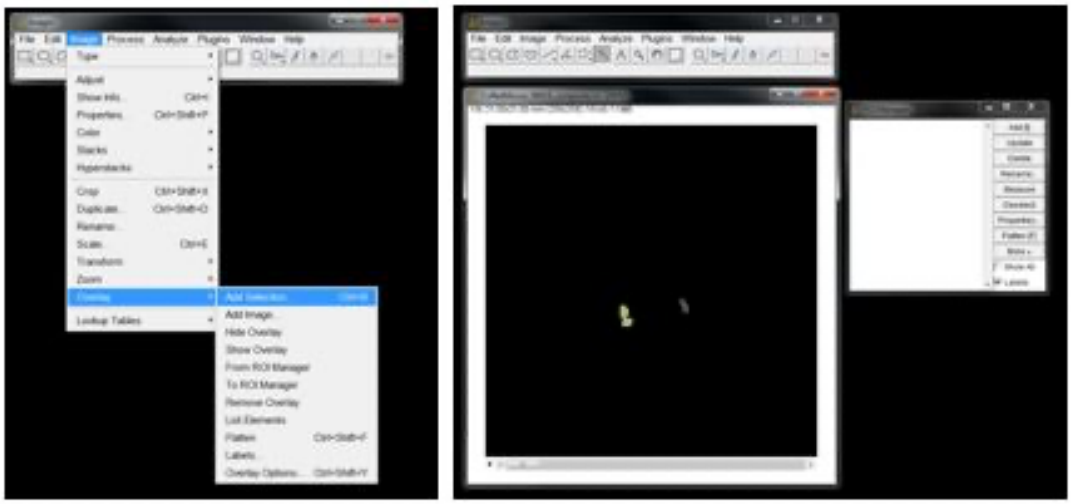

Figure A.3. ImageJ stenosis area measurement protocol.

A.5.3 Ultrasound Velocity Analysis

The Vevo3100 (Fujifilm VisualSonics, Toronto, Canada) ultrasound system and MX550D transducer (40 MHz center frequency) were used for imaging. Mice were anesthetized

using 1-2% isoflurane with balance 100% O2 and placed on a heated stage (37°C) in the supine position. Hair in the neck region was removed (Nair) and ultrasound gel was applied liberally to the region. The transducer was placed in the sagittal plane along the carotid artery. M-mode imaging was done ~3-4 mm proximal to the carotid bifurcation on the left and right carotid arteries to measure vessel diameter. At the same location diameter was measured, Pulsed Wave Doppler measured maximum blood velocity.
Once imaging was completed, files were imported into Vevo Lab for analysis. Ultrasound peak velocity of vascular flow can be measured in M-Mode. To add a velocity measurement, click measurements → velocity and then place the yellow tagger at the base of the desired velocity curve and then drag cursor to other side of peak at the next base. Three cardiac cycles were measured, and saved in the report. The cardiac cycle's velocity measurements were averaged for both the left and the right carotid arteries.

A.5.4 VMTK Lab Centerline

For the CFD, VMTKLab was used to first create a rough 3D outline of the carotid arteries. Once VMTKLab is open, the segmentation option was selected. Next the MRI .gem folder was imported and the left instrumented artery was focused on. Once loaded, the initialization type was selected as active tubes. Seeds were placed on the cross section of the carotid artery and adjusted to the appropriate area using the fine tuning mechanism. After the seeds were put in place, the active tubes were run with less than 100 iterations to create a rough 3D model of the carotid artery. The model was save as an .stl file so it could then be loaded back into VMTKLab. On the home page, the centerlines option was selected and the .stl file was imported. Next seeds were placed at the center of the inlet and outlet of the modeled carotid artery to create a centerline from downstream to upstream. This centerline could then be used in the CFD process, along with the diameter from ImageJ and the velocity from the Doppler ultrasound to create a realistic model of the left artery at the different time points.

Appendix B

Histology Protocols

B.1 Oil Red O

1. Air dry slides (make sure slides are labeled with pencil or in a specific order. Ink will bleed)
2. Filter ORO (company)
3. Pre-warm ORO to 60 °C in a water bath
4. Insert slides into slide holder and place in PBS for 3 min.
5. Fix sections in 10% formalin for 10 min.
6. Wash in 3 changes of tap water
7. Wash with distilled water for 5 min.
8. Place in Propylene glycol for 2 min.
9. Transfer slide to 60°C ORO and incubate for 20 min.
10. Wash in at least 3 changes of tap water for 15 min.
11. Counterstain with Hematoxylin for 1.5 min.
12. Wash in 3 changes of tap water for 10 min.
13. Dip slides 10x in 0.5% Ammonium Hydroxide
14. Wash in tap water for 10 min.
15. Mount with Polymount while slides are still wet

B.2 Picro Sirius Red

Picric Acid Solution

1. Add 2.4g of picric acid (solid) to 200 ml of distilled water and shake for 5-10 min. Will need to decant the water from the container and scoop the acid solid. Be sure to replace the water to the picric acid.
2. Add 0.2g of direct red 80 (Sigma) to make 0.1% solution
3. Add 0.2g of fast green FCF (Sigma) to make 0.1% solution
4. Shake final solution for 5-10 min.

Staining Protocol

1. Air dry slides
2. Place slides in 4% Paraformaldehyde overnight for unfixed tissue or 4-6 hours for fixed tissue
3. Wash in PBS for 10 min.
4. Incubate in Picro Sirius Red solution for 1 hour at room temperature
5. Wash in 0.01% HCl for 2 min. (27 uL HCl: 100mL dH2O)
6. Dehydrate for 3 seconds in ethanol with dH2O in the following concentrations
    a. 50% ethanol

   b. 70% ethanol
   c. 90% ethanol
   d. 100% ethanol
   e. 100% ethanol
7. Let Ethanol evaporate
8. Mount with Tissue Tek

B.3 CD68 Immunostain

Stain was optimized by running every combination of primary and secondary antibodies at 1:250, 500, 750, 1000. The best combination was 1:250 for both primary and secondary antibodies.

1. Air dry slides. Make sure slides are labeled or in a specific order since ink will run in acetone.
2. Fix slides in -20°C Acetone for 10 min.
3. Wash in PBS for 3x5 min.
4. Block with 0.3% Hydrogen Peroxide for 20 min.
5. Dunk in acetone and air dry slides
6. Apply PAP pen hydrophobic boundary around tissue sections
7. Incubate with non-specific binding (either goat serum or fetal bovine serum depending on antibody host animal)
8. Incubate in primary antibody for 1 hour at room temperature
9. Wash in PBS for 3x5 min.
10. Incubate in secondary antibody for 1 hour at room temperature
11. Wash in PBS for 3x5 min.
12. Incubate with 0.0025 ug/mL of Dapi for 1.5 min
13. Wash in PBS for 2x5 min.
14. Mount with Fluorgold Mounting Media while slides are still damp

B.4 Smooth Muscle Alpha Actin Immunostain

Stain was optimized by running every combination of primary and secondary antibodies at 1:250, 500, 750, 1000. The best combination was 1:250 for primary and 1:1000 for secondary antibodies. Since this marker was not a surface receptor, target retrieval methods were also optimized to access the receptor. Both a triton solution and a target retrieval buffer were utilized.

1. Air dry slides. Make sure slides are labeled or in a specific order since ink will run in acetone.
2. Fix slides in -20°C Acetone for 10 min
3. Block with 0.3% Hydrogen Peroxide for 20 min.
4. Place in 0.025% Triton for 10 min.
5. Wash in PBS for 3x5 min.
6. Place in 80°C Sodium Citrate Buffer (pH = 9) for 30 min.

    a. Make by mixing 2.6g of sodium citrate in 1L of dH2O (10M sodium citrate). Add 10M sodium hydroxide incrementally until pH is 9
7. Wash in PBS for 3x5 min.
8. Dunk in acetone and air dry slides
9. Apply PAP pen hydrophobic boundary around tissue sections
10. Incubate with non-specific binding (either goat serum or fetal bovine serum depending on antibody host animal)
11. Incubate in primary antibody for 1 hour at room temperature
12. Wash in PBS for 3x5 min.
13. Incubate in secondary antibody for 1 hour at room temperature
14. Wash in PBS for 3x5 min.
15. Incubate with 0.0025 ug/mL of Dapi for 1.5 min.
16. Wash in PBS for 2x5 min.
17. Mount with Fluorgold Mounting Media while slides are still damp

B.5 Calponin Immunostain

Stain was optimized by running every combination of primary and secondary antibodies at 1:250, 500, 750, 1000. The best combination was 1:100 for primary and 1:250 for secondary antibodies. Since this marker was not a surface receptor, target retrieval methods were also optimized to access the receptor. Both a triton solution and a target retrieval buffer were utilized.

1. Air dry slides. Make sure slides are labeled or in a specific order since ink will run in acetone.
2. Fix slides in -20°C Acetone for 10 min
3. Block with 0.3% Hydrogen Peroxide for 20 min.
4. Place in 0.025% Triton for 10 min.
5. Wash in PBS for 3x5 min.
6. Place in 80°C Sodium Citrate Buffer (pH = 9) for 30 min.
    a. Make by mixing 2.6g of sodium citrate in 1L of dH2O (10M sodium citrate). Add 10M sodium hydroxide incrementally until pH is 9
7. Wash in PBS for 3x5 min.
8. Dunk in acetone and air dry slides
9. Apply PAP pen hydrophobic boundary around tissue sections
10. Incubate with non-specific binding (either goat serum or fetal bovine serum depending on antibody host animal)
11. Incubate in primary antibody for 1 hour at room temperature
12. Wash in PBS for 3x5 min.
13. Incubate in secondary antibody for 1 hour at room temperature
14. Wash in PBS for 3x5 min.
15. Incubate with 0.0025 ug/mL of Dapi for 1.5 min.
16. Wash in PBS for 2x5 min.

17. Mount with Fluorgold Mounting Media while slides are still damp

B.6 Ki67 Immunostain

Ki67 was recommended by a reviewer for examining synthetic smooth muscles cells and how smooth muscle cells are undergoing mitosis. Stain was optimized by running every combination of primary and secondary antibodies at 1:250, 500, 750, 1000. The best combination was 1:100 for primary and 1:250 for secondary antibodies. Since this marker was not a surface receptor, target retrieval methods were also optimized to access the receptor. Both a triton solution and a target retrieval buffer were utilized.

18. Air dry slides. Make sure slides are labeled or in a specific order since ink will run in acetone.
19. Fix slides in -20°C Acetone for 10 min
20. Block with 0.3% Hydrogen Peroxide for 20 min.
21. Place in 0.025% Triton for 10 min.
22. Wash in PBS for 3x5 min.
23. Place in 80°C Sodium Citrate Buffer (pH = 9) for 30 min.
    a. Make by mixing 2.6g of sodium citrate in 1L of dH2O (10M sodium citrate). Add 10M sodium hydroxide incrementally until pH is 9
24. Wash in PBS for 3x5 min.
25. Dunk in acetone and air dry slides
26. Apply PAP pen hydrophobic boundary around tissue sections
27. Incubate with non-specific binding (either goat serum or fetal bovine serum depending on antibody host animal)
28. Incubate in primary antibody for 1 hour at room temperature
29. Wash in PBS for 3x5 min.
30. Incubate in secondary antibody for 1 hour at room temperature
31. Wash in PBS for 3x5 min.
32. Incubate with 0.0025 ug/mL of Dapi for 1.5 min.
33. Wash in PBS for 2x5 min.
34. Mount with Fluorgold Mounting Media while slides are still damp

Appendix C

Microfluidics Protocols

C.1 Turning system on

1. Turn OBI and MUX recirculation on
2. Plug in BFS flow sensor
3. Open Software ESI
4. Turn pump on by turning knob to auto, then flipping switch to open (labeled 1)
5. Hit play button for OBI in software
6. Click on Mux recirculation setting and make sure it is set at the home position
7. Adjusted pressure to desired flow rate

C.2 Turning system off

1. Set pressure to 0
2. Turn off OBI and MUX, unplug flow sensor
3. Exit out of software
4. Turn pump off by flipping switch to 0 and then turning knob to off

C.3 Experimental Set-up

1. Turn on system (see above) for at least 30 min prior to experiment to warm up
2. Make sure dummy chips are in place
3. Run ethanol through system
4. Place PBS in autoclaved reservoirs and run it through system for ~5 min at 500-1000 mbar
5. Place media in reservoirs. There should be >100 ml of media between the two reservoirs at approximately equal volume. Typically add >50 ml in Reservoir 1 and Reservoir 2.
6. Flow sensor will need to be calibrate before experiments.
    a. In the hood, use a syringe and needle to take ~10 ml of media
    b. Unhook the flow sensor from the chip – there's a white luerlock that can be unscrewed and the blue pieces can be pushed up the tubing
    c. Inject media into tubing at the inlet, make sure you see the flow rate increasing in the software
    d. Once flow is still, click on zero calibrate under flow sensor settings
    e. Refit the tubing to the luerlock and screw on tightly
7. Mark the inlet and outlet of sample chip so it does not get mixed up for lysing
8. Add in sample chip – **attached outlet first, then inlet**
9. Start experiment by selecting configuration sequence and hitting play button

10. Run for allotted time. Make sure to check reservoirs every 8-12 hours to make sure there are no leaks or that the media isn't running out
11. Once experiment is complete, set pressure to 0 mbar
12. Remove sample, **remove inlet first and then outlet**
    a. Immediately lyse samples and store in -80°C (*see C.6).
13. Add in dummy chips back into system
14. Change reservoir 1 to ethanol and run ethanol through system
15. Reservoir 2 is now waste
16. Remove Reservoir 2 and replace with Ethanol filled reservoir.
17. Rerun ethanol through configuration A and B.
18. Turn system off (see above).

C.4 Create a Sequence in Scheduler

1. Once system is on an ready to run, place PBS in reservoirs for calibration
2. Make sure flow sensor is zero calibrated because it will effect pressure levels selected
3. For each pressure channel, determine the desired shear stress and corresponding flow rate. Then by adjusting the pressure, determine the best pressure for flow rate in channel 1 and channel 2. *note: pressure will be different in each channel based on the flow rate. Channel 1 is typically a higher pressure than channel 2.
4. Once the pressures are known, make sure MUX recirculation is in the correct position for channel 1, and set pressure to desired flow rate.
5. Click config, save configuration
    a. Naming convention will have FlowType_SS or FR or Pressure_configuration (A or B)
6. Once channel 1 is saved, reposition MUX for configuration B and set channel 2 to desired pressure. Again, save configuration.
7. In scheduler, order will always be as follows
    a. OBI – 1: select configuration A from saved folder
    b. DIST - valve 1
    c. Time (depends on shear stress – will need to time it for each shear stress)
    d. OBI – 2: selected configuration B from saved folder
    e. DIST - valve 2
    f. Time
8. For repetitions, calculate the amount of repetitions you'll need for the experiment time
9. For example, for 24 hour experiment for 2 Pa at 1.5 min, set the repetitions for 500 to be safe
10. For 48 hours at 2 Pa, at 1.5 min set repetitions for 1000 repetitions.

11. Can stop the experiment at any time by clicking stop button and setting pressure to 0 mbar
12. Save scheduler by naming it FlowType_SS or FR_exp#_date

C.5 Cell Culture

C.5.1 HY926 Immortalized Cells

To determine if microfluidics channels could be used in series, we tested one chip vs. two chips in series with an immortalized cell line. Cells were seeded into channels using the same protocol as HUVECs below, however due to the type of cell the number of usable passages was significantly increased.

C.5.2 HUVECS

HUVECs were allowed to come up to 98-100% confluency in a T-75 flask. Cells were washed with PBS and then trypsinized with 4 ml. 8 ml of media was added to stop the trypsin reaction and media plus trypsin solution was added to a 15 ml falcon tube and spun down in a centrifuge. The cell pellet was cleared of liquid and 1 ml of fresh media was added to break up the pellet.

Once the cells were counted, 60,000 cells/cm^2 were seeded into the micro channels and well plates. Cells were allowed to adhere and after ~24 hours, media was changed and microfluidics experiments were started and ran for 48 hours.

For high shear stress, a preconditioning step was added for 6 hours to allow cells to acclimate to the flow environment. Moderate shear stress (1.36 Pa) was applied and then after 6 hours, the shear stress was increased to 1.88 Pa and ran for the remaining 42 hours. The protocol is as follows:

1. Wash a confluent T-75 of HUVECs with PBS
2. Trypsinize with 4mL for 3-5min
3. Add 8mL of media
4. Transfer cell mixture to 15mL falcon tube
5. Centrifuge cells for 5min at 900rpm
6. Aspirate fluid
7. Resuspend cell pellet in 1mL of fresh media, thoroughly breaking up the pellet
8. Take 5uL of the cell solution and add 35uL of fresh media
9. Use 10uL of mixture to count cells (using appropriate kit)
10. Calculate correct fluid volume to seed at 60,000 cells/cm2 in the pre-collagen coated ibidi channels
    a. Mix the appropriate amount of the cell mixture with enough media to total 600uL for three chips
    b. Use a 1mL syringe with needle tip to pull up the 600uL
    c. Gently pump syringe to remove bubbles
    d. Remove needle tip
    e. Push fluid to tip of syringe

    f. Seal syringe on channel, push 200uL through channel
    g. Repeat step 16 with second channel
    h. Aspirate any bubbles and fill reservoirs of both chips with remaining volume from original 600uL
11. Calculate correct fluid volume to seed pre-collagen coated 12-well controls at 60,000 cells/cm2
    a. Use 1mL micropipette to dispense correct amount into each media-filled control well
    b. Agitate plate to ensure dispersal of cells
12. Allow cells to adhere for ~24 hours
13. Change media in channels and controls
14. Hook up channels to microfluidics system
15. Run experiment for 48 hours

C.6 RNA lysing protocol

Once experiment was completed, micro channels were removed from system. A 1 ml syringe was filled with PBS and inserted into the inlet of the channel. PBS is used to wash cells and remove excess media. After a min, RNeasy RLT buffer was injected into the inlet of channel and placed on a rocker for 1.5 min. The micro channels were then placed under a microscope to make sure cells had detached. The syringe was then added to the outlet of the channel and pulled up the RNA solution and placed into a 1.5 ml Eppendorf tube. The Eppendorf tubes were then placed on a vortex for 1 min. All sample were stored at -80°C.

C.7 RNA and Protein Isolation

1. Remove samples from -80°C and place in water bath until thawed.
2. Add 1 volume of 70% ethanol to Eppendorf tubes of samples.
3. Transfer sample + ethanol solution into RNeasy spin column.
4. Centrifuge
5. Flow through can be collected as protein. If not using, discard solution.
6. Add 700 µl Buffer RW1 to each RNeasy spin column. Centrifuge. Discard flow through
7. Add 350 µl Buffer RW1 to RNeasy column. Centrifuge. Discard flow through
8. Make DNase incubation mix with 10 µl DNase 1 stock solution and 70 µl of Buffer RDD
9. Add 80 µl of DNase incubation mix directly to RNeasy column membrane. Incubate for 15 min at room temperature.
10. Add 350 µl Buffer RW1 to RNeasy column. Centrifuge. Discard flow through.
11. Add 700 µl of RW1 to RNeasy spin column. Centrifuge. Discard flow through.
12. Add 500 µl of Buffer RPE to RNeasy spin column. Centrifuge. Discard flow through.

13. Add 500 µl of Buffer RPE to RNeasy spin column. Centrifuge. Discard flow through.
14. Centrifuge for 1 min to dry.
15. Place RNeasy column into new 2 ml collection tube. Centrifuge for 1 min to dry.
16. Place RNeasy column into a new 1.5 ml collection tube.
17. Add 30 µl of RNase-free water directly to column membrane. Centrifuge for 1 min.
18. Immediately use plate reader to determine 260/280 values and RNA concentration for each sample.
19. Store samples in -80°C.

C.8 cDNA Extraction

To make cDNA solution. Sample concentration quantification is required.

1. Determine amount of RNA needed to make a 200ng solution.
   ie. RNA (ng/ µl)*X = 200 ng
   25 ng/ µl*X =200 ng
   X = 8 µl of RNA
2. Make cDNA solution. Must add up to 16 µl
   Since 8 µl of RNA is required and 4 µl RT solution is constant, 4 µl is left over so hH_2O is required to make a 200ng solution.
3. Calculation amount of RNA and water for each sample needed
4. Make 2 tubes of solution for each sample
5. Place in Thermocycler for 30 min.
6. Store in -20°C.

Now make diluted solution for 200 reactions

1. Fill 1.5 ml Eppendorf tubes with 984 ml of hH_2O
2. Ad 16 µl of cDNA to Eppendorf tube.
3. Split solution into 6x200 µl strip tubes (~165 µl per tube).

C.9 RT-qPCR

1. Retrieve sterile 96 well plate.
2. Using 12 pipette tip, pipette 10 µl of Syber Green solution into each well.
3. Pipette 5 µl of diluted RT samples into each well.
4. Pipette 5 µl of gene primers into each well.
5. Cover plate with stick on cover, seal all side and around each well.
6. Vortex plate.
7. Centrifuge at 1000g for 1 min.
8. Place plate in plate reader.
9. Quantify data in Design and Analysis application.

Appendix D

Additional Experiments

D.1 Contractile and Synthetic Smooth Muscle Cells

During our nanoparticle paper submission, a reviewer comment made us look more into contractile and synthetic smooth muscle markers. While SMα-actin, Calponin and Ki67 were in the paper, SM22 was also attempted for a contractile marker. For this paper, we needed to add a specific contractile comparator. SM22 and Calponin were the two markers tested, however since Calponin had better fluorescence, that was the marker chosen (Figure D.1). SM22 is a calponin-related protein, so both markers would have demonstrated similar results.

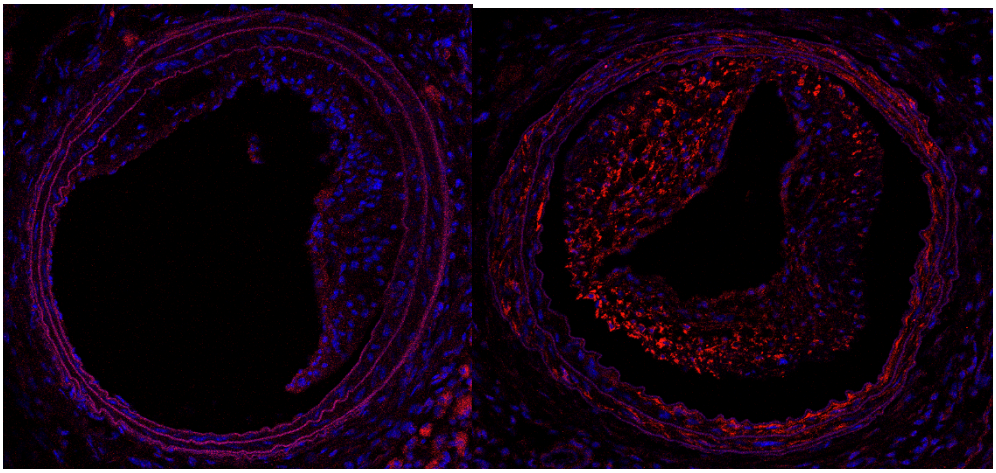

Figure D.1. Displays the intensity difference in (A) SM22 and (B) Calponin stains

D.2 eNOS

ENOS was the first fluorescent stain ever attempted in tissue by our group. We lacked expertise for this stain at the time, whereas if we attempted it again with our current knowledge and methods, we would most likely succeed in staining this marker in tissue. The biggest reasons it did not demonstrate quality results was most likely due to the intracellular marker not being brought to the surface with antigen retrieval methods. Furthermore, due to lack of understanding, we were using a 488 excitation secondary antibody which is not an appropriate wavelength for mouse tissue due to auto-fluorescence. Were we to attempt this stain in the future, we would be able to improve the quality of this stain significantly.

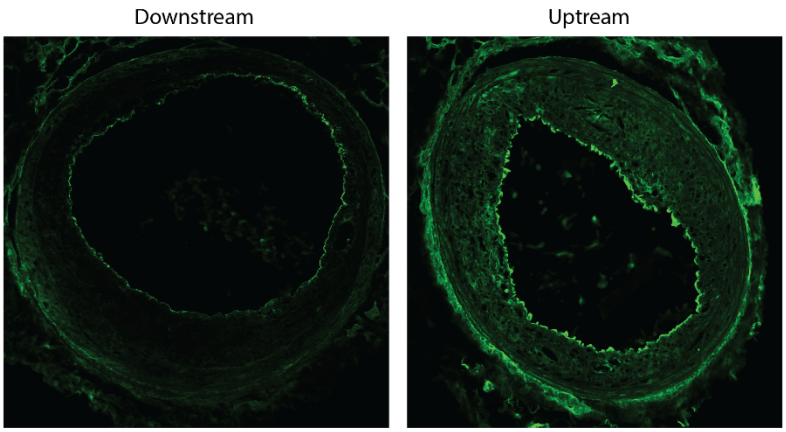

Figure D.2. eNOS expression in upstream and downstream tissue sections.

D.3 Macrophage markers

To authenticate the macrophage markers, rat macrophages were isolated over the macrophage spectrum. M1 and M2 macrophages as well as naive macrophages were isolated and stained with each antibody (Figure D.3). For pan macrophages markers, in addition to CD68 (Appendix B.3), F480 and MAC3 were also optimized. CD68 stained the macrophages over the spectrum equally, while F480 and MAC3 had less fluorescence between groups. F480 was the least optimal stain in both cells and tissue, while MAC3 was better quality, it lagged in the M2 macrophages. For M1 macrophages, iNOS was attempted. While iNOS was a quality marker in cells, it was more difficult to stain for in tissue due to antigen retrieval. Additionally, it did not add to the data for the paper. For M2 macrophages, KLF4 and CD163 were attempted, and it showed that they were not quality markers for M2 macrophages because they stained multiple types of macrophages across the spectrum. Since the M2 markers were not specific, we did not attempt the stains in tissue

Cell stain protocol was as followed:

1. Cells were fixed in 4% PFA and stored at 4°C prior to staining
2. Rinse with PBS 3x5 min
3. Block with 1% BSA, 22.52 mg/ml glycine in PBST for 30 min at room temperature
4. Incubate with primary antibody diluted in blocking buffer (1:100μl) for 1 hour at room temperature
5. Wash cells 3x5 min in PBS
6. Incubate with secondary antibody diluted in blocking buffer (1:250μl) in the dark for 1 hour at room temperature
7. Wash 3x5 min in PBS
8. Incubate with Dapi at 1 μg/ml for 2 min
9. Wash cells in PBS
10. Mount with mounting media or store in PBS

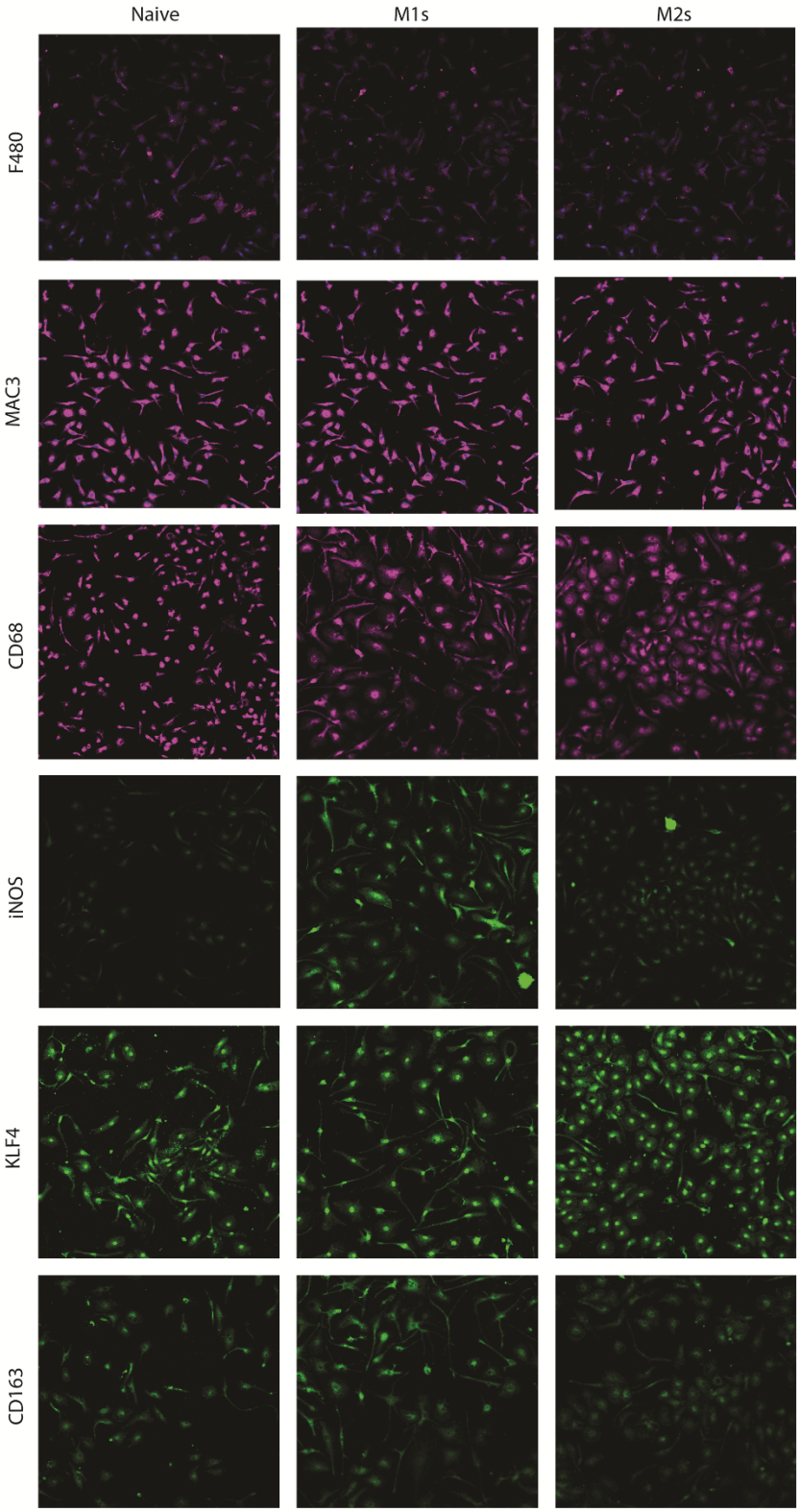

Figure D.3. Immunofluorescent stains M1, M2, and naive macrophages. Helped determine the best markers for staining different types of macrophages.

D.4 RNA Scope

RNA Scope in situ Hybridization was attempted to examine additional markers for our laminar flow study. It is the process that allows visualization of single RNA molecules in a variety of sample types with the detection of up to four target genes. For our study, we examined 4 probes: ICAM-1, IL-6, Collagen I, and Collagen III (Figure D.4).

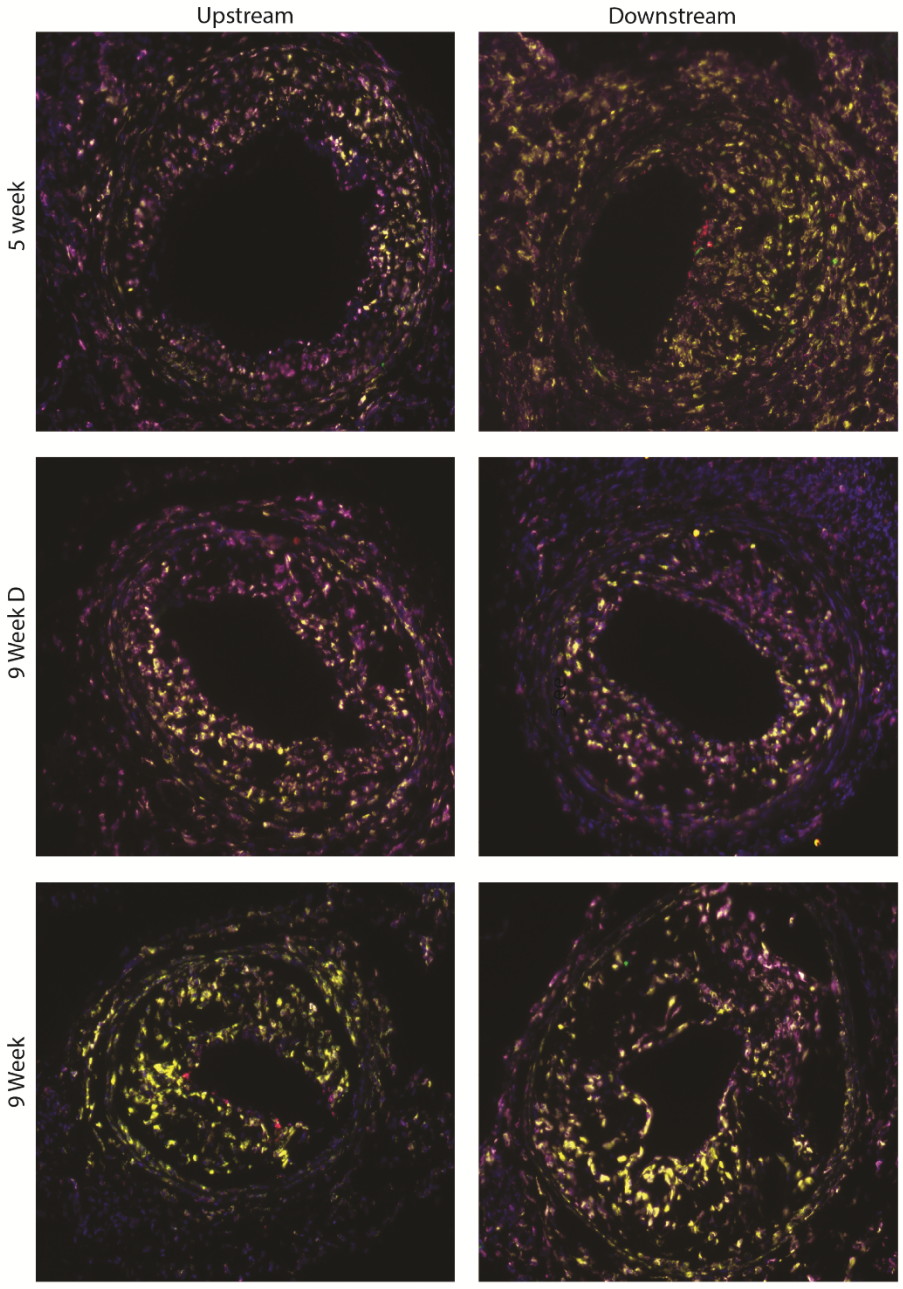

Figure D.4A. RNA Scope fluorescent images of different mice tissue sections for collagen i and iii, ICAM-1, and IL-6.

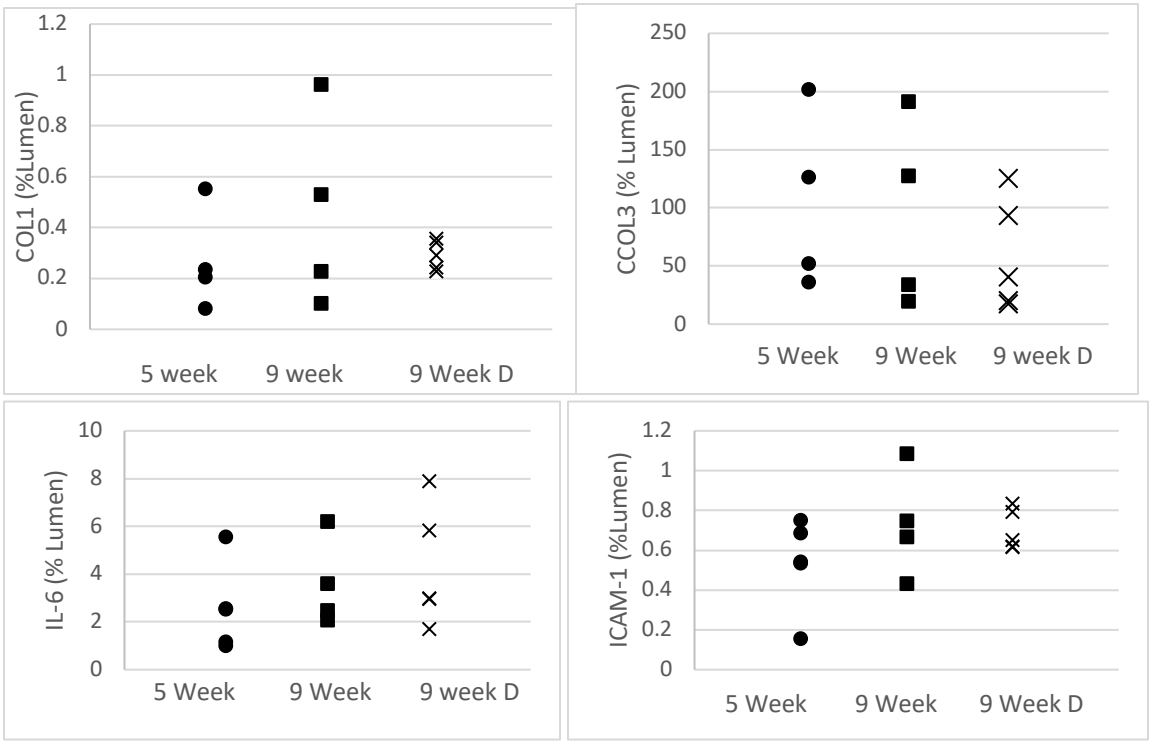

Figure D.4B. Upstream RNA scope data of each probe target.

D.5 En face

In an attempt to examine the endothelial cell layers lining the mouse carotid arteries, we utilized and *en face* immunofluorescence stain. The protocol was as follows:

1. Using a small animal dissection or surgical microscope, carotid arteries were placed in a well with PBS and cut axially (Figure D.5).
2. Tissue was placed into clean well with PBS
3. Aspirate the PBS and add 0.1% Triton in PBS
4. Rock at room temperature for 10 min
5. Wash with PBS
6. Block in non-specific binding 10% goat serum in 10% TTBS (2.5% Tween20 in 10%Tris buffer saline) for 30 min on rocker at room temperature
7. Incubate with primary antibody in TTBS and 10% goat serum for 1 hour at room temperature
8. Wash with 10% TTBS with rocking 3x10 min
9. Incubate with secondary antibody + Dapi solution in 10% goat serum in 10% TTBS on rocker for 1 hour at room temperature
10. Wash with 10% TTBS rocking at room temperature

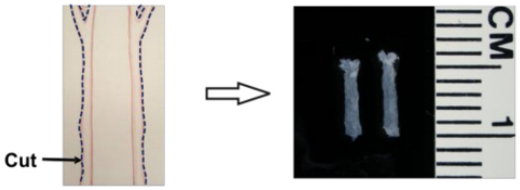

Figure D.5. Carotid artery example of *en face* orientation.

11. Wash with PBS for 5 min
12. Place one drop of antifade Fluorgold mounting media on cover slip
13. Place the tissue face down on cover slip so endothelial cell layer is facing upwards on slide
14. Place slide on top of tissue
15. Store in fridge for longer wait, or RT when imaging the next day

This protocol was semi-successful. It will need to be re-optimized for antibodies chosen. It was decided that this protocol could be a separate paper for examining the endothelial markers along with RT-qPCR for later mouse studies.